Modeling and Development of Compact Onboard Fuel Processors for PEM Fuel Cell Applications

by

Amit Dhingra

A dissertation submitted in partial fulfillment
of the requirements for the degree of
Doctor of Philosophy
(Mechanical Engineering)
in The University of Michigan
2012

Doctoral Committee:

Professor Hong G. Im, Chair
Professor Katsuo Kurabayashi
Professor Phillip E. Savage
Professor Margaret S. Wooldridge

This dissertation is dedicated to my parents,
Capt. N. L. Dhingra
and
Dr. B. Dhingra
for their everlasting love and support.

Acknowledgements

I am in deep debt and am very grateful to my advisor Professor Hong G. Im for his invaluable guidance of my doctoral study. His constructive comments and criticism has definitely left a mark on me and this work. He has been very accessible and his door has always been open no matter how trivial or immense the issue.

I am thankful to the amazing people I worked with in the Mechanical and Chemical Departments. Dr Sujit Srinivas, Dr Andrew Tadd, Dr Gap Kim and Dr Chang Kim to name a few. This thesis would have never seen the light if it had not been for you all. Many thanks.

My long hours in the office would have been quite dull had it not been for my lab mates. I would like to thank the students in the research group for their advice and support and all the fun we had. Dr Sankaran, Dr Yoo, Jingjing and Songtao. You have been an amazing company all these years.

I am also very thankful to the rest of my doctoral committee - Professor Wooldridge, Professor Kurabayashi and Professor Savage for their support and patience.

A big thanks to all my friends who have made my life in Ann Arbor a thoroughly enjoyable and fulfilling experience. You have been my family and home away from home.

This thesis would have never seen the light of day without the unconditional support and love of my parents. I dedicate this thesis to them for always standing behind me and never doubting me.

The final and most important appreciation is due to my wife Saru. She wielded the stick when it was required most to finally get the thesis written and completed. In-spite of all the frustration I cause her, she continues to sternly and solemnly stand behind me and prod me on. Her collaboration with my parents has finally yielded results with getting the work done. I am but a small cog in the works.

I would also like to acknowledge the Department of Energy for their financial support for this work.

Table of Contents

List of Tables

Table

List of Figures

Figure

List of Appendices

Appendix

List of Symbols

C	Species concentration
C^*	Surface species concentration
C^i	Inlet species concentration
C_P	Specific heat at constant pressure
d_1	Reaction channel diameter
d_2	Control channel inner diameter
d_3	Control channel outer diameter
Ea	Activation energy
ΔH_R^0	Heat of reaction
h	Convective heat transfer coefficient
k_{CO}	Rate constant for CO oxidation
k_{W}	Thermal conductivity of wall material
L	Length of the reactor
M	Atomic weight
$\dot{m}$	Mass flow rate
p	Partial pressure
r	Rate of reaction
R	Universal gas constant
S	Selectivity of CO oxidation
T	Temperature

T_0	Room temperature
V	Volumetric flow rate
V_0	Volumetric flow rate at room temperature
v	Flow speed
W	Weight of catalyst
$\alpha,\ \beta$	Rate law exponents for CO oxidation
$\dot{\Omega}$	Molar reaction rate
χ	Dispersion of catalyst
ρ_{bed}	Packing density of catalyst bed
θ	Weight fraction of metal in catalyst
ψ	Surface-to-volume ratio
κ	Mass transfer coefficient

Subscripts

W	Wall
R	Reaction channel flow
C	Control channel flow
∞	Ambient
0	Room temperature

Superscripts

0	Left hand side boundary condition
L	Right hand side boundary condition

Abstract

Liquid hydrocarbons are high energy density fuels, and micro-reactor based fuel processors are viable alternatives to generate hydrogen for portable fuel cell applications. Micro-reactors have high mass and high heat transfer rates due to their small length scales. However, they suffer from thermal heat retention problems due to large surface area to volume ratios. This thesis attempts to explore methodologies to make micro-reactors thermally efficient. The approach is by use of a counterflow heat exchanger configuration for heat recuperation, and quantifying parameters by which operation of the system can be controlled and optimized.

In the first part, a simulation of the preferential oxidation(PrOx) catalytic reaction is setup in a cylindrical channel. The channel is contained within a counterflow heat exchanger to recuperate excess heat. Performance of the system is evaluated by using the concept of reactive length and thermal efficiency. The ratio of the channel used for 95% of net conversion of CO is defined as reactive length. Thermal efficiency is defined as the ratio of heat recuperated to the total heat available. The PrOx reaction model is verified by comparing simulation with experimental data.

A parametric study then is performed using parameters such as mass flow rates, inlet temperatures, thermal conductivity, PrOx selectivity, mass of catalyst and inlet concentrations. Significant parameters by which the system can be controlled effectively are identified. Parameters such as the inlet temperatures that directly affect the systems enthalpy are found to be the most effective. The remaining parameters have a smaller effect, but can be used to fine tune the operation of the system. The control mass flow rate can be used as an active control during operation.

In the second part, simulation is employed to understand the flow and thermal characteristics of two types of micro-reactors: silicon based and channel based micro-reactors. For silicon substrate micro-reactor, it is found that the flow mixes and redistributes itself due to high mass transfer limits. The temperature is uniform in the substrate due to high thermal conductivity of silicon. CFD simulation is able to predict these temperatures within the silicon micro-reactor to 5% accuracy. The silicon micro-reactor is compared against a packed-bed reactor and is found to operate comparable due to similar length and time scales. A 1-D reaction model is also able to predict the conversion trends in both the packed-bed and silicon micro-reactors. Collapsing a 2D temperature field to an average temperature underestimates the reaction rates and conversion since the Arrhenius kinetics are exponential with temperature.

The channel based micro-reactor design consists of three generations of fuel processors that are constructed and demonstrated by the University of Michigan fuel processor team. The first generation is a proof of concept for channel flow micro-reactors, while the second generation uses discrete reactors(ATR, WGS & PrOX) for each processor stage. The second generation processor performed to specifications but required external power to maintain operation. The third generation fuel processor combines these separate stages into a single physical package giving a thermally integrated fuel processor with internal heat recuperation. A continuous self-sustaining operation of the third generation fuel processor is demonstrated over extended periods of time. Thus showing that a thermally integrated iso-octane fuel processor can be built with self-sustaining capabilities. There are potential applications for such micro-reactor based fuel processors as portable electronics, military hardware, quick recharge devices and more.

Chapter 1

Introduction

1.1 Motivation

Energy is what makes the world go around in our current society and lifestyle. It drives everything from growing our food, to processing it, from transportation to entertainment, from heating our homes to recreation. It sustains the economic growth and the commerce of the world. Every energy crisis in the past century has shown us our dependence on energy. Without energy everything will come to standstill. It is of little surprise, that the world uses an enormous amount of energy. The United States has and annual energy costs of more than 1 trillion dollars. Non-renewable sources of power, such as coal, oil and gasoline provide about 90% of the electrical power with coal providing almost half[1, 2]. Renewable sources such as hydro-electric, wind, etc. do provide a sizeable portion of our energy requirement and are growing, however non-renewable sources of energy are limited and will not be able to satisfy our every increasing needs of energy and power.

Over time as we have increased our energy usage, the scarcity of the non-renewable power sources(coal oil, natural gas) has driven the cost of energy higher and higher. Peak Oil is near or has happened depending on whom you ask[3]. In either case it is fairly clear that the costs of energy are on a ever upward spiral. Along with the higher costs of fossil fuels based energy, these are also inherently dirty. They are notorious for pollution of earth and burning them produces pollutants such as carbon dioxide, sulphur dioxide, nitrogen oxides(NOx) and particulate matter along with many others[4].

In our energy budget, transportation and automobiles consume the largest share of non-renewable fossil fuels. They contribute towards a major portion of the worlds emissions and fossil fuel usage accounting for almost 30% of our energy usage along with 95% of global oil consumption[2]. Transportation based on oil using internal combustion is about 20% efficient[5]. If we take into account the well to wheel efficiencies, they are even lower[6]. Automobiles and other engines the worst polluters. Even though emission regulations exist, the better method would be to replace the original power generated though combustion with alternate sources and methods. Thus there is a need to develop cleaner and efficient methods of alternate power sources of automotive and mobile applications.

With our power consumption rates following exponential growth, we simply cannot satisfy our needs for a long period of time. At some point demand would outstrip supply. Clearly we do need to develop alternate sources of energy. Along with developing renewable sources of power such as wind, hydro-electric, etc. we also need to improve our current systems of deriving energy from fossil fuels. Not only do we need to increase the efficiency of our current systems, we have to also overhaul our energy extraction and conversion systems to make them non-polluting by design and not by use of after-treatment systems. The after-treatment systems impose a cost as well as efficiency penalty.

In the new millennium, there is a strong research interest in the development of power generation devices based on hydrogen. Hydrogen is believed to have a great potential to provide high energy density with more improved efficiency and almost zero emissions[7].

Fuel cells are a promising technology to generate clean energy from oxidizing hydrogen into water. Since only pure water is produced as a product is a very clean method of generating power. Solid-Oxide fuel cells have existed from quite a while, however, they need a high temperature of 500–1000°C to operate efficiently. Proton exchange membrane(PEM) fuel cells operate at around 70–80°C [8, 9] and combine hydrogen gas at the anode, with oxygen at the cathode to generate useful electric power at a high efficiency. Since these are electro-chemical systems, they avoid the thermodynamic mechanical cycle losses encountered in conventional power generation, while emitting only water as the exhaust. This technology thus helps to conserve fossil fuels and provides a more environmental friendly exhaust emission than the existing internal combustion engine system. The use of proton exchange membrane fuel cell systems to obtain clean and efficient power for stationary as well as mobile applications has gained prominence over the last few years[7].

In automotive applications, hydrogen can be utilized as a direct fuel for the internal combustion engines or as a source of electricity using fuel cell systems. In particular, fuel cells have attracted attention from industries, such that virtually every major automotive manufacturer currently explores a research program to develop fuel cell systems for automobiles[10].

It may be noted that the ultimate goal in the development of the on-board fuel cell power system for automotive application is to reduce emissions at a comparable, or better, efficiency as the state-of-the-art internal combustion engines with after-treatment systems. The conventional hydrocarbon engines produce a significant amount of NOx and particulates, thereby facing a serious challenge in meeting the ever more stringent emissions regulations. In comparison, the fuel cell system is inherently free of such combustion-generated pollutants. It is also anticipated that the fuel processor can subsequently reduce the pollutant formation by efficient and better-controlled catalytic reaction processes.

One of the major challenges in the development of hydrogen fuel cell technology is the on-board storage of hydrogen; its low density requires extremely high pressure or low temperature or other expensive means to store a practical amount of fuel[7]. Various methods for effective hydrogen storage are being explored, such as metal hydride, carbon nanotubes and glass micro-spheres[11, 12]. As an alternative, a viable option is the on-board generation of hydrogen by reforming other conventional hydrocarbon fuels[13]. This can be accomplished by catalytic reactors places in series which would include desulpherizing, reforming(ATR), water-gas shift (WGS) and CO clean up(PrOx).

Proton exchange membrane fuel cells are hindered from the fact they require very low CO concentration in the feed to operate properly. Concentration in the range of tens of ppm is required[14, 15]. Any excess CO in the feed will poison the render the fuel cell in-operative. To this effect, many technologies can be utilized to oxidize CO into harmless carbon dioxide. These range from pressure and temperature swing absorption(PSA/TSA), methanation, membrane separation and preferential oxidation(PrOx) among others. The former methods, PSA and TSA are energy intensive and expensive. Methanation converts each mole of CO into methane utilizing three moles of hydrogen. Preferential oxidation oxidizes the CO using oxidation catalysts. Some hydrogen also gets oxidized in this process and hence selectivity of the chosen catalyst is very important. Preferential Oxidation also uses small amounts of oxygen and hence PrOx is the preferred technology. PrOx is being widely implemented in fuel processor systems for CO cleanup[16].

For automotive and mobile applications, there is an obvious constraint on size and weight for fuel reformers due to packaging reasons. General Motors recently did a prototype where the complete carrier trunk in a truck was fitted with a fuel reformer system. Since this would not be feasible economically, it is important that we reduce the size of the system to as small as possibly while still retaining the functions as well as the system efficiency. Keep in mind that for automotive applications, we would have to beat the efficiency and economic costs for a regular internal combustion engine to be economically viable.

Micro-reactor technology is being used more and more to miniaturize conventional reactive systems while providing the same through-output and efficiency.[17]. Several micro-fabrication techniques are available which can be used to fabricate different designs most suited for a particular application[18]. The advances in micro-reactor technology has been very promising. Various research groups such as Institut für Mikrotechnik Mainz (IMM)[19], Forschungszentrum Karlsruhe GmbH (FK)[20], Massachusetts Institute of Technology (MIT)[21, 22], The University of Michigan[23] and Pacific Northwest National Laboratory (PNNL)[24] have all been very active in micro-reactor development over the past many years.

Additionally the micro-reactor design yields a reduction of diffusive transport limitations. This gives high heat and mass transfer rates and well mixed characteristics of the fluids within[17, 25]. With the physical scales being so small, heat transfer rates within separate channels is enhanced to high rates such that at times it is difficult to maintain a temperature differential between neighboring features. Coating the walls of the micro-reactor with catalytic materials lets us make catalytic reactors. Compared to packed-bed reactors, a wash-coated micro-reactor has a much smaller pressure drop for the same catalyst amount.

Scale up of micro-reactors is much simpler with a simple numbering up of the reactors instead of redesigning a higher capacity reactor. Reactors can be chained either in serial or parallel to achieve the configuration required. Micro-reactor technology is maturing very quickly. Based on the above advantages and available new fabrication techniques, widespread use of micro-reactor based systems is a reality.

Although the basic catalytic reforming process for common hydrocarbon fuels has been developed, its application to on-board systems involves many additional constraints of size and weight limitations. This implies that the on-board fuel reformer must be compact and light-weight, which necessitates high efficiency and reduced heat loss via careful packaging. To achieve this goal, it is thus necessary to undertake a synergistic research effort toward development of better catalytic material, better reactor component design, and careful integration of the components for optimal thermal management. This thesis attempts to further understand and achieve these goals by analytical tool development and prototyping micro-reactor based fuel reformer systems.

The University of Michigan fuel processor group is a multi-disciplinary consortium of research groups with diverse research expertise in this endeavor. The objective of this research is to develop a compact fuel processor system that delivers 1kW/kg, yet is small enough to be incorporated as an on-board power generation device. The success of such a miniaturized design relies on effective catalytic materials and micro-channel based reactor designs to maximize the hydrogen yield, and efficient thermal integration that allows recuperation of excess heat from exothermic to endothermic components within the system.

1.2 Scope of Work

The scope of this dissertation is primarily focused on the design, modeling, and thermal integration of a fuel processor system. The attempt is on to try and use micro-reactor systems to develop a compact fuel processor capable of generating clean hydrogen that can be utilized in a PEM fuel cell for electric power generation. The aim is specifically to model, predict and construct a thermally efficient micro-reactor based fuel processor system and demonstrate its operation over a substantial period of time.

In Chapter 2, the workings of a fuel processor are discussed. The chapter talks about the layout and working of a general fuel processor which generates hydrogen from iso-octane. The steps required to convert iso-octane into hydrogen are discussed one by one. This is accomplished by a series of catalytic reactions including fuel desulfurizaion, steam/autothermal reforming, water gas shift and residual CO clean-up. CO clean-up is an important step to protect the PEM fuel cell membrane. This can be performed in a number of ways including pressure swing adsorption (PSA), methanation and preferential CO oxidation (PrOx). However, PSA is energy intensive and expensive, while methanation involves hydrogenation of the CO which consumes three moles of hydrogen for every mole of CO that is cleaned up. Hence, PrOx is the primary technology of preference[26]. Typically, PrOx catalysts contain an active metal such as Pt, Au, Cu, etc. on an oxide support such as alumina[26–28].

Chapter 3, discusses a comprehensive modeling strategy that was initiated by the need to model various components at different levels of detail. A generalized modeling approach prevents repetition and redundancy among various components, thereby achieving more effective design and development processes. In this dissertation, two types of modeling efforts are undertaken concurrently: (a) simplified thermal integration models, and (b) detailed three-dimensional simulations of individual components. While it would be ideal to combine both detailed and system level models into one large integrated modeling tool, this is cost-prohibitive and is not necessarily the most effective way. Therefore, a practical and reasonable option is to pursue both paths independently, and provide feedback and guidance to each other. Hence in Chapter 3, a one-dimensional counterflow heat exchanger model will be presented as a canonical configuration to analyze thermal interaction between two components. Since catalytic reactions are very sensitive to temperature, it is critical to maintain the desired temperature level within the flow while heat is transferred from exothermic to endothermic reactors. Heat has to be recovered from exothermic reactors for better thermal efficiency. Studies are performed to identify optimal design conditions that satisfy the target. One of the main challenges in this task is the lack of knowledge of the detailed chemical kinetic rates associated with individual reactions in the reactor components. Thus, a significant amount of effort is put into extracting the kinetic data based on the experimental measurements, resulting in semi-empirical kinetic rate constants used in the component models. The PrOx reaction is then chosen to be applied to this model.

Chapter 4, underlines the suitability of micro-reaction technology for the development of compact fuel processing systems as compared to packed-bed reactor technology which does not scale down in a feasible manner. A micro-channel reactor is fabricated in silicon using standard micro-fabrication tools. A 2% Pt/Al_2O_3 catalyst is wash-coated on the micro-reactor channel walls. Preferential CO oxidation in hydrogen is chosen as a model reaction and the results were compared with those obtained from a conventional packed-bed micro-reactor. Issues of scale-up and efficient heat integration have also been addressed.

In Chapter 5, the concept of scalable silicon micro-reactor demonstrated in Chapter 4 is extended with an integrated thin-film platinum heater. This setup is again modelled and developed for preferential CO oxidation. The performance of the micro-reactor is assessed and compared to a packed-bed reactor model. Complimentary experimental and modeling efforts are made to identify the optimal thermal design parameters. Experimental measurements using the fabricated reactors are compared with the simulation results in order to assess the overall performance of the new micro-reactor design.

In Chapter 6, three-dimensional computational fluid dynamics (CFD) codes are used to simulate the flow and thermal characteristics of various individual components as well as an integrated fuel processor. The Fluent CFD package is used to design and simulate a detailed geometric configuration of the individual reactors comprising the fuel processor system. In all, three successive generations of the fuel reformers are designed, modelled, built and studied. The effective use of modeling results to support the experimental developments has been demonstrated in detail in this chapter. Results and summary from each of the builds is detailed.

Finally, in Chapter 7, the findings are summarized along with some recommendations for future work.

Chapter 2

Fuel Processor

Hydrogen has been hailed as the clean fuel for the coming millennium. Not only does hydrogen posses a very high calorific value, it also burns extremely cleanly to generate only water as its byproduct. Fuel cells utilize hydrogen to generate electricity efficiently and cleanly. However, hydrogen has problems of its own that need to be addressed. Being a very low density gas, hydrogen requires either large tanks for its storage or very high pressure tanks which reduces the overall efficiency of the system and pose an explosion risk. Furthermore, transportation of hydrogen requires larger and pressurized containers as compared to liquid fuels for the same energy which lowers the effective use of hydrogen. Hence, to store hydrogen effectively, innovative methods are being developed such as metal hydrides storage[29], carbon nanotubes[30], on-board hydrocarbon reforming[31], etc.

Instead of storing hydrogen, an option is to generate hydrogen on-board to meet the fuel demand on a need to basis. Hydrogen can be produced on-board in a number of methods. One of the most viable method is breaking down of liquid hydrocarbon fuels into hydrogen. Converting higher hydrocarbons to hydrogen can be done through a number of processing steps in a fuel processor. A gasoline fuel processor can generate hydrogen by utilizing off-the-shelf gasoline. It uses sequential reactors to first generate hydrogen and then cleans the reformate removing excess carbon monoxide(CO). The cleanup process is important since excess CO poisons the membranes of a PEM fuel cell, rendering the fuel cell inoperative. The cleanup can be accomplished by use of water gas shift(WGS) reactors and preferential oxidation(PrOx) reactors. For PEM fuel cells the CO content in its hydrogen supply must be below 10–50 ppm. Alternatively, a PEM fuel cell can be replaced with a solid-oxide fuel cell(SOFC) which is not susceptible to CO poisoning. Hence, a relatively compact SOFC fuel cell can be designed by eliminating the CO cleanup process.

2.1 Layout of a fuel processor

Generally, the fuel processor system comprise of many individual reactors linked sequentially to form a complete system. Ideally, the complete system should be packaged in a small integral manner, so as to reduce the physical weight and size. Furthermore, this reduces the surface area to volume ratio, decreasing the heat loss and increasing the overall efficiency of the system. However, the startup and control of such integrated systems is a challenging task leading to simpler designs with individual sequential reactors.

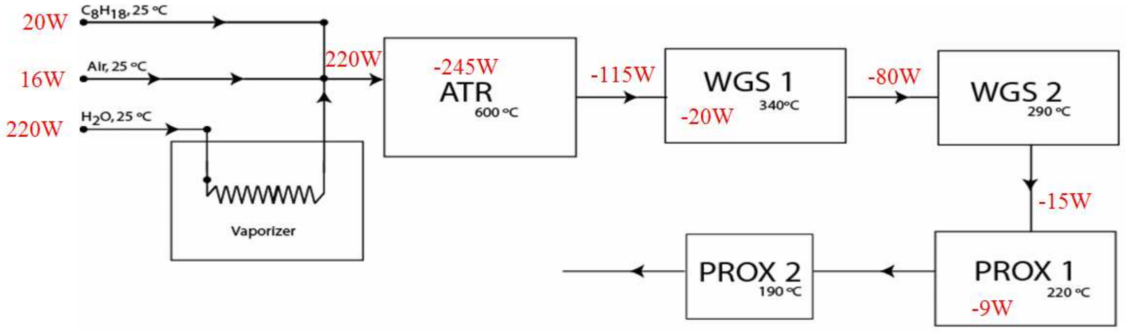

Figure 2.1: Schematic of an iso-octane fuel processor

Figure 2.1 shows a schematic of a typical fuel processor. The system consists of a series of components: a Desulpherizer/filter, a combustor/vaporizer, a reforming reactor, a water gas shift reactor, and a preferential oxidizer. First, the fuel is filtered in a Desulpherizer/filter. The filtered fuel is then mixed with water and air which are supplied to the vaporizer in which the mixture is then vaporized. Depending on the design of the system either a separate vaporizer for the water might be utilized or water could be fed directly into the reforming reactor. In either case, the feed is then fed into the reforming reactor where most of the fuel gets converted to hydrogen. The reformate contains a considerable amount of carbon monoxide, which needs to be cleaned as it contaminates the anodes in a PEM fuel cell. The desired level of the CO concentration for a PEM fuel cell is below 10 ppm. To meet this target, the next two components, a water gas shift (WGS) and a preferential oxidation (PrOx) reactors are utilized. WGS reaction lowers the CO concentration to around 500 ppm, and PrOx subsequently reduces it closer to the desired 10 ppm. The resultant stream is fed into the fuel cell to generate electricity. The exhaust from the fuel cell contains some amount of hydrogen which is recycled into the vaporizer as a fuel for generating heat to vaporize water and fuel in the feed stream. The vaporizers utilizes a Platinum based oxidizing catalyst to combust hydrogen and to generate heat.

Fuel filter/Desulpherizer Depending on the fuel used, there are various impurities in fuel which needs to be removed before the fuel is reformed. For example, gasoline comprises of a number of compounds[32] such as sulphides, thiophenes, thiols, etc. To remove these impurities the fuel is passed through a Desulpherizer which reduces the sulphur content by adsorption through sorbets[33, 34].

Reformer Reformer is the main component in the fuel processing system which converts most of the fuel into hydrogen. There are three main fuel reforming techniques: steam reforming, partial oxidation and autothermal reforming. The steam reforming technique converts fuel by reacting it with steam in the presence of a catalyst, as shown in Eqn. 2.1. This method is a highly endothermic reaction with the highest hydrogen yield from fuel. The conversion in this reaction depends on the temperature and heat supplied to the reactor.

$$\mathrm{C_8H_{18}} + 8\mathrm{H_2O} \rightarrow 8\mathrm{CO} + 17\mathrm{H_2} \qquad \Delta H = 1274\ \mathrm{kJ/mol} \tag{2.1}$$

Partial oxidation method provides combustion of fuel in a fuel rich regime as shown in Eqn. 2.2. This method is self sustaining and exothermic with low hydrogen yield. However, controlling this reaction is difficult and can produce localized hot spots due to uneven fuel distribution in the reactor. It is also prone to coking and soot formation due to operation in the fuel rich regime.

$$\mathrm{C_8H_{18} + 4O_2 \rightarrow 8CO + 9H_2} \qquad \Delta H = -660\,\mathrm{kJ/mol} \tag{2.2}$$

The next technique to generate hydrogen using a reforming reactor is a combination of the previous two methods known as autothermal reforming (ATR)[35]. Combining Eqns. 2.1 and 2.2 in various ratios to operate in different regimes is described in Eqn. 2.3.

$$\mathrm{C_8H_{18}} + x\mathrm{O_2} + (8-2x)\mathrm{H_2O} \rightarrow 8\mathrm{CO} + (17-2x)\mathrm{H_2} \tag{2.3}$$

For a value of x closer to zero, the reaction tends towards the steam reforming reaction and for a value closer to four the reaction is a partial oxidation reaction. Hence, autothermal reforming lies between the two techniques and all the feed streams are mixed together in a single reactor. Some fraction of the fuel is oxidized to provide heat for the steam reforming reaction and the remaining is converted to hydrogen. Hydrogen yield from this method lies between steam reforming and partial oxidation. This autothermal reforming reaction can be controlled effectively by controlling the amount of fuel, air and water streams entering into the reforming reactor. Hence, by varying the steam to carbon ratio(H_2O/C) and oxygen to carbon ratio(O/C), the reforming reactor can be used in different applications.

Water Gas Shift Reactor (WGS) WGS is a preferred technique for CO reduction and increasing hydrogen yields. The reaction for WGS is described by Eqn. 2.4. However, WGS is an equilibrium limited reaction. The rate of reaction is higher at high temperatures, but the equilibrium is shifted towards the CO side *i.e.* the reaction reaches equilibrium quickly, but a large amount of CO remains unreacted. At lower temperatures, the equilibrium is favorable to full CO conversion, however the reaction rates are slow. Thus, to achieve high conversion of CO, the WGS reaction is generally divided into two stages: a high temperature shift(HTS) and a low temperature shift(LTS). The HTS converts the major amount of CO to H_2 at higher reaction rates and the LTS drives the CO conversion rates higher.

$$\mathrm{CO} + \mathrm{H_2O} \rightarrow \mathrm{CO_2} + \mathrm{H_2} \qquad \Delta H = -41\,\mathrm{kJ/mol} \tag{2.4}$$

Care must be taken for the high temperature shift reaction since higher temperatures, can lead to reverse WGS reaction and production of undesirable products like methane.

Preferential Oxidation (PrOx) As mentioned earlier, for PEM fuel cells the CO in the reformate stream should be below 10 ppm. The PrOx reactor oxidizes the remaining amount of CO entering from the previous reactor in presence of a Platinum catalyst while trying not to oxidize the hydrogen in the reformate stream. The process consists mainly of two reactions:

$$\mathrm{CO} + \frac{1}{2}\,\mathrm{O_2} \rightarrow \mathrm{CO_2} \qquad \Delta H = -280\,\mathrm{kJ/mol} \tag{2.5}$$

$$\mathrm{H_2} + \frac{1}{2}\,\mathrm{O_2} \rightarrow \mathrm{H_2O} \qquad \Delta H = -240\,\mathrm{kJ/mol} \tag{2.6}$$

An efficient oxidation catalyst can reduce the CO levels as desired, but it is very difficult to prevent the hydrogen from getting oxidized since the concentration of hydrogen in the gas stream is much higher. In practice, an oxidation catalyst can be called good if it oxidizes less hydrogen than CO on a molar bases. This selective efficiency of the catalyst is known as selectivity and is generally defined for the PrOx catalyst as number of moles of CO oxidized divided by the total number of moles of CO and hydrogen oxidized together. The efficiency of the PrOx reactor is sensitive to the amount of CO in the inlet gas stream.

2.2 Micro-reactors for fuel processing

The technology for fuel processing of liquid hydrocarbon fuels into hydrogen exists and is used by industry to produce bulk quantities of hydrogen. This hydrogen is then bottled in cylinders and distributed. However, storage of hydrogen is a cumbersome process requiring large cylinders at very high pressure. The compression of hydrogen during the storage process requires work and lowers the overall efficiency of the system. Thus, the concept of on-board generation of hydrogen by employing catalytic micro-reactors is advantageous.

Catalytic micro-reactors are well suited as components in portable fuel processors for hydrogen production in a variety of mobile applications [17, 36]. Compared to conventional packed-bed reactors, their high mass-transfer limits [31] and compact size offers numerous advantages in terms of efficiency and ease of scale-up. One of the main challenges in micro-reactor designs is increased heat loss due to their large surface-to-volume ratios. An external heat source is required to maintain high temperatures in the reactors, which leads to a bigger system size as well as decreased thermal efficiency, limiting the advantages of the overall concept. However, recognizing that a typical fuel processor system consists of both endothermic and exothermic reactor components, these problems may be significantly overcome by recuperating excess heat from one part of the system and utilize it in another.

Table 2.1 shows the approximate heat duty for various components and processes for a 500 Watt iso-octane fuel processor. While some heat will be recovered from the combustion of the waste Hydrogen from the exhaust of the fuel cell, this number is difficult to estimate since it depends on the efficiency of the fuel cell. Positive values denote heat required by the reactor or function and the negative values show excess heat that can be recovered from the various components or functions. Kolb *et al.*[37] demonstrate a working $5\mathrm{kW}$ iso-octane fuel reformer system. They employ concurrent heat recovery for the WGS and PrOx reactors and also between the ATR and WGS reactors. However all reactors in the

Process	Heat Duty (W)
Vaporize fuel	20
Vaporize water	220
Heat Air	16
Heat to ATR inlet(650°C)	220
ATR	-245
Heat recovery before WGS	-115
HTS reactor	-20
Heat recovery before LTS	-80
LTS reactor	-9
Heat recovery before PrOx	-15
Prox reactor	-9
Combustion recovery	
Total	-32

Table 2.1: Heat duty of an 500W iso-octane fuel processor

system are discrete and external heat input is provided for feed heating and vaporization. Even though the heat duty of the system is slightly exothermic, systemic heat losses to the ambient surroundings causes the system not to be self-sustaining. Hence external heat, either in form of preheating the feed, or heating the device itself needs to be used.

In order to make the system more efficient, thermal integration of all the devices is a necessary step. Besser[38] proposes a cylindrical methanol reformer with all the components in a single physical package. The hottest reformer is placed in the middle with the other reactors layered around. Hence, the system needs to be designed in a very compact and integrated manner so as to reduce the surface area to volume ration of the system. Not only will the thermal integration allow for higher thermal efficiencies, the compactness will lower the weight of the system, making it lighter and cheaper to build.

The challenging aspect in an integrated design is controlling the heat flow from one device to the other while achieving good reaction rates. To achieve this goal, it is necessary to develop a systematic integration strategy to determine an optimal design under various different operating conditions. This goal of coupling two separate reaction channels, one exothermic and the other endothermic is described in Chapter 3. Northrop *et al.*[39] designed a prototype methane reformer using a counterflow arrangement to recuperate heat from WGS and PrOx sections using heat of vaporization of water as a control. The ATR was not used to recuperate heat from. Similar prototype systems have been designed and operated[40–42] where heat is recuperated by use of heat exchanger between reactor components to increase thermal efficiency.

As with any system, micro-reactors has its own set of advantages and limitations when compared to other systems.

Advantages of micro-reactors

- Micro-reactors with wall coated catalysts have a much smaller pressure drop as compared to packed-bed reactors.
- Higher mass transfer and mixing characteristics then conventional packed bed reactors.
- They are compact and portable.
- They can operate for longer periods between refueling/recharging as compared to battery based systems.
- Easy scale up by increasing the number reactors in the system and setting them up in parallel.
- Micro-reactors operate much cleaner with low emissions since the reactions are catalyst based and have no flame front.

Limitations of micro-reactors

- They have lower power densities (power/weight) as compared to IC engines. In smaller devices the micro-reactor based fuel processor might be favorable.
- The hydrogen yields are lower as compared to full sized reforming plants.
- They have higher thermal losses due to high surface to volume ratios.

- They have large startup and shutdown times.
- Startup sequences might be complicated to prevent contamination of downstream stages.
- Complicated manufacturing and sealing at the high temperatures due to the small size.

To be feasible in the market, a micro-reactor based fuel processor needs to achieve efficiency levels of at least that of conventional on-board power generation methods. For example, to power an automobile, the fuel processor needs to match the efficiency of an internal combustion engine. For smaller portable applications, a penalty on efficiency might be acceptable for increased portability and a higher power density.

Chapter 3

The Counterflow Micro-reactor

A micro-reactor has the main advantage of being a portable device, but it suffers from its inability to retain heat due to its low heat capacity and large surface area to volume ratio. This results the micro-reactor systems to have a high heat loss and a low thermal efficiency. There are a few techniques using which thermal efficiency of micro-reactor system can be increased. The easiest method would be to increase the size and capacity of the system. This decreases the surface area to volume ratio making the system sustainable. However this constraints the systems portability which is undesirable. Hence in order to design a fuel reforming system by the use of micro-reactors, a novel technique to make the micro-reactors self-sustaining is required.

As noted in Chapter 2, a typical fuel processor consists of both endothermic and exothermic reactor components, heat might be recuperated from the exothermic reactors and provided either to the endothermic reactors or utilized to preheat the input feed streams to the system. Hence even though there are endothermic reactors present in the system, the overall system can be self-sustaining without the need of any external heat. This necessitates thermal integration between the components of the fuel processor. This has the further advantage that the system will be compact is size.

This Chapter will focus on the technique technique to recover heat and preheat feed streams in order to improve the thermal efficiency of the system. In case of reactive systems, such as a fuel processor, care needs to be taken to implement the heat recuperation strategy with minimal effect on the chemical conversion efficiencies. Towards the aim of increasing the thermal efficiency, this chapter discusses a systematic modeling approach developed as a tool to undertake a parametric study to identify crucial design parameters. A reactive counterflow heat exchanger system is studied and modeled. The effects of key system parameters, such as reactant, control flow rates, inlet temperatures, rate of conversion, and reactive length are investigated. The model is developed as a system of coupled ordinary differential equations which are integrated numerically, allowing a parametric study to assess various system design concepts.

In the following sections, the formulation of the mathematical models for the heat exchanger and chemical reactions is described. As a specific application example, the model is applied to a thermal integration between a preferential oxidation (PrOx) reactor and a control feed. Various aspects of the system performance characteristics are examined, such as flow rate and the inlet temperature. Do keep in mind in a real micro-reactor system, there are far too many parameters to do a full parametric study. For a full modeling analysis of a micro-reactor device, a full 3D CFD simulation is still recommended. This method tries to implement a first principles fundamental model that is inexpensive to model and can generate results in quick time. Similar work for the water gas shift(WGS) reactions has been performed by Kim *et al.*[43].

To get the maximum conversion efficiency out of a reactive system, initial thought point towards an optimum isothermal reactor temperature. However, this is wasteful from a thermal standpoint and is difficult to achieve. It would be worthwhile to relax the isothermal requirement and examine the overall impact of temperature profiles on the product yield and thermal efficiency of the device. The derived temperature gradient might even be advantageous in a reactor like the water shift reactor where the higher temperatures give higher reaction rates and lower temperatures shift the equilibrium favorably. Thus the HTS and LTS reactors might even be combined into a single reactor reducing size and weight of the system.

3.1 Model description

The model is developed in two steps. First the counterflow heat exchanger model is developed. The reactive kinetic model is then further added onto the heat exchanger model and integrated to give the complete model.

3.1.1 Heat Exchanger Model

The heat exchanger model adopts a concentric counterflow 1-D configuration. The reactants flow through the inner channel(left to right) and the control stream flows in the outer concentric channel in the opposite direction(right to left). The temperature in the reactants and control flows are denoted by $T_{\mathrm{R}}(x)$ and $T_{\mathrm{C}}(x)$, respectively as a function of the location down the length of the heat exchanger. The two channels are separated by a wall of finite thickness. The wall temperature on the reactor side surface is given by $T_{\mathrm{W,R}}(x)$. Similarly $T_{\mathrm{W,C}}(x)$ gives the temperature of the wall on the control flow on side.

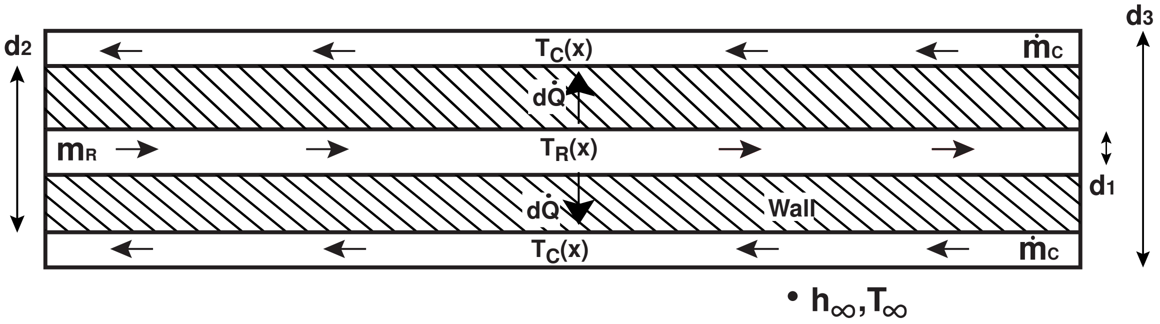

Figure 3.1: Model configuration: Concentric counterflow reactor

For setting up the equations for the model the following assumptions are made:

1. 1-D model in the axial direction, with no radial variations(axi-symmetric)
2. Constant specific heats of the fluids (C_{PR} and C_{PC})
3. No heat conduction axially in either of the reactant or control fluids
4. No phase change

5. The wall separating the reactant flow and control flow is thermally thin: $T_{\mathrm{R}} - T_{\mathrm{C}} \gg T_{\mathrm{W,R}} - T_{\mathrm{W,C}}$

6. The convective heat transfer coefficient between the reactant fluid and the walls on both sides as well as the heat transfer coefficient between the control fluid and its walls is assumed to be a constant and is denoted by h.

Reasoning for the above assumptions are explained below.

The flow in the channel is laminar at Reynolds number on the order of 500. For the thermal radial gradients, since the flow is laminar a parabolic profile for the radial thermal gradients will exist. This is captured in the model by the use of the correct Nusselt number correlations[44] to account for the correct heat transfer rates. For the temperature at which the reaction occurs in the reaction channel, the average temperature of the channel is then utilized.

The 1-D counterflow PrOx micro-reactor model is developed as a plug flow model. The plug flow model is applied to both temperature gradients as well as the concentration gradients in the axial direction. The thermal Péclet number for a typical case is calculated to be around 60. Hence conduction of heat in the axial direction can be neglected. For species concentration the typical Péclet number is calculated to be around 900. For these large Péclet numbers the diffusion of species in the axial direction can be neglected. In other words the dependency of the flow on downstream locations is diminished and the temperature and concentration variables are ‘one-way’ properties. Thus the simpler plug flow model is employed.

For gas mixtures, the specific heat can be calculated by taking the weighted average of the component gases. In the current model, the maximum change in composition can approach 1% when conversion approaches 100%. In other words even at complete conversion, the CO composition will change from 1% to 0%. For this small change, the change in specific heat will be very small. For partial conversion then change in composition will be even smaller. Hence the specific heat for the gas mixture in the reaction channel and control channels can be taken as a constant.

In the model, the temperatures simulated in the reaction channel are in the range of 380 K to 470 K. In this range, all the species, including water are primarily in the gaseous state. Hence the assumption that only the gaseous phase exists is reasonable.

For the counterflow model, heat is transferred from the reaction channel to the control channel. In order to do so, heat must pass through the reaction channel-wall interface(convection), the wall itself(conduction) and then the wall-control channel interface(convection). For a typical case, the thermal resistance provided by the fluid-wall interfaces comprises of 98% of the total thermal resistance. Further, given the heat transfer rates, the temperature drop over the wall is in the range of 2 K while the total temperature drop from the reaction channel to the control channel is in the range of 100 K. Thus the wall is denoted to be thermally thin in the model[45].

For long channel with constant flow conditions, the Nusselt number is a constant. Given $Nu = hD/k$ and the diameter is constant along with the conductivity of the fluid which varies only slightly, the local heat transfer coefficient is taken as a constant over the length of the channels.

Deriving the energy conservation equations for the wall, the reaction channel and the control channel over a small control volume in the x co-ordinate(Figure 3.1), we get:

$$\frac{k_{\mathrm{W}}}{4h}(d_2^2 - d_1^2)\frac{\mathrm{d}^2 T_{\mathrm{W}}}{\mathrm{d}x^2} = -d_1(T_{\mathrm{R}} - T_{\mathrm{W,R}}) + d_2(T_{\mathrm{W,C}} - T_{\mathrm{C}}), \tag{3.1}$$

$$\frac{\dot{m}_{\mathrm{R}} C_{\mathrm{PR}}}{\pi h d_1}\frac{\mathrm{d}T_{\mathrm{R}}}{\mathrm{d}x} = -(T_{\mathrm{R}} - T_{\mathrm{W,R}}), \tag{3.2}$$

$$\frac{\dot{m}_{\mathrm{C}} C_{\mathrm{PC}}}{\pi h d_2}\frac{\mathrm{d}T_{\mathrm{C}}}{\mathrm{d}x} = -(T_{\mathrm{W,C}} - T_{\mathrm{C}}) + \frac{h_\infty d_3}{h d_2}(T_{\mathrm{C}} - T_\infty). \tag{3.3}$$

Following Ronney [45], adding and subtracting Eqns. (3.2) and (3.3) yield:

$$\begin{aligned}\frac{\dot{m}_\mathrm{R} C_\mathrm{PR}}{\pi h d_1} \quad & \frac{\mathrm{d}T_\mathrm{R}}{\mathrm{d}x} + \frac{\dot{m}_\mathrm{C} C_\mathrm{PC}}{\pi h d_2}\frac{\mathrm{d}T_\mathrm{C}}{\mathrm{d}x} = \\ & (T_\mathrm{W,R} + T_\mathrm{W,C}) - (T_\mathrm{R} + T_\mathrm{C}) + \frac{h_\infty D_3}{h d_2}(T_\mathrm{C} - T_\infty), \qquad (3.4) \\ \frac{\dot{m}_\mathrm{R} C_\mathrm{PR}}{\pi h d_1} \quad & \frac{\mathrm{d}T_\mathrm{R}}{\mathrm{d}x} - \frac{\dot{m}_\mathrm{C} C_\mathrm{PC}}{\pi h d_2}\frac{\mathrm{d}T_\mathrm{C}}{\mathrm{d}x} = \\ & (T_\mathrm{W,R} - T_\mathrm{W,C}) - (T_\mathrm{R} - T_\mathrm{C}) - \frac{h_\infty d_3}{h d_2}(T_\mathrm{C} - T_\infty). \qquad (3.5)\end{aligned}$$

Using the thermally thin wall assumption, $T_\mathrm{R} - T_\mathrm{C} \gg T_\mathrm{W,R} - T_\mathrm{W,C}$, the first term on the RHS of Eqn. (3.4) simplifies to $2T_\mathrm{W}$, and the first term on the RHS of Eqn. (3.5) can be neglected. Therefore, Eqns. (3.4) and (3.5) are rewritten as:

$$\begin{aligned}\frac{\dot{m}_\mathrm{R} C_\mathrm{PR}}{\pi h d_1}\frac{\mathrm{d}T_\mathrm{R}}{\mathrm{d}x} \quad + \quad & \frac{\dot{m}_\mathrm{C} C_\mathrm{PC}}{\pi h d_2}\frac{\mathrm{d}T_\mathrm{C}}{\mathrm{d}x} = \\ & 2T_\mathrm{W} - (T_\mathrm{R} + T_\mathrm{C}) + \frac{h_\infty d_3}{h d_2}(T_\mathrm{C} - T_\infty), \qquad (3.6) \\ \frac{\dot{m}_\mathrm{R} C_\mathrm{PR}}{\pi h d_1}\frac{\mathrm{d}T_\mathrm{R}}{\mathrm{d}x} \quad - \quad & \frac{\dot{m}_\mathrm{C} C_\mathrm{PC}}{\pi h d_2}\frac{\mathrm{d}T_\mathrm{C}}{\mathrm{d}x} = \\ & -(T_\mathrm{R} - T_\mathrm{C}) - \frac{h_\infty d_3}{h d_2}(T_\mathrm{C} - T_\infty). \qquad (3.7)\end{aligned}$$

Adding and subtracting Eqns. (3.6) and (3.7) yield a form similar to the original equations. The final set of equations is then reduced to:

$$\begin{aligned}\frac{k_\mathrm{W}}{4h}(d_2^2 - d_1^2)\frac{\mathrm{d}^2 T_\mathrm{W}}{\mathrm{d}x^2} &= -d_1(T_\mathrm{R} - T_\mathrm{W}) + d_2(T_\mathrm{W} - T_\mathrm{C}), \qquad (3.8) \\ \frac{\dot{m}_\mathrm{R} C_\mathrm{PR}}{\pi h d_1}\frac{\mathrm{d}T_\mathrm{R}}{\mathrm{d}x} &= -(T_\mathrm{R} - T_\mathrm{W}), \qquad (3.9) \\ \frac{\dot{m}_\mathrm{C} C_\mathrm{PC}}{\pi h d_2}\frac{\mathrm{d}T_\mathrm{C}}{\mathrm{d}x} &= -(T_\mathrm{W} - T_\mathrm{C}) + \frac{h_\infty d_3}{h d_2}(T_\mathrm{C} - T_\infty). \qquad (3.10)\end{aligned}$$

These equations are then numerically integrated to obtain the axial temperature variations in the reactant and control flows and the wall.

3.1.2 Reaction Model

The heat exchanger model from the previous section is extended to integrate a preferential oxidation (PrOx) model. The PrOx reactor is used in a fuel processor after the water gas shift reactor(WGS) to further reduce the amount of CO (below 5–10 ppm) for PEM fuel cell applications [46]. First the PrOx reaction mechanism is described, followed by the reduction of the mechanism to a simplified form and then application into the reaction model.

Pt/γ-Al_2O_3 catalyst is written as:

$$\mathrm{CO} + \frac{1}{2}\,\mathrm{O_2} \rightarrow \mathrm{CO_2} \qquad \Delta H = -280\ \mathrm{kJ/mol} \tag{3.11}$$

$$\mathrm{H_2} + \frac{1}{2}\,\mathrm{O_2} \rightarrow \mathrm{H_2O} \qquad \Delta H = -240\ \mathrm{kJ/mol} \tag{3.12}$$

$$\mathrm{CO} + \mathrm{H_2O} \rightarrow \mathrm{CO_2} + \mathrm{H_2} \qquad \Delta H = -41\ \mathrm{kJ/mol} \tag{3.13}$$

$$\mathrm{CO} + 3\,\mathrm{H_2} \rightarrow \mathrm{CH_4} + \mathrm{H_2O} \qquad \Delta H = -210\ \mathrm{kJ/mol} \tag{3.14}$$

Of the above equations, the water gas shift reaction (Eqn. 3.13) and the methanation reaction (Eqn. 3.14) occur in trace quantities and are neglected. The remaining two reactions are reduced to a single unified reaction by employing CO Selectivity (S), which is defined as:

$$\text{CO Selectivity} = \frac{[\text{moles of } \mathrm{O_2} \text{ consumed for CO oxidation}]}{[\text{total moles of } \mathrm{O_2} \text{ consumed}]} \tag{3.15}$$

Experiments have shown [46] the CO selectivity to be nearly a constant over the temperature range of 140–210°C in which the PrOx reactor operates. With this simplification, the overall mechanism is reduced to:

$$\mathrm{CO} + \frac{1-S}{S}\,\mathrm{H_2} + \frac{1}{2S}\,\mathrm{O_2} \rightarrow \mathrm{CO_2} + \frac{1-S}{S}\,\mathrm{H_2 0}. \tag{3.16}$$

Simplifying a standard species transport equation, the steady state distribution of the CO concentration is given as:

$$\frac{d(C_{\mathrm{CO}}v)}{dx} = \dot{\Omega}_{\mathrm{CO}}. \tag{3.17}$$

The molar reaction rate for the CO oxidation is adopted from Kim *et.al.*[47] as:

$$\dot{\Omega}_{\mathrm{CO}} = r_{\mathrm{CO|TOF}} \times \left(\frac{W_{TOT}}{LA_C}\right) \times \frac{\theta \cdot \chi}{M_{\mathrm{Pt}}}, \tag{3.18}$$

where the turn over frequency (TOF) is given by:

$$-r_{\mathrm{CO|TOF}} = k_{\mathrm{CO}} \cdot e^{\frac{-Ea}{RT}} \cdot p_{\mathrm{CO}}^{\alpha} \cdot p_{\mathrm{O_2}}^{\beta}. \tag{3.19}$$

The flow controllers are calibrated at room temperature T_0. Hence, the reactant flow speed v needs to be corrected with the local temperature in the reaction channel, T_R. Equation (3.17) is then combined with Eqn. (3.18) to give:

$$\frac{\mathrm{d}(C_{\mathrm{CO}}T_{\mathrm{R}})}{\mathrm{d}x} = r_{\mathrm{CO|TOF}}\frac{T_0}{V_0}\frac{W_{TOT}}{L}\frac{\theta \cdot \chi}{M_{\mathrm{Pt}}}. \tag{3.20}$$

A similar conservation equation can also be derived for the oxygen species by relating the stoichiometry in the overall reaction (Eqn. 3.16):

$$\frac{\mathrm{d}(C_{\mathrm{O_2}}T_{\mathrm{R}})}{\mathrm{d}x} = \frac{1}{2S}\frac{\mathrm{d}(C_{\mathrm{CO}}T_{\mathrm{R}})}{\mathrm{d}x}. \tag{3.21}$$

The heat released by the PrOx reactions leads to an addition of a heat generation term to the reaction channel equation (Eqn. 3.9).

3.1.3 Complete model

Combining the heat transfer and reaction model equations, the system of equations is then written as:

$$\begin{aligned}
\frac{\mathrm{d}^2 T_{\mathrm{W}}}{\mathrm{d}x^2} &= [-d_1(T_{\mathrm{R}} - T_{\mathrm{W}}) + d_2(T_{\mathrm{W}} - T_{\mathrm{C}})]\frac{4h}{k_{\mathrm{W}}(d_2^2 - d_1^2)}, \\
\frac{\mathrm{d}T_{\mathrm{R}}}{\mathrm{d}x} &= -(T_{\mathrm{R}} - T_{\mathrm{W}})\frac{\pi h d_1}{\dot{m}_{\mathrm{R}} C_{\mathrm{PR}}} + \frac{\mathrm{d}(C_{\mathrm{CO}} T_{\mathrm{R}})}{\mathrm{d}x}\frac{\Delta H_R^0}{\pi h d_1}\frac{V_0}{T_0}, \\
\frac{\mathrm{d}T_{\mathrm{C}}}{\mathrm{d}x} &= -(T_{\mathrm{W}} - T_{\mathrm{C}})\frac{\pi h d_2}{\dot{m}_{\mathrm{C}} C_{\mathrm{PC}}} + \frac{\pi h_{\infty} d_3}{\dot{m}_{\mathrm{C}} C_{\mathrm{PC}}}(T_{\mathrm{C}} - T_{\infty}), \\
\frac{\mathrm{d}(C_{\mathrm{CO}} T_{\mathrm{R}})}{\mathrm{d}x} &= r_{\mathrm{CO|TOF}}\frac{T_0}{V_0}\frac{W_{TOT}}{L}\frac{\theta \cdot \chi}{M_{\mathrm{Pt}}}, \\
\frac{\mathrm{d}(C_{\mathrm{O_2}} T_{\mathrm{R}})}{\mathrm{d}x} &= \frac{1}{2S}\frac{\mathrm{d}(C_{\mathrm{CO}} T_{\mathrm{R}})}{\mathrm{d}x}.
\end{aligned} \tag{3.22}$$

The boundary conditions for above system of equations are given as:

$$\begin{aligned}
x = 0 \quad & \begin{cases} T_{\mathrm{W}} &= (d_1 T_{\mathrm{R}}^0 + d_2 T_{\mathrm{C}}^0)/(d_1 + d_2) \\ T_{\mathrm{R}} &= T_{\mathrm{R}}^0 \\ C_{\mathrm{CO}} T_{\mathrm{R}} &= [C_{\mathrm{CO}} T_{\mathrm{R}}]^0 \\ C_{\mathrm{O_2}} T_{\mathrm{R}} &= [C_{\mathrm{O_2}} T_{\mathrm{R}}]^0 \end{cases} \\
x = L \quad & \begin{cases} T_{\mathrm{W}} &= (d_1 T_{\mathrm{R}}^{\mathrm{L}} + d_2 T_{\mathrm{C}}^{\mathrm{L}})/(d_1 + d_2) \\ T_{\mathrm{C}} &= T_{\mathrm{C}}^{\mathrm{L}} \end{cases}
\end{aligned} \tag{3.23}$$

The above system of equations constitutes a coupled boundary value problem[48]. The Matlab [49] boundary value solver `bvp4c` is used to solve the system. The solver uses the Lobatto IIIA collocation formula to obtain the solution.

Prior to performing extensive parametric studies, the accuracy of the kinetic reaction model was validated by comparing the calculation results with experimental data by Srinivas *et al.*[46] for an isothermal reactor. The agreement was found to be acceptable as shown in figures 5.7 and 5.8.

3.2 Model performance metrics

Employing the model described above, three quantities are primarily examined as performance metrics. First, the most important metric is the net conversion of CO that the system can achieve. For maximum conversion, since the kinetics are Arrhenius, the temperature should be kept as high as possible throughout the reactor. However, maintaining the temperature requires an external heat source and is found to be inefficient.

Instead of keeping the temperature constant, it can be allowed to decrease over the length of the reactor. This loss in the overall enthalpy in the reaction channel can then be recuperated into the outer control stream, which in turn loses heat to the ambient. Therefore, the outer channel serves as a buffer stage that can recycle a significant fraction of heat. As a second performance metric, the overall efficiency is thus defined as the ratio of the net heat gained by the control channel to the total heat received from the reaction channel. In other words, it is the measure of the heat recuperation from the reaction channel. Finally, the reactive length is defined as the ratio of the length of the reaction channel where up to 95% of the total CO conversion takes place. This metric tries to quantize the part of reactor used for CO conversion. For *e.g.*, if 95% of the reaction occurs in the first half of the reactor, the rest of the reactor is not contributing significantly to the reaction, but mainly acts as a heat exchanger(as shown in Figure 3.3). The reactive length parameter is normalized with respect to the total length of the reaction channel.

3.3 Parameter list and selection

To identify optimal operating conditions and obtain the reaction characteristics within the channel, a variety of design parameters are considered. These include geometry (length, wall thickness, construction material), the mass flow rates, and the inlet temperatures among others. The full list of parameters considered are shown in figure 3.2. The parameters which then selected for further study are highlighted in blue.

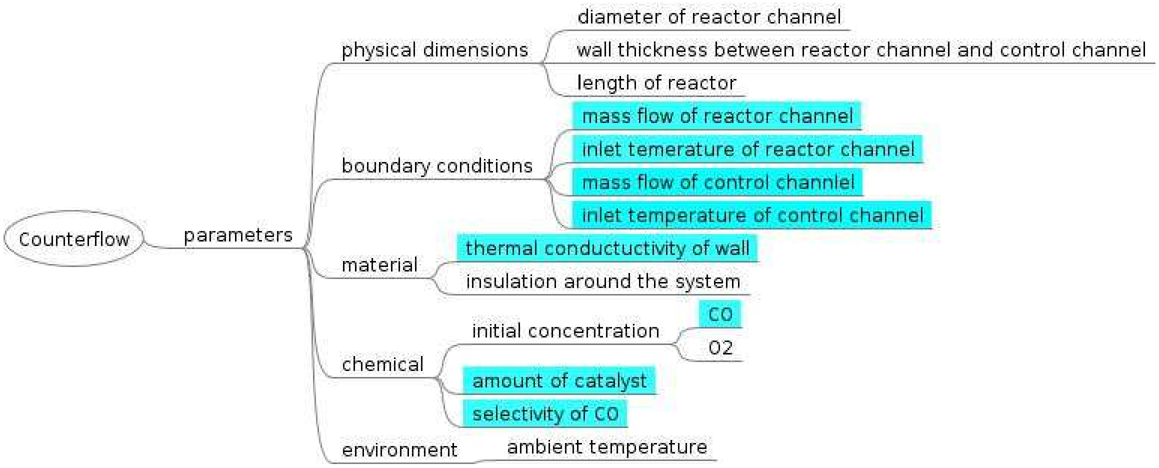

Figure 3.2: Counterflow model parameter tree. The selected parameters are marked in blue and listed in Table 3.1

Some of these parameters are rather fixed by the specific design targets and constraints. For example, the reactant mass flow rate is determined by the desired output of the system, and the geometry and dimension are often limited by the size limitation. In this study, the inlet for the PrOx reaction channel is set with a mixture of 60% H_2,1% CO, 1% O_2 in Argon, with the flow rate at 0.0186 gm/sec. This flow rate of hydrogen is expected to produce approximately 40 W of power in a 100%-efficient fuel cell stack. The amount of catalyst is determined by fixing the weight hourly space velocity (WHSV) to be approximately 120,000. The control stream is taken to be water. The flow rate of 0.005 gm/sec for the control stream is the net water requirement for an iso-octane fuel reforming system for the numbers given above. Based on these operating conditions, we explore the selected parameters and examine their effects on the three performance metrics discussed above. The base high and low values for the selected parameters are given in table 3.1.

3.4 Model results

Figure 3.3 shows a typical behavior of the temperature and reaction rate profiles within the PrOx reactor model. The entry part of the reactor is highly reactive due the high temper-

Parameter	Symbol	Low Value	Baseline	High Value	Units
Reactor channel mass flow rate	$\dot{m}_{\mathrm{R}}$	0.009	0.0186	0.036	gm/sec
Reactor channel inlet temperature	T_{R}^{0}	468	471	473	K
Control channel mass flow rate	$\dot{m}_{\mathrm{C}}$	0.0026	0.005	0.015	gm/sec
Control channel inlet temperature	$T_{\mathrm{C}}^{\mathrm{L}}$	300	300	330	K
Thermal conductivity	k_{w}	2	12	127	W/m-K
Initial CO mole fraction	X_{CO}	0.01	0.01	0.05	-
Mass of catalyst	W_{TOT}	0.4	0.8059	0.88	gm
Selectivity	S	0.45	0.5	0.55	-

Table 3.1: Parameter values for PrOx Counterflow model

atures, after which the reaction channel temperature drops and the reaction rate decreases exponentially. The latter part of the reactor thus functions primarily as a heat exchanger. For the entry region, since the temperature is high, the reaction rate is fast which gives a high heat release rate. This in turn raises the temperature and maintains a high reaction rate. Once the temperature drops further downstream, the reaction rate and the heat release rate decreases with the depletion of the reactants which accelerates the temperature drop. In a fuel processing system, where each subsequent reactor has a lower temperature, the latter heat exchanger part of the reactor can thus be designed so as to provide the inlet temperature of the next reactor. Despite the lower temperature, the latter part of the reaction channel can be beneficial for reactions with a favorable equilibrium at lower temperatures[50].

3.4.1 Parametric results

Figure 3.4 shows the effect of the mass flow rate in the reaction channel($\dot{m}_{\mathrm{R}}$) on the CO conversion, reactive length and efficiency. As mass flow in the reaction channel in increased, the reaction channel is able to hold the higher temperature much better. However the coolant channel does not correspondingly increase its temperatures. Even though heat transferred to the control channel increase with the reaction channel mass flow rate, the increase in heat recuperation is comparatively lower. This makes the efficiency drop quite substantially as the mass flow rate in the reaction channel is increased.

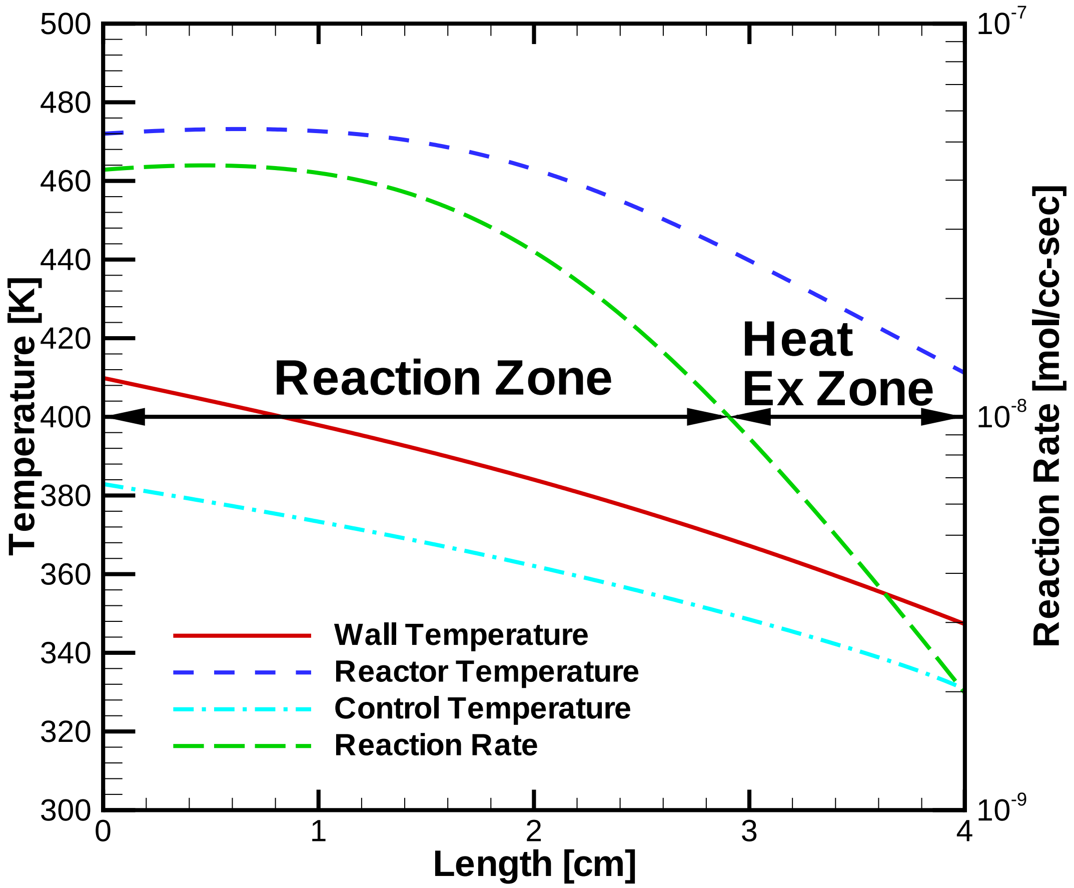

Figure 3.3: Temperature and reaction rate profiles for the counterflow model

For the reactive length, since the temperature in the reaction channel stays higher for longer of the length in the reaction channel, more of the reaction channel accounts for the net reaction. Hence the reactive length increases. Interestingly, conversion is flat. Even though the temperature are higher and the reactive length increases giving higher reaction rates, the flux of incoming CO also increases. This causes the conversion of stay fairly flat as the mass flow rate in the reaction channel is varied.

Figure 3.5 shows the effect of the reaction channel inlet temperature(T_{R}^{0}) on the CO conversion, reactive length and efficiency. The results due the reaction inlet temperature are similar to the previous reaction channel inlet mass flow rate except that the flow rate had

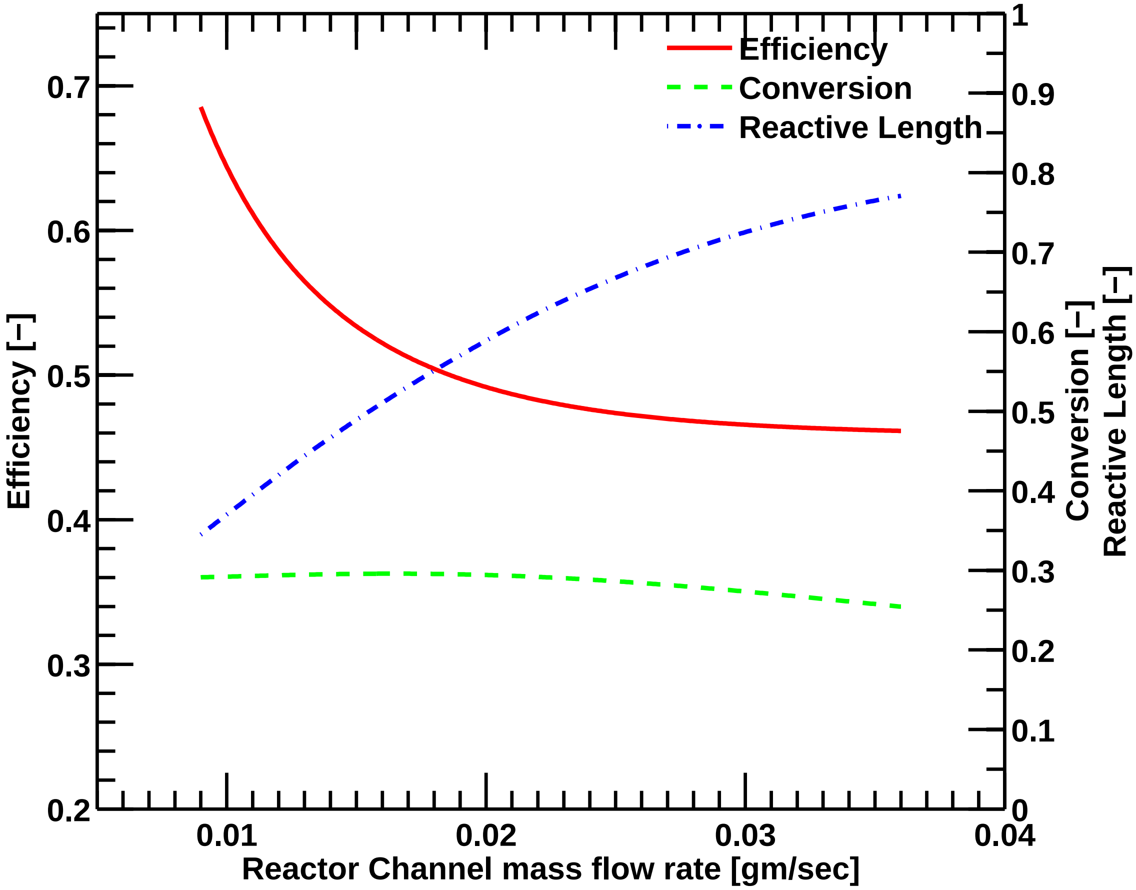

Figure 3.4: Efficiency, CO conversion and reactive length versus reaction channel flow rate

diminishing effect as the rate went up, while the inlet temperature has an increasing effect as the rate goes up.

The inlet temperature directly effects the enthalpy going into the system. It does increase the temperature of the reaction channel considerably. Hence the conversion increases noticeably since this time the incoming flux of CO remains the same. The reactive length has similar characteristics due to the increased temperature and it increases as well.

For efficiency, both the heat transferred and heat recuperated increase, however the recuperation does not increase as much as the heat transferred. Therefore, the efficiency decreases as the reaction channel inlet temperature increases similar as before.

From a control standpoint, changing the reactor channel inlet temperature beyond a limit not be desirable since certain unwanted reactions might becomes prominent at higher

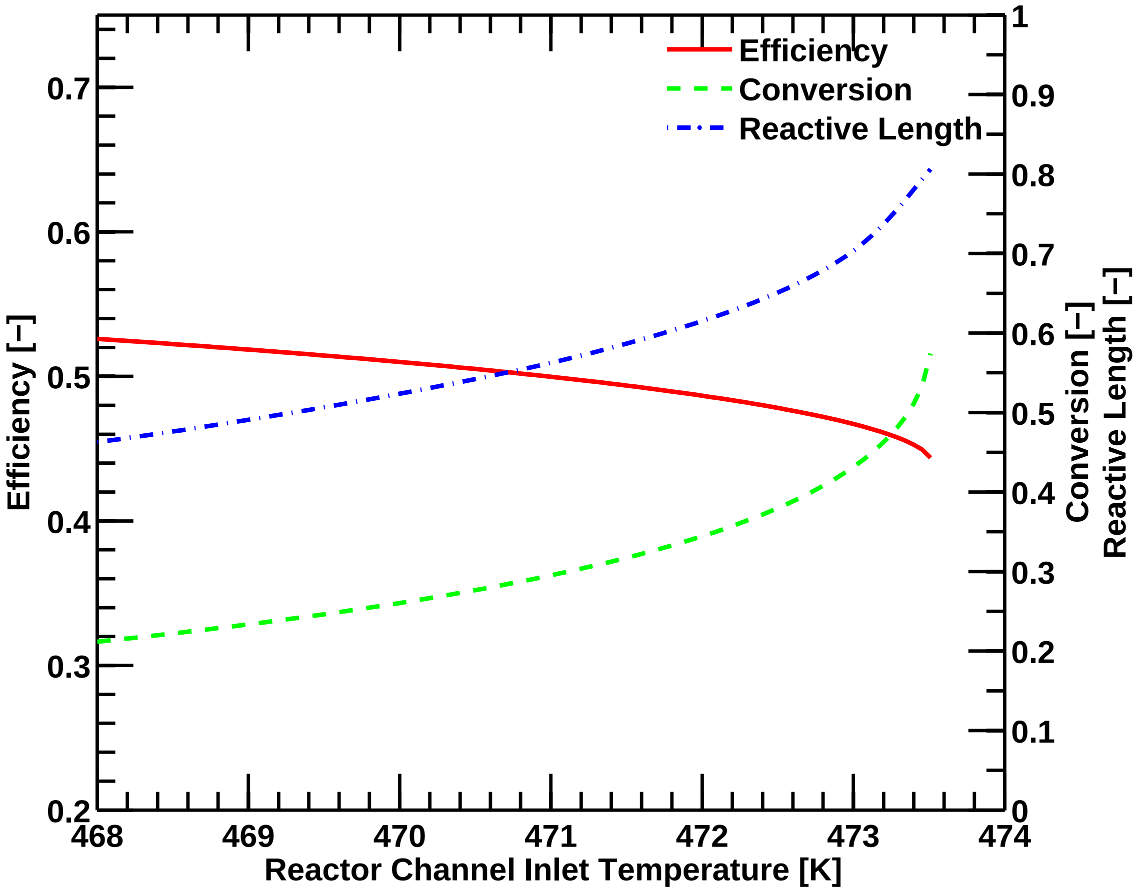

Figure 3.5: Efficiency, CO conversion and reactive length versus reaction channel inlet temperature

temperatures. An example is the formation of methane at higher temperatures in the PrOx setup.

Figure 3.6 shows the effect of the control flow rate($\dot{m}_C$) on the CO conversion, reactive length and efficiency of the system. Increasing the control flow rate does increase the efficiency as it retains more heat, but this comes at a drastic expense of lower conversion rates. A higher flow rate increases the effective heat capacity of the control flow, thus the temperature rise is reduced and it draws more heat from the reaction channel. This results in a reduced temperature in the reaction channel and hence a lower conversion rate. By the same reasoning, a reduced control mass flow rate results in a higher CO conversion at a lower efficiency. Therefore, it is clear that there is a trade-off between the CO conversion

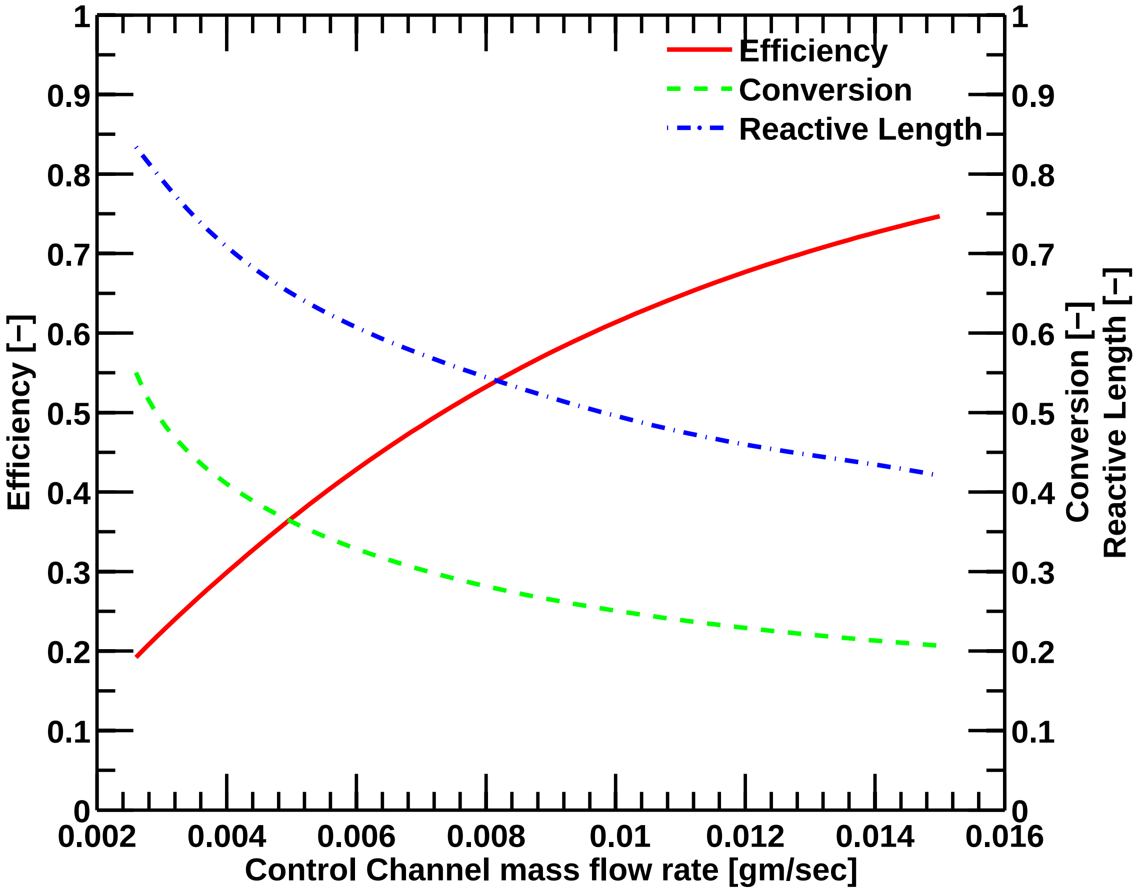

Figure 3.6: Efficiency, CO conversion and reactive length versus control flow rate

and the efficiency (or the heat recuperation) as the control mass flow rate is varied. At higher flow rates, all the curves tend to level off to an asymptotic value. The flow rate is thus effective within a certain range of low flow values.

Figure 3.7 shows the normalized sensitivity coefficients of the three performance metrics to the control flow rate. Consistent with the results in Fig. 3.6, it is clearly seen that the performance of the reactor is more sensitive at lower control flow rates. The results clearly suggest that the control mass flow rate can be a convenient means to adjust the reactor operation at desired conditions. An excessively high rate of control mass flow may lead to a total turn-down of the system, in which case an external heating unit may be required to maintain the system operation. For similar reasons, an external source of heating may be

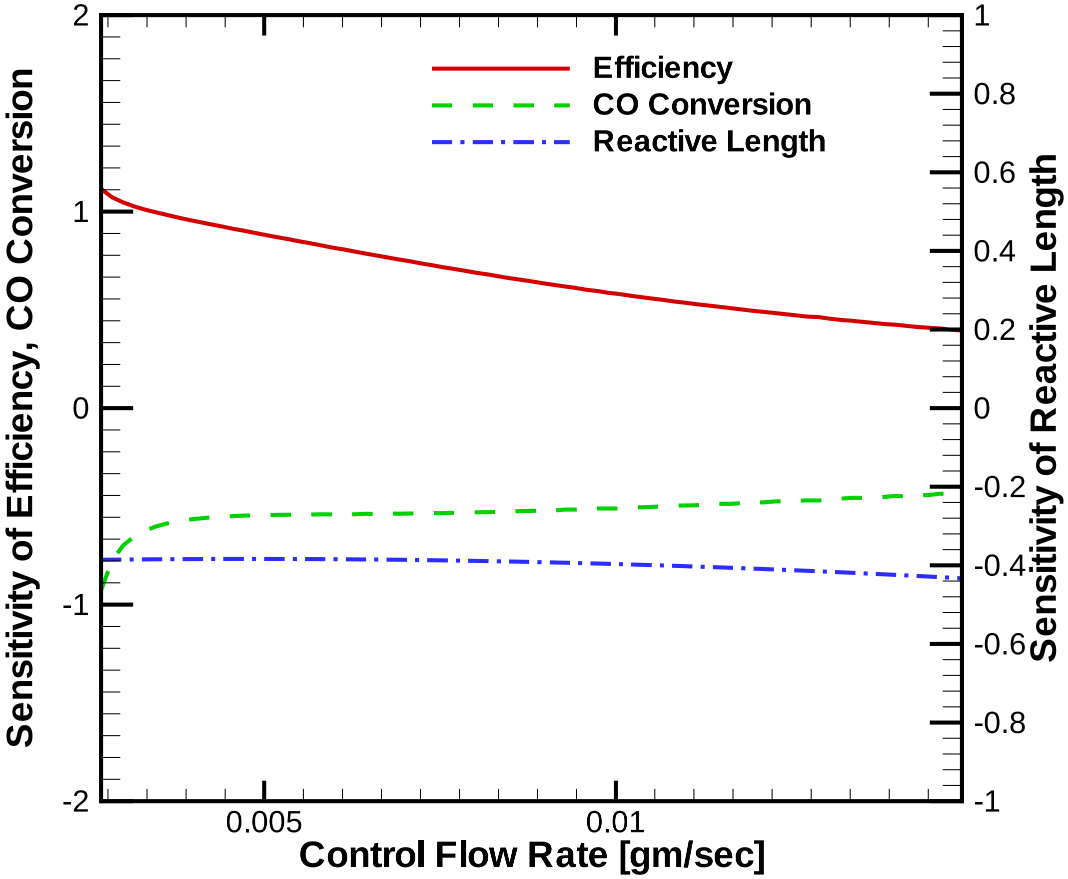

Figure 3.7: Normalized sensitivity of efficiency, CO conversion and reactive length versus control flow rate

needed during start-up until the catalyst becomes activated.

Figure 3.8 shows the effect of control inlet temperature(T_C^L) on the same performance metrics. The overall effect is similar to that of the control flow rate in that a higher inlet temperature of the control flow promotes reaction, thereby increasing the conversion and decreasing the efficiency. Compared to the control mass flow, the effect of the control inlet temperature leads to a wider range of variations in the performance metrics. This is because the control inlet temperature has a direct effect on the enthalpy of the system. Figure 3.9 shows the normalized sensitivity of the metrics to the control inlet temperature. It can be

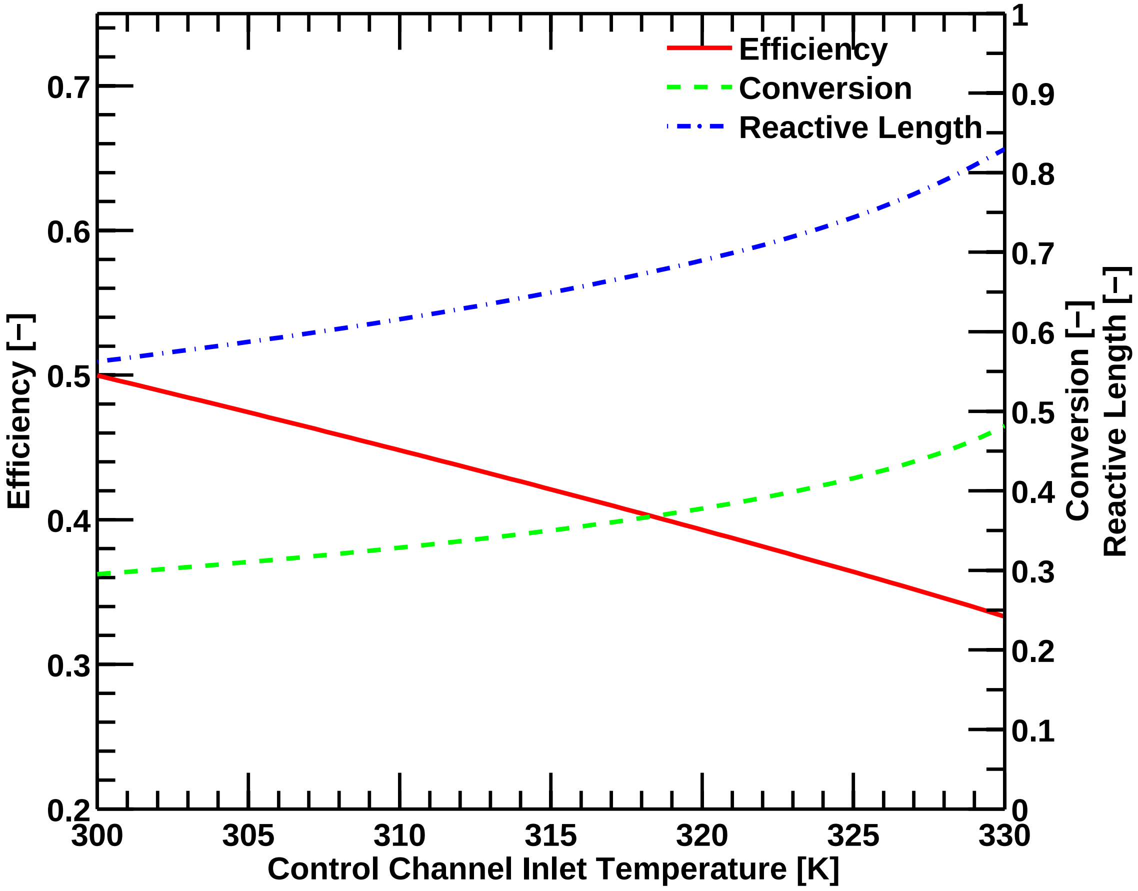

Figure 3.8: Efficiency, CO conversion and reactive length versus control flow inlet temperature

seen that the sensitivity of all three quantities is considerably higher than the sensitivity to the control flow rate. Therefore, it is concluded that the inlet temperature is a more effective means for the control of the system, while the control flow rate is suitable for smaller adjustments.

Figure 3.10 shows the effect of thermal conductivity of the construction material(k_W) on the CO conversion, reactive length and efficiency. The effect of conductivity is generally very small except at the low values where the material behaves more like an insulator. Anything above a value of 20–30 W/m-K, the system effectively washes out the temperature in the wall and it behaves like a very thin wall. In that scenario, the main heat resistances are the convective resistances between the fluids and the wall, *i.e.* between the fluid in the

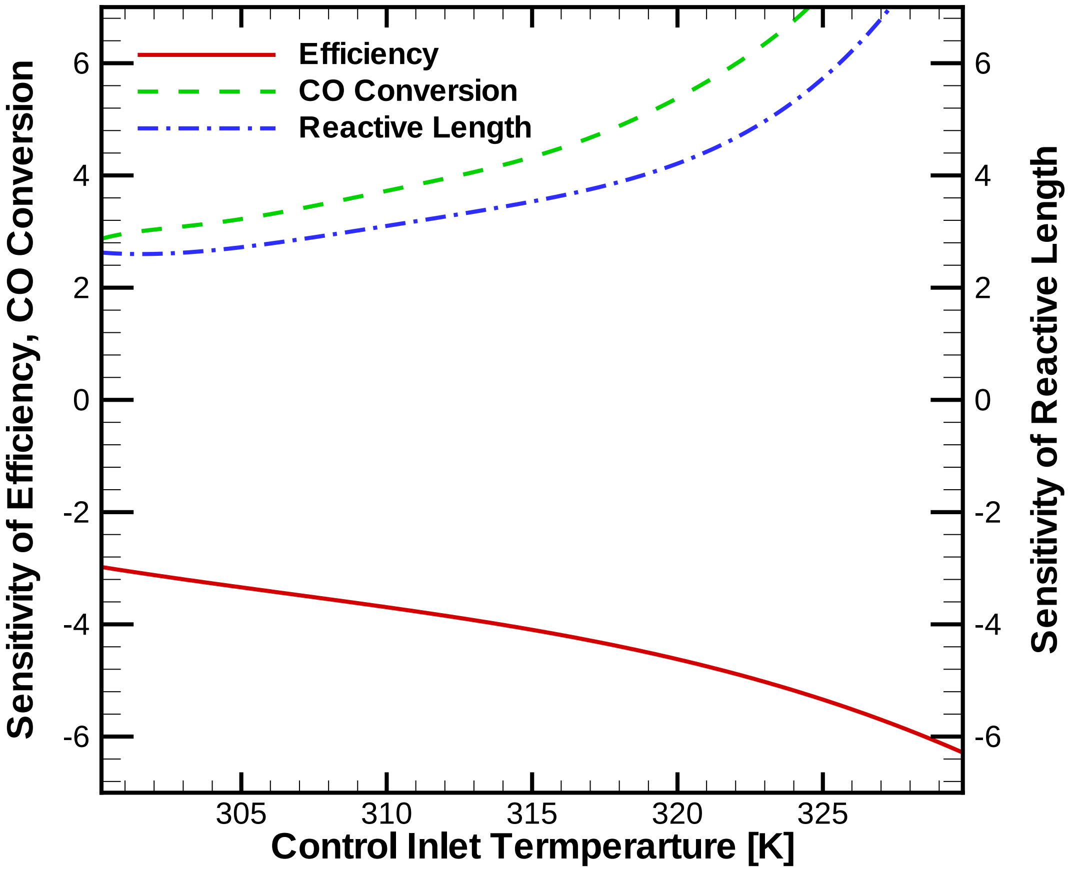

Figure 3.9: Normalized sensitivity of efficiency, CO conversion and reactive length versus control inlet temperature

reaction channel and the wall and between the wall and the control channel. The material then has minimal effect on the operation of the system.

At the low values of thermal conductivity the material behaves more like an insulator and provides substantial thermal resistance between the reaction and control channels. This may or may not be helpful since it also impedes the transfer of heat from the reaction channel to the control channel. A low resistance is better for heat recuperation while at the same time it might lower the temperature of the reaction channel more than what is required. Hence the material is an important design factor that can be used to set the

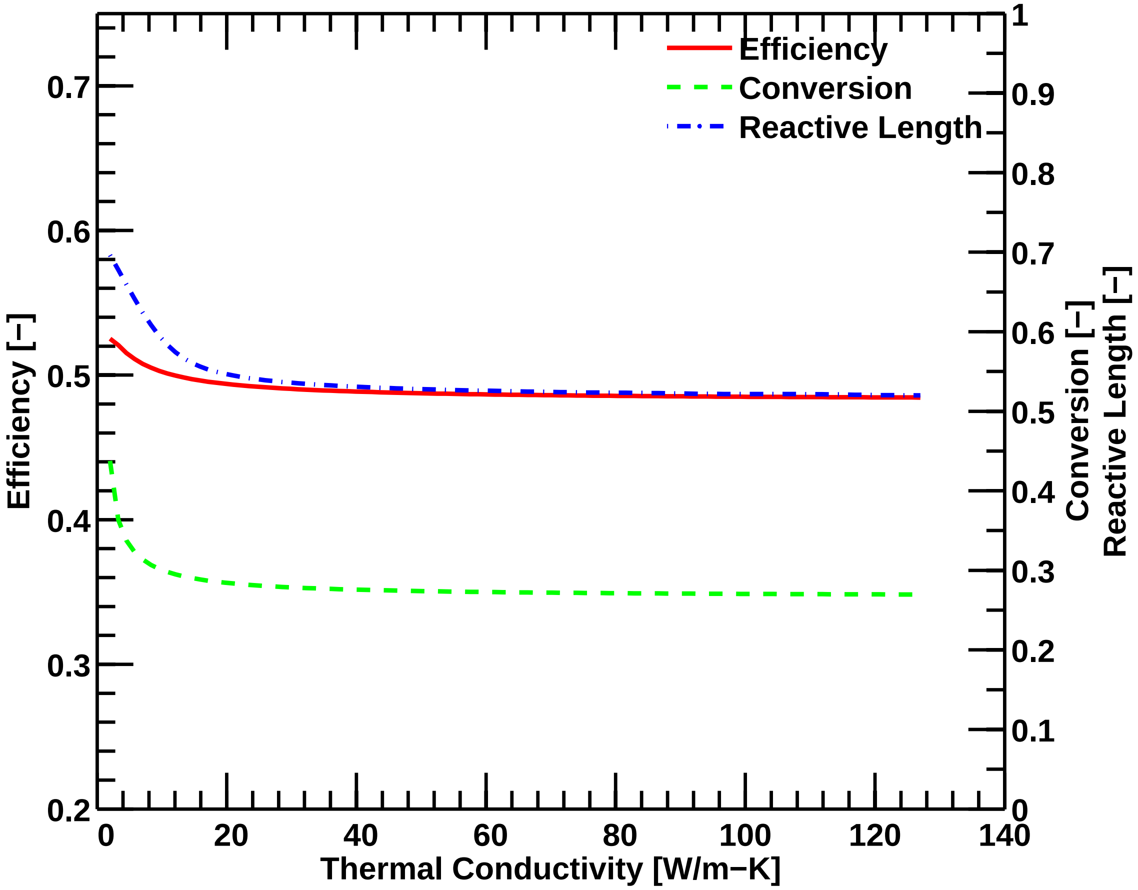

Figure 3.10: Efficiency, CO conversion and reactive length versus wall thermal conductivity

operating point of the system.

A thing to note is that in Section 3.1.1, the assumption was made that the wall is thermally thin and hence the model is not valid at these low values of thermal conductivity.

Figure 3.11 shows the effect of mole fraction of CO in the inlet stream(X_{CO}) on the CO conversion, reactive length and efficiency. The mole fraction of CO in the system is a very interesting parameter. As CO mole fraction is increased, the corresponding Argon mole fraction is decreased to ensure that the effect of the amount of CO is isolated from the other species in the system.

As the CO mole fraction increases, the raw amount of CO the system has to remove also increases. Even though reaction rates slightly increase due to higher CO concentration, the

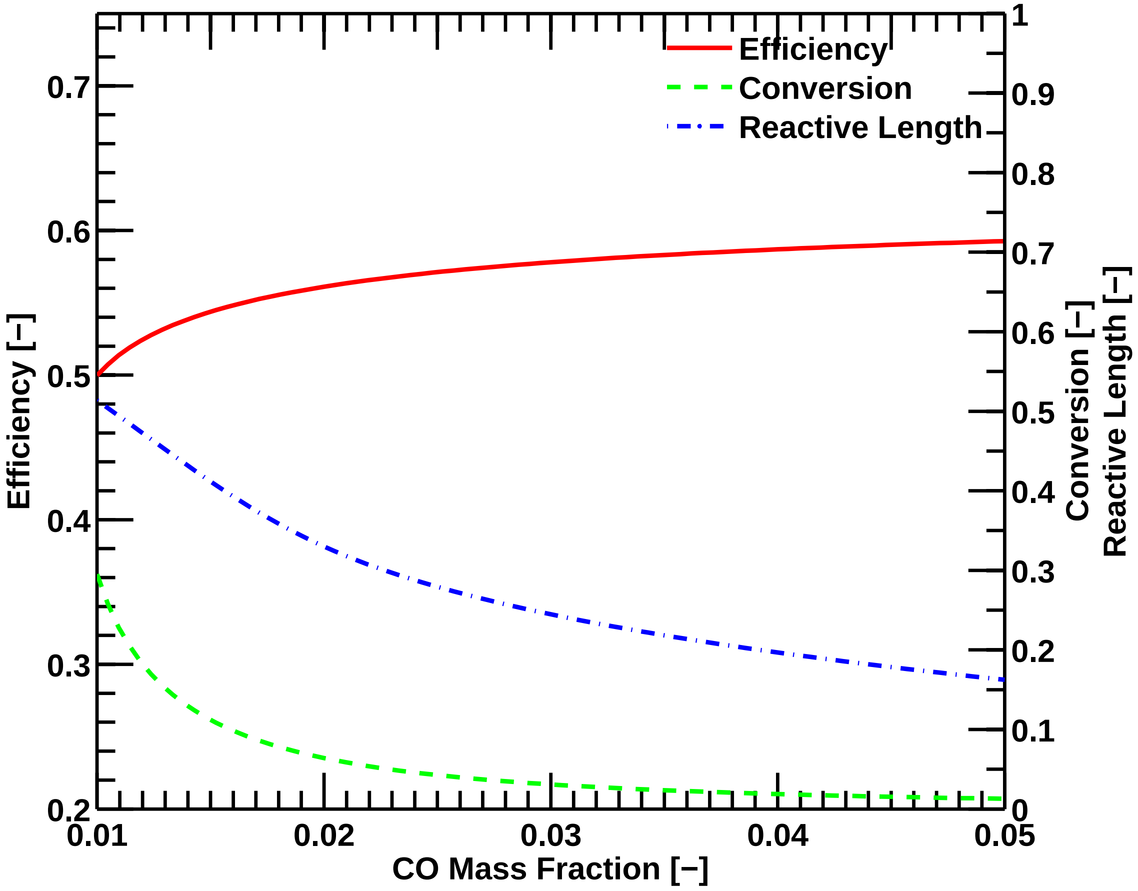

Figure 3.11: Efficiency, CO conversion and reactive length versus CO mass fraction in the inlet stream

oxygen(and other species) levels remain the same limiting the reaction rate. Further the of oxygen available to drive the CO oxidation reaction is also the same as before while the amount of CO has increased. Hence the conversion of CO falls as the inlet CO concentration increases.

Keeping the above paragraph in mind, as the conversion drops off as the CO inlet mole fraction is increased, the reaction rates also drops off sharply similarly and hence the reactive length decreases also as the CO inlet mole fraction is increased.

Figure 3.12 shows the effect of mass of catalyst(W_{TOT}) in the reaction channel on the CO conversion, reactive length and efficiency. Mass of catalyst has a direct effect on the reaction rate. The more amount of catalyst in the system, the faster the reaction and

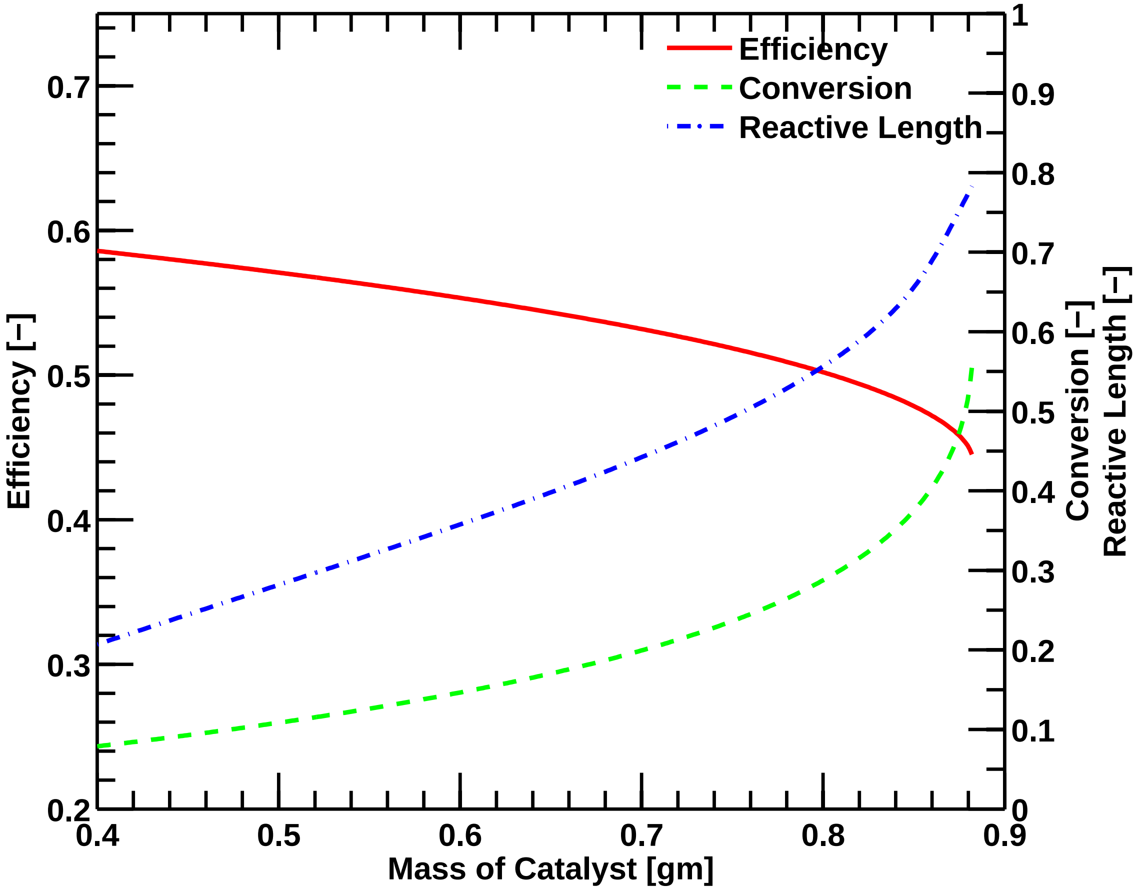

Figure 3.12: Efficiency, CO conversion and reactive length versus mass of catalyst

better CO conversion is obtained. Thus with increasing the mass of catalyst in the reaction channel, the conversion and reactive length both increase.

The heat generated and transferred from the reaction channel also increases as mass of the catalyst is increased. However the control channel finds it tough to hold onto the transferred heat and looses most of it to the ambient. Hence the Efficiency dips sharply as the amount of catalyst is increased.

Figure 3.13 shows the effect of selectivity (S) on the CO conversion, reactive length and efficiency. The parameter of selectivity is a very sensitive one. The reason is that how selectivity is defined and how the parametric study is undertaken. Selectivity is defined as the rate of oxygen used to oxidize CO to the total oxygen used. (which also includes oxygen used to oxidize hydrogen).

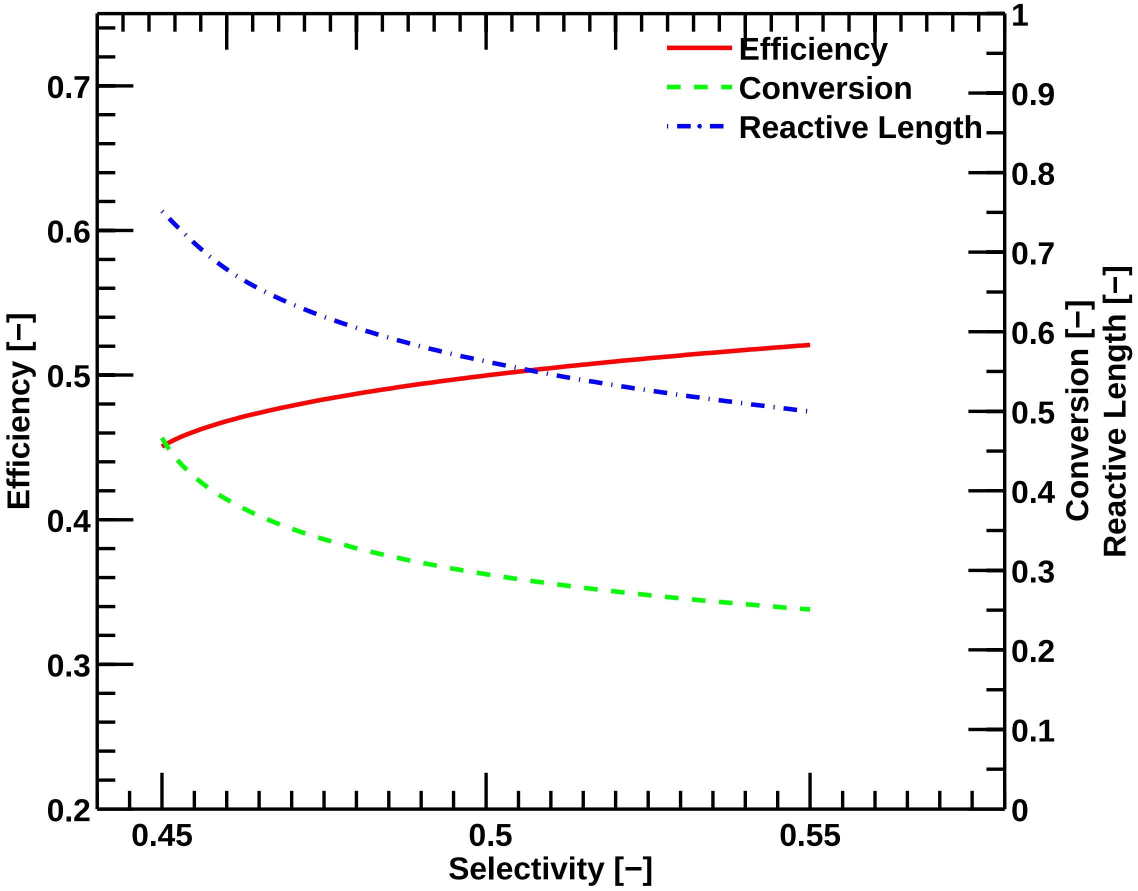

Figure 3.13: Efficiency, CO conversion and reactive length versus selectivity(S)

For the parametric study, the CO oxidation rate is calculated by the Arrhenius rate. Then based on the value of selectivity chosen, the hydrogen oxidation rate is determined. This when we vary the selectivity value, what we are changing is the rate of hydrogen oxidation. As selectivity is decreased, the hydrogen oxidation rate actually increases. The rate of CO oxidation meanwhile changes based on the temperature and the amount of CO and oxygen available and not on the selectivity value chosen.

Keeping in mind the heat of reaction for hydrogen oxidation is greater then that of CO oxidation, as we decreased selectivity the hydrogen oxidation increases, causing the heat to be released in the system to increase. This causes a higher temperature in the reaction channel and bumps up the CO oxidation rate which further increases the hydrogen oxidation rate and so on. Thus we a get a better conversion rate and reactive length. The efficiency as usual moves in the opposite direction and decreases as selectivity is decreased.

This work is performed with a PrOx reactive system which is mildly exothermic. Other systems that are more exothermic will generate a larger amount of heat that can be recuperated with a smaller expense of conversion efficiency. Note also that the present study employed free convective heat loss on the outer surface of the control channel without any insulation. Further improvement in the system performance is thus expected with an additional insulation on the outer surface which will reduce heat loss to the ambient.

3.5 Control stream for thermal management

The parametric work was done to look at the effect of various parameters to study their effect on the operation of the system. One of the main challenges with running a counter flow reaction system is control of the system. Too hot and you get unwanted reactions, too cold and the reaction ceases. Most of the parameters looked at are fixed once the design of the system is finalized or are very difficult to change once the system is running.

However two parameters that are easier to manipulate are the control stream mass flow rate($\dot{m}_{\mathrm{C}}$) and the control stream inlet temperature($T_{\mathrm{C}}^{\mathrm{L}}$). These effectively are inputs to a running system and can be changed as needed. As shown by the parametric studies, the control stream inlet temperature has a bigger effect and the flow rate a smaller but a significant effect on the operation of the system. Hence the control stream flow rate and temperature can be used as the primary controls when the system is running. The control channel inlet temperature could then be utilized as a coarse control while the flow rate as a fine control.

3.6 Expansion to multiple reactors

The current work is concentrated on the response of a single reactor. Based on the developed model, an integrated system of multiple reactors can be designed such that each

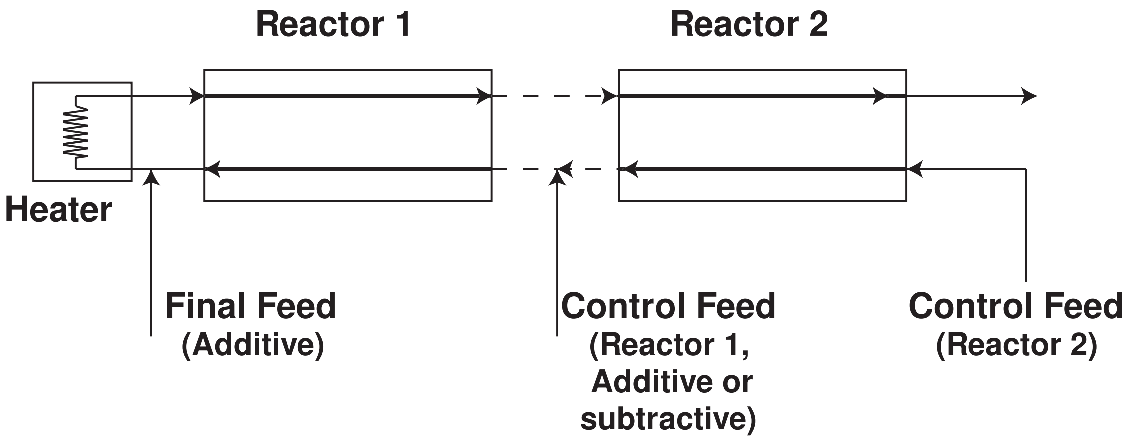

Figure 3.14: System Design for counterflow based reformer system

reactor unit is represented by an assembly of counterflow streams of reactants and control streams. The flow rates of the control stream and its temperature can be adjusted to control the individual reactors in the system. Figure 3.14 show one possible design based on such a concept. In this method, the feed is preheated as it flows as the control stream through reactors in the order of increasing temperature. This increases the control streams temperature stepwise through the reactors. Before every reactor, the control stream can be augmented or curtailed to suit the requirements of the subsequent reactor. The reactors themselves need not be discrete, and can be placed next to each other with no physical separation to avoid heat loss from the connecting pipes.

Taking the concept one step further, instead of packaging the reactors sequentially with all the reactors exposed to the same ambient temperature, the system can be designed into a layered structure wherein the hottest reactor is buried inside the structure. The other reactors are then layered on the outside to form a gradual temperature gradient from inside with the coolest reactor on the outside. This will reduce heat loss from the system because only the coolest reactor will loose heat to the ambient. This type of system design is expected to provide better performance and conversion efficiency. However control of such a design, especially the startup phase is not an easy task. It would demand some creative thinking like control of resident time of the flows and the associated heat transfer rates by using channels of varying cross-sectional area.

Chapter 4

Silicon Micro-reactor

4.1 Introduction

Micro-reactor technology is a relatively new concept which has offered the possibility of miniaturization of conventional macroscopic reactors while providing the same throughput[17]. By using the tools of micro-fabrication, several novel reactor configurations can be fabricated allowing different designs that would not have been possible with conventional packed beds. Such systems, referred to as micro-channel reactors or micro-reactors, typically have dimensions in the sub-millimeter range, the effect being a reduction in diffusive transport limitations. This translates into rapid heat and mass transfer rates and short response times[17, 25]. The walls of the micro-channels can be coated with catalytic material by a number of methods including sputtering, evaporation, slurry washcoating and solgel coatings. For a given catalyst loading, the pressure drop in wall-coated micro-channels is substantially lower than that in packed-bed reactors; the losses in wall-coated micro-channels would be primarily skin frictional losses, while in packed beds the form frictional losses around the packed particulates would be dominant in addition to skin friction[51, 52]. For example, considering the Ergun equation for a packed-bed and the equation for pressure drop in a wall- coated micro-channel of identical cross-section and catalyst loading, the pressure drop in the packed-bed is found to be approximately 400 times greater than that in the wall-coated channel. Note, however, that the wall-coated channel needs to be longer than the packed-bed to obtain the same catalyst loading, such that a careful system design and integration is necessary.

Figure 4.1: Silicon substrate based Preferential Oxidation(PrOx) micro-reactor

Micro-reactors also facilitate integration of different structural features (manifolds, static mixers, etc.) as well as functional elements (flow and temperature sensors, etc.). The scale-up is much simpler since it does not involve a conventional “pilot plant” based scale-up. Instead, the number of micro-reactors is increased and they are setup to operate in parallel to achieve the desired throughput[17]. Large scale packed-bed reactors incorporating powder or pellet type catalysts pose problems such as external diffusive limitations, large thermal gradients across the catalyst bed and flow distribution problems. These issues are much easier to handle in micro-reactors because of the flexibility in reactor engineering, their small size and ease of scale-up. Micro-reactor technology thus seems ideally suited for fuel processing reactor design as it provides quick starting, compact reactors capable of being taken on-board.

Recent efforts in the area of micro-reactor technology have shown promising results. An example would be micro-reactor fabricated in silicon substrate with integrated sensors and Platinum catalyst. The catalyst is deposited by an electron beam evaporation for ammonia oxidation, where conversionselectivity data and ignition-extinction behavior are explored[21]. A micro-fabricated differential packed-bed reactor is developed and demonstrated for CO oxidation and is successful in providing kinetic and mechanistic information, for use in catalyst screening[22]. However, scale-up issues of packed-bed reactors pose difficulties–the main one being high pressure drop. Membrane-based micro-reactors incorporating zeolites and palladium have also been fabricated and demonstrated[53, 54]. Pioneering efforts in developing micro-fabricated reaction systems are being carried out by various groups including Institut für Mikrotechnik Mainz (IMM)[19], Forschungszentrum Karlsruhe GmbH (FK)[20], Massachusetts Institute of Technology (MIT)[21, 22], The University of Michigan[23] and Pacific Northwest National Laboratory (PNNL)[24].

4.2 Micro-channel reactor fabrication

Micro-reactors are fabricated in silicon substrate using well known micro-fabrication techniques such as photo-lithography and deep reactive ion etching. Silicon is chosen as the substrate material because of its well-established processing techniques, excellent thermal properties, and suitability for catalyst coating. [31].

As an application to PrOx reactors, a silicon micro-channel reactor is originally designed by Srinivas and Gulari[31] as shown in Figure 4.2. The dimension of the silicon chip is 32.5 mm long, 32.5 mm wide, and $525\ \mu\mathrm{m}$ thick. To prepare the chip, a primary etch of $20\ \mu\mathrm{m}$ is made. The channels are then etched to a $250\ \mu\mathrm{m}$ depth. The channels have square $500\ \mu\mathrm{m}$ x $500\ \mu\mathrm{m}$ pillar shaped obstructions to facilitate mixing of the reformate stream. An 8 mm recess is left on both sides of the chip. The PrOx catalyst is then washcoated onto the chip.

The chips are designed such that multiple layers can be stacked to build a crossflow heat exchanger. Alternate chips can be made to carry different streams which interact only thermally. One set of chips would be aligned in one direction carrying one of the reformate streams while the other set would be aligned in the cross direction. This system

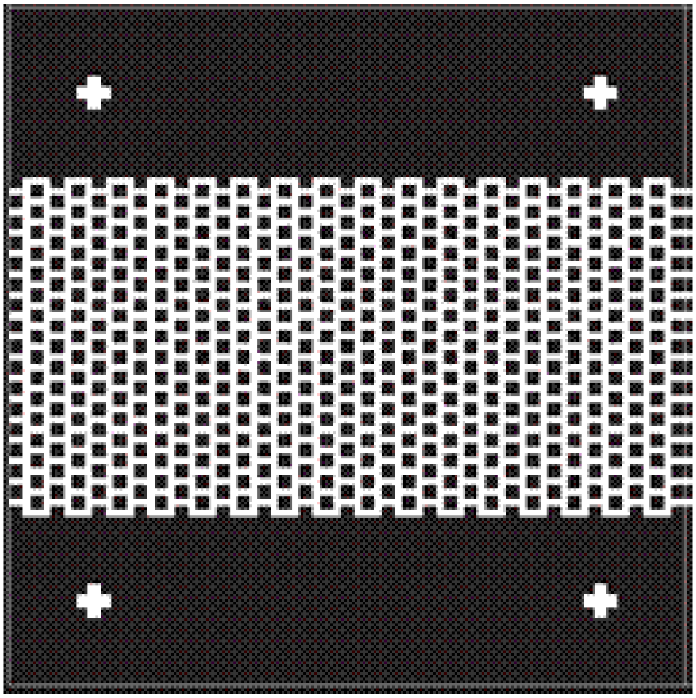

Figure 4.2: The original design of the silicon PrOx micro-reactor

can be applied to an endothermic reactor coupled with an exothermic reactor[55] for better thermal recuperation and efficiency.

4.3 Mass transfer analysis

The mass transfer analysis provides an estimation of the time of diffusion through the micro-reactor which would be used further as an input to the computational simulation of micro-reactor. Consider the diffusion of the gaseous reactants to the micro-reactor walls. The one-dimensional species conservation equation can then be written as

$$\frac{\mathrm{d}C}{\mathrm{d}t} = -D\frac{\mathrm{d}^2C}{\mathrm{d}x^2} \tag{4.1}$$

where C is the species concentration, D the gas diffusivity, and x the dimensional coordinate for diffusion[56]. Using this equation, we can obtain an order-of-magnitude estimate of the characteristic time needed for the gas to diffuse to the catalyst surface at the micro-reactor walls to be L^2/D, where L is the characteristic length for diffusion and D the gas diffusivity. Considering a representative value of the diffusion length $L = 400\ \mu\mathrm{m}$ in the micro-channel and $D = 0.1\ \mathrm{cm}^2/\mathrm{s}$ [57, 58], the characteristic diffusion time is estimated to be approximately 16 milliseconds. Under the operating conditions used, the typical residence time in the micro-reactor is approximately 1.8 seconds. Therefore, it is clear that the time for diffusion is much smaller than the residence time, such that external mass transfer effects should not play a significant role in the reaction.

4.4 Catalyst preparation

The catalyst preparation is done by Srinivas and Gulari[31] using the slurry-sol hybrid suspension method[59, 60]. An alumina sol is prepared with a particle size of $0.5\ \mu\mathrm{m}$, at an appropriate pH level to create a stable alumina suspension[61]. A solution of Dihydrogen hexachloroplatinate is added to the suspension in the appropriate amount to give a 2 wt.% Pt on Al_2O_3 loading. The walls of the micro-reactor are primed to form an adherent layer[27] and the catalyst suspension is then introduced into the silicon micro-reactor.

The coated micro-reactor is then dried for approximately 30 minutes at $100^\circ\mathrm{C}$ to form a porous washcoat layer on the walls. The coating and drying steps are repeated in order to build the catalyst washcoat layer until a desired catalyst loading of approximately 150 mg/cm^3 is obtained. Figure 4.3 shows SEM pictures of the washcoat layer on the silicon walls. The thickness of the washcoat is approximately 10 mm.

In another setup, the catalyst suspension is prepared in a similar manner, dried and calcined in a ceramic dish and then ground to 230 mesh size (62 mm) particles. This powder catalyst is used in a conventional tubular packed-bed reactor (4 mm ID and 8 mm bed height) for the purpose of comparing the results with those obtained using the wall-coated silicon micro-reactor.

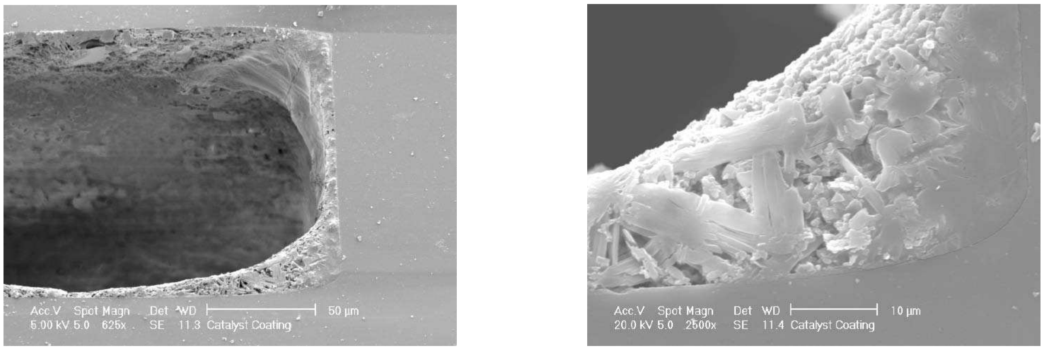

Figure 4.3: SEM images of the PrOx catalyst

4.5 The preferential oxidation reaction

In this study, PrOx is chosen as a model reaction and is carried out in a wall-coated micro-reactor fabricated in silicon chip, as well as in a conventional packed-bed reactor for the purpose of performance comparison. The test gas used consists of a 1:1 CO:O_2 mixture in a large excess of H_2 with argon as the carrier gas. The catalyst used is a 2% Pt on Al_2O_3 washcoat. The equations below give the reaction set for the PrOx reactions:

$$\mathrm{CO} + \frac{1}{2}\,\mathrm{O_2} \rightarrow \mathrm{CO_2} \qquad \Delta H = -280\ \mathrm{kJ/mol} \tag{4.2}$$

$$\mathrm{H_2} + \frac{1}{2}\,\mathrm{O_2} \rightarrow \mathrm{H_2O} \qquad \Delta H = -240\ \mathrm{kJ/mol} \tag{4.3}$$

$$\mathrm{CO} + \mathrm{H_2O} \rightarrow \mathrm{CO_2} + \mathrm{H_2} \qquad \Delta H = -41\ \mathrm{kJ/mol} \tag{4.4}$$

$$\mathrm{CO} + 3\,\mathrm{H_2} \rightarrow \mathrm{CH_4} + \mathrm{H_2O} \qquad \Delta H = -210\ \mathrm{kJ/mol} \tag{4.5}$$

In the above set of reactions, the oxidation reactions 4.2 and 4.3 are the primary reactions that take place in the PrOx reactor. The watergas shift equilibrium reaction 4.4 would occur to an extent governed by the amount of H_2O present in the system. The methanation reaction 4.5 typically occurs at very high temperatures. Reaction 4.2 and the forward reaction in 4.4 are desired as they consume CO. Reactions 4.3, 4.5 and the reverse reaction of 4.4 are undesired as they consume H_2. CO levels must be reduced to well below 100 ppm to avoid poisoning of the PEM fuel cell Platinum electrodes.

The following parameters are used to evaluate the performance of silicon micro-reactor and the packed-bed reactor:

$$\text{CO conversion} = \frac{\text{moles of CO consumed}}{\text{moles of CO fed}} \times 100 \tag{4.6}$$

$$\text{O}_2 \text{ conversion} = \frac{\text{moles of O}_2 \text{ consumed}}{\text{moles of O}_2 \text{ fed}} \times 100 \tag{4.7}$$

$$\text{PrOxselectivity} = \frac{\text{moles of O}_2 \text{ consumed for CO oxidation}}{\text{total moles of O}_2 \text{ consumed}} \times 100 \tag{4.8}$$

$$= \frac{1/2 \text{ moles of CO converted to CO}_2}{\text{total moles of O}_2 \text{ consumed}} \times 100 \tag{4.9}$$

4.6 CFD flow analysis

In addition to the thermal integration of the reactors using a simplified plug-flow model, 3D CFD is also used extensively to predict the flow and heat characteristics of the reactors. These efforts provided valuable guidance to the details in the design of the components. Throughout the fuel processor project, several components and assembly designs have directly benefited from the CFD modeling predictions. These will be described in this chapter.

A computational fluid dynamics (CFD) simulation to obtain the flow pattern for a gas (argon) in the micro-reactor is performed using FLUENT[62]. The Reynolds number under the range of operating conditions is calculated to be between 5 and 10. Therefore, the flow within the channels of the reactor is laminar in nature. Due to the symmetric nature of the micro-reactor design, the flow is modeled for a single inlet of the manifold with periodic boundary conditions. Pressure at the outlet is assumed to be atmospheric. The flow pattern near the inlet is seen to spread out rapidly, giving a mixing length within 2% of the total reactor length. Therefore, the flow is considered well mixed throughout the micro-reactor.

Modeling the entire chip in a 3D simulation is still a very difficult task. This would require an untenable number of grid points and also very long time to calculate. However, due to the repetitive pattern of channels on the chip, only a part of the chip can be simulated by employing periodic boundary conditions. To further simplify the simulations without causing any significant loss of accuracy, the $20\ \mu\mathrm{m}$ precut in the silicon substrate is ignored. Figure 4.4 shows the computational grids representing a segment of the micro-channel reactor. To resolve the fine-scale behavior near the boundary layer, the grid patterns have finer mesh near the solid surfaces in the streamwise direction.

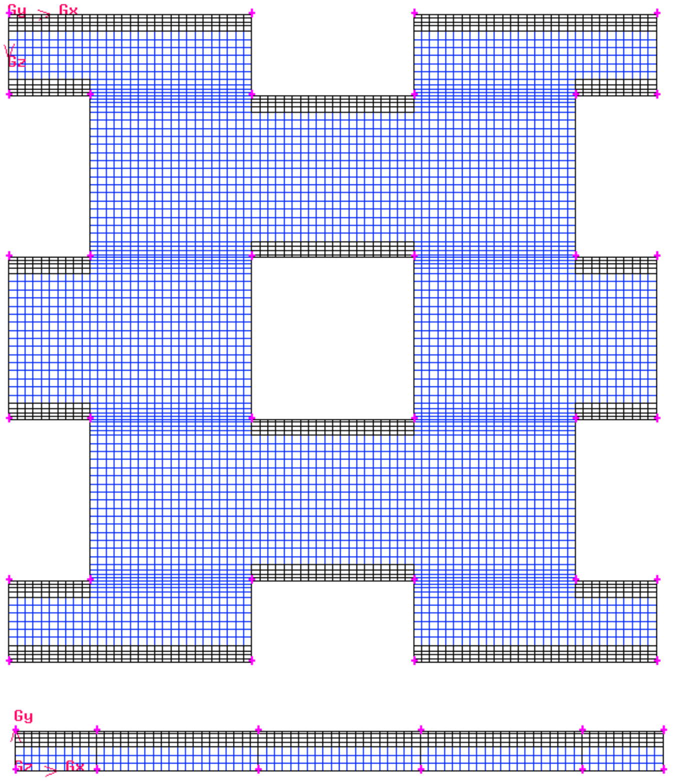

Figure 4.4: Mesh of a portion of the central part of the micro-reactor employing periodic boundary conditions

The following operating conditions are employed throughout all simulations:

Flow rate = 80-100,000 reformate ml/Hr/gm of catalyst

Temperature = 255°C

H_2O : MeOH = 1.5:1 (Molar)

O_2 : MeOH = 0.3:1 (Molar)

Loading of catalyst = 0.00583 $\mathrm{mg/mm^2}$

Catalyst loading = 5 mg/chip

Figure 4.5 shows a typical result of the CFD simulation. The flow pattern is shown for the middle plane of the chip. The flow is maximum at the center of the channel between the two solid surfaces, reproducing a laminar channel flow behavior. The main goal of studying the flow pattern is to resolve the dead spaces near the entrance section of the chip. The area in which the flow velocity is too low is a dead region for the catalytic reaction and thus adversely affects the overall performance.

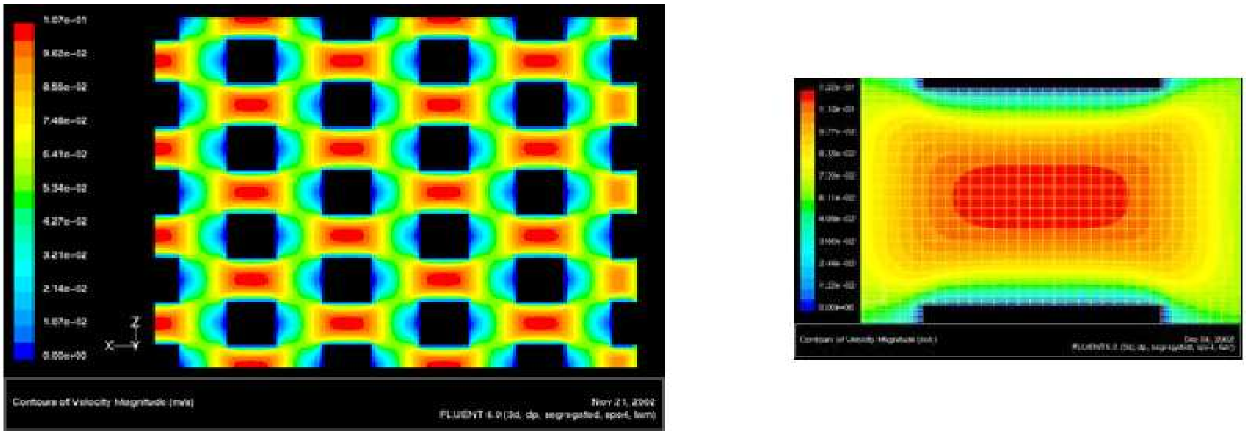

Figure 4.5: Contours of flow in the micro-reactor channels

Another concern is channeling of the flow in the reactor channels. The flow pattern may develop thin boundary layers near the solid wall such that the bulk of the flow simply passes through the channel without sufficient contact with the catalytic surface. To ensure that the overall mixing length at the entry of the reactor, a modified simulation is performed by blocking alternate inlets into the chip. The results are shown in figure 4.6 and confirm that the flow returns to the original flow pattern within two pattern lengths. Thus channeling is not considered a serious concern in this reactor configuration.

4.7 Mirco-reactor redesign and CFD flow analysis

During the development process, flow leakage is also found to be a serious problem near the entry and exit manifolds. To overcome this problem, the chip is redesigned into the inlet manifold built into the chip itself, as shown in figure 4.7. Instead of feeding directly

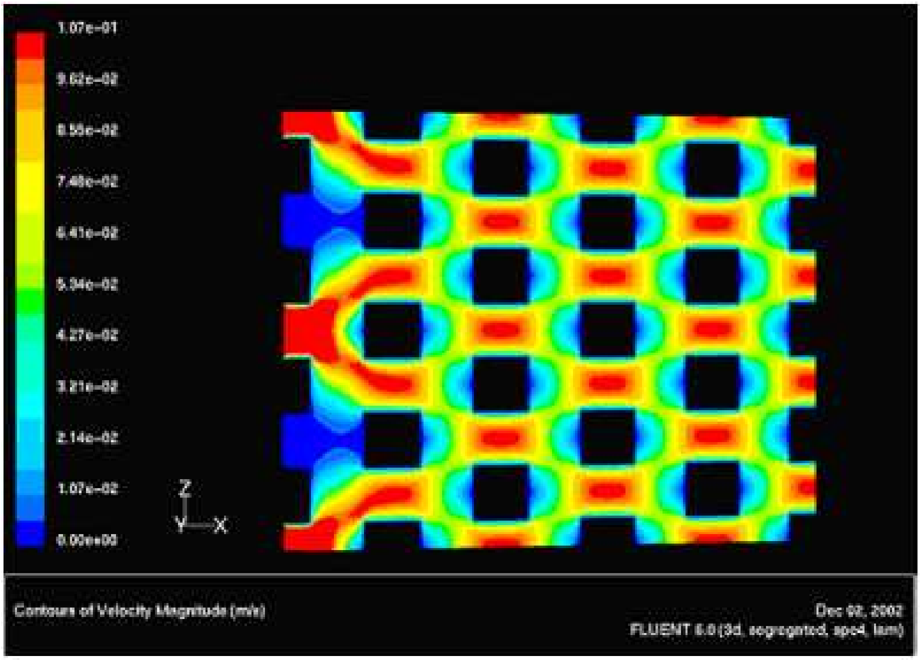

Figure 4.6: Entrance region flow pattern with alternate inlets closed

through the full face of the chip, fluid now flows down a common hole and then distributes in the chip through eight inlets. These inlets are made narrow to provide a back pressure into the feed system. This ensures an even flow into every inlet.

The redesigned micro-reactors are 6 cm x 6 cm and have anodically bonded pyrex covers with inlet and outlet holes. Flow manifolds are provided in the micro-reactor itself. The active region of the micro-reactor also had staggered rows of “pillars” for efficient mixing. The etch depth is approximately 200 mm and the characteristic dimension (hydraulic diameter) is approximately 400 mm. Pictures of the fabricated micro-reactor are shown in Fig. 4.7.

The obstruction pattern is also changed from the earlier square pattern to a much smaller oval pattern. As a result of this change, the void area in the chip increases and results in a drop in the peak velocity (Fig. 4.8[right]). Peak velocity in the modified design is found to be slower by an order of magnitude(approximately 1 cm/s as compared to 10 cm/s earlier), allowing a longer residence time for the flow.

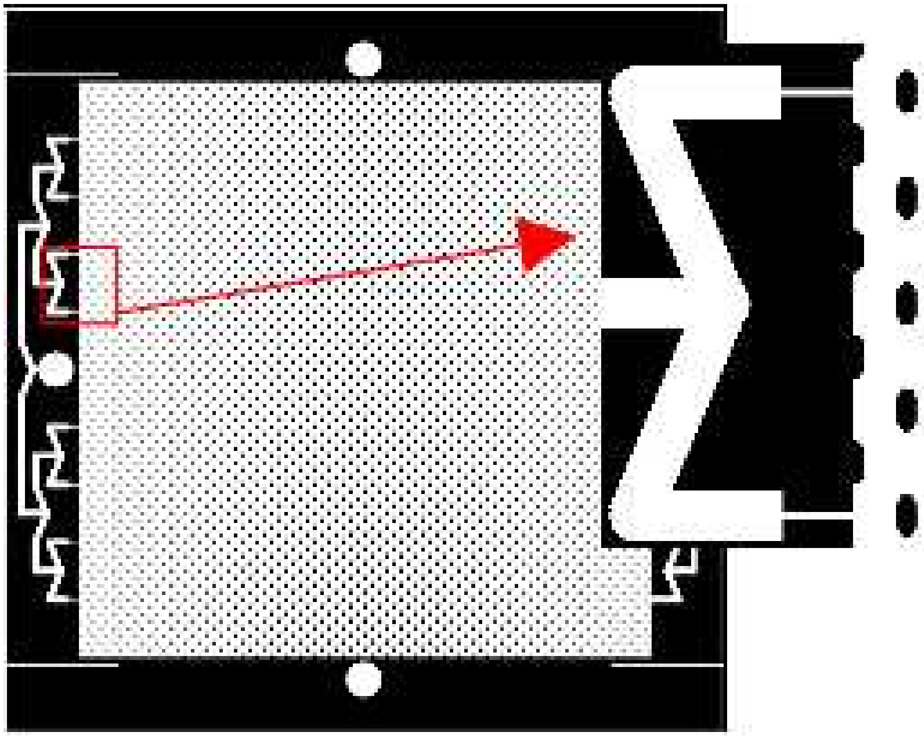

Figure 4.7: The redesigned micro-reactor with inlet and exit manifolds built-in

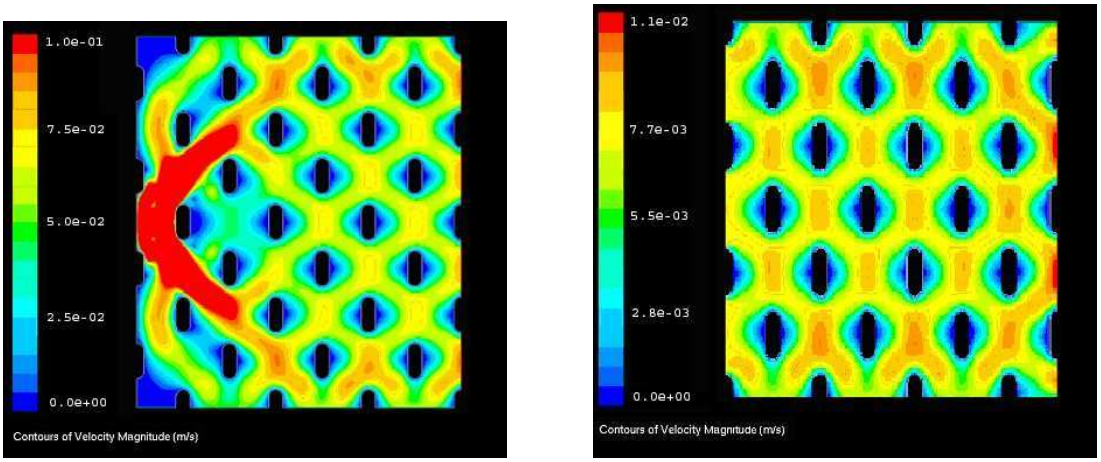

Figure 4.8: Contours of flow in the redesigned micro-reactor channels: entrance(left) and interior(right)

To visualize how the flow spreads out from a thin inlet, a model containing just one inlet is constructed. Results from this simulation can be seen in figure 4.8[left]. Some dead areas observed on either side of the inlet. However, the flow still manages to spread out rapidly, yielding a very small entry length of approximately 2% of the length of the reactor. The flow is thus considered well mixed throughout the micro-reactor.

4.8 Experimental work

The silicon micro-reactor experimental set-up consists of a custom built aluminum housing (8 cm × 8 cm × 1 cm upper and lower blocks) with inlet and outlet Swagelok connections. High temperature silicone rubber is used as a hermetic gasket material. External heating is provided using cartridge heaters placed in the lower aluminum block. Fig. 4.9 shows details of the micro-reactor housing assembly. For the packed-bed U-tube reactor studies, the powder catalyst is packed in a quartz U-tube using glass wool and heated using a ceramic box heater.

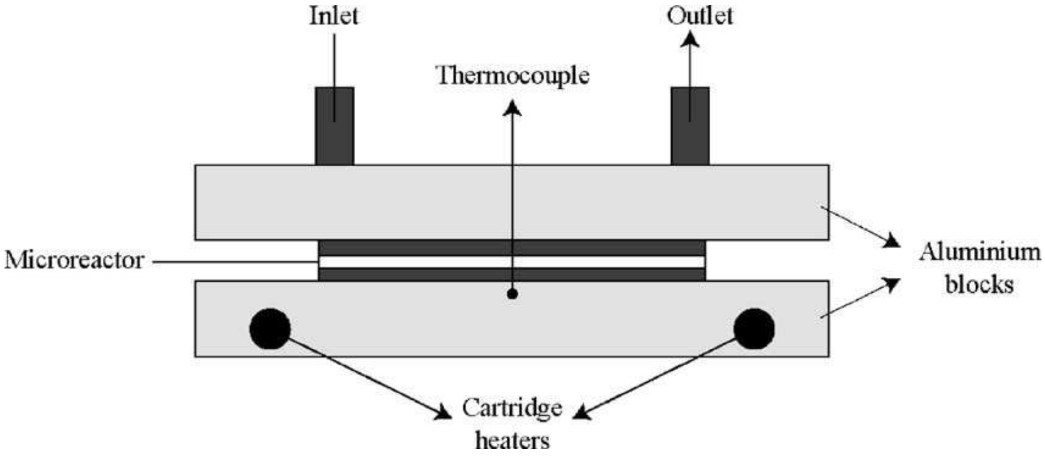

Figure 4.9: Silicon micro-reactor housing assembly

The catalyst is pre-treated by reduction in H_2 at 250°Cfor 4 hours. The reaction mixture is then passed through the wall-coated silicon micro-reactor and the temperature is varied between 150 and 250°C in steps of 20°C. It should be noted, however, that the thermocouple used with the temperature controller is placed in the aluminum housing just below the bottom surface of the silicon micro-reactor. This is not an actual representation of the temperature of the catalyst coating inside the micro-channel. Therefore, an attempt is made to correlate the catalyst temperature with the thermocouple reading.

The PrOx reaction is carried out under dry conditions and without any CO_2 in the inlet stream, which had a composition of 60% H_2, 1% CO and 1% O_2 (stoichiometric coefficient, $\lambda = 2$) in argon. Parameters defined in equations 4.6–4.9 are used as before to evaluate the performance of the reactors.

Weight hourly space velocity (WHSV) is calculated by dividing the volumetric flow rate under normal conditions by the weight of the catalyst used. The WHSV is maintained at $120000\ \mathrm{cm}^3\mathrm{h}^{-1}\mathrm{g}$-cat^{-1} for both reactors. Thus, the reactant flow rate, normalized with respect to the weight of the catalyst used, is used as the fixed parameter to evaluate and compare the performance of the two reactors. Reactant and product compositions are obtained using a dual channel Varian CP-4900 micro-gas chromatograph employing a thermal conductivity detector. Temperature measurements are made using K-type thermocouples. Reactant flow rates and pressure are controlled via PORTER mass flow controllers. A schematic of the experimental set-up is shown in Fig. 4.9.

4.9 Thermal simulation

A simulation of the silicon micro-reactor and the aluminum housing under steady state heating is undertaken using FLUENT[62]. Standard ambient heat loss are assumed from the outside surfaces of the heating block. Note that, although PrOx is an exothermic reaction, the heat generated by the PrOx reaction at the flow rates under consideration (100 cm^3/min with 1% CO) is approximately 0.2 W, which is negligible compared to the ambient heat loss which is estimated at 35–40 W. The silicon base of the micro-reactor with its excellent thermal conductivity, coupled with the aluminum block, behaves like a heat sink and washes out this small amount of heat generated. Therefore, for simplicity, the system is modeled assuming flow of an inert gas such as argon. In addition, the modeling is performed assuming a flat horizontal enclosed channel, while in reality the silicon base has vertical pillars which behave as fins, further contributing to the heat sink.

The simulation results are shown in Fig. 4.10. The lower aluminum block and the silicon base are approximately at the same temperature, and there is hardly any gradient in the vertical or the horizontal direction. This is reasonable since both these materials have excellent thermal conductivity. However, there is a sharp temperature drop within the micro-channel of approximately 20°C. The interface between the channel and the glass cover also sees a drop of approximately 10°C, beyond which there is not much decrease in temperature throughout the upper aluminum block. Note that the catalyst has been coated not only on the silicon surface of the micro-reactor; it also covers the entire inner surface of the micro-channel reaching the glass surface. For the particular model results shown here, the temperature within the micro-reactor varies from 150–170°C. Therefore, a reasonable approximation of the catalyst temperature would be the average temperature inside the channel which is approximately 10°C lower than the temperature read out by the thermocouple placed in the lower aluminum block. This correction is applied in reporting the catalyst temperature for the wall-coated micro-reactor.

4.10 Results

4.10.1 Comparison to packed bed reactors

For comparison of the micro-reactor to a packed-bed reactor, similar experiments are conducted using a U-tube packed-bed reactor. As in the case of the wall-coated silicon micro-reactor, the catalyst is pre-treated in the same manner, and the reaction mixture is passed through the packed-bed reactor. A key parameter is the temperature. The temperature control used is the same as the earlier case. For matching the temperature a thermocouple is directly placed within the packed-bed reactor, inside the catalyst bed touching the power catalyst. Hence, no temperature correction is needed for the packed-bed setup. For the

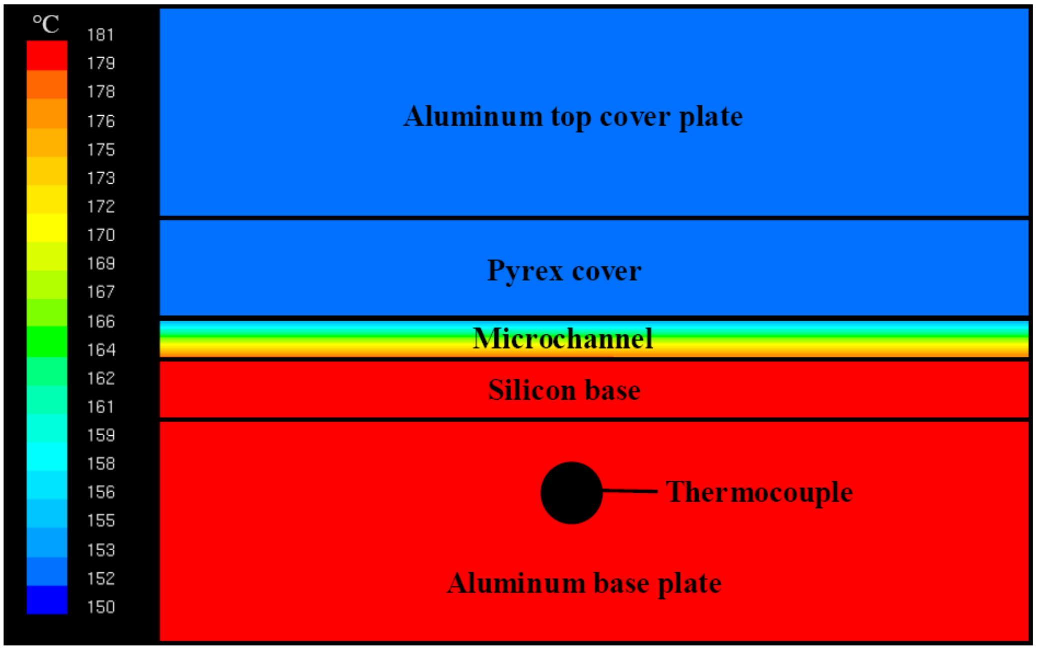

Figure 4.10: Temperature profile in a section of the micro-reactor housing assembly

micro-channel, temperatures were corrected using CFD simulations as described in Section 4.9. Also, the micro-reactor and packed-bed reactor characteristics are matched as far as possible. The GHSV for both reactors is kept the same, the amount of catalyst in both reactors is also matched.

The diffusion length scale in the micro-reactor from Section 4.3 is $400\ \mu\mathrm{m}$ while particle size in the packed-bed is given to be around $500\ \mu\mathrm{m}$ from Section 4.4. These similar diffusive length scales mean that the diffusion time scales are on the same order of around 20 milli-seconds. The residence time in the reactors is more than one second such that any external mass transfer effects would not have an effect and the flow can be taken as fully mixed in both packed-bed and micro-reactor setups. The internal mass transfer effects are taken to be the same since the catalyst and the flow characteristics are the same.

Figure 4.11 shows a comparison of the O_2 and CO conversion obtained from actual experimental runs performed on the wall-coated silicon micro-reactor and the packed-bed reactor. The results obtained from both types of micro-reactors show good agreement with each other. This validates the fact that there are no external mass transfer limitations that

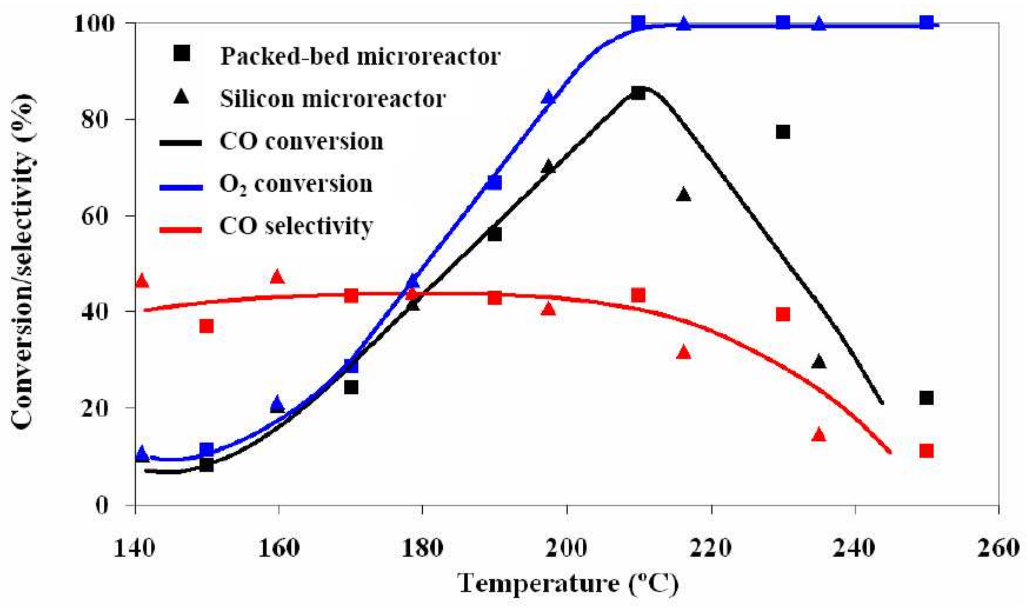

Figure 4.11: Comparison between packed bed-and the silicon micro-reactor

arise in using the wall-coated micro-reactor as compared to the packed-bed micro-reactor. For both reactors, the O_2 conversion showed an increasing trend with temperature and reached 100% conversion at approximately 210°C. The CO conversion increased with temperature until about 210°C and then begins to fall.

Figure 4.11 also shows the measured selectivity of the PrOx reactions, where consistent behavior is observed for both micro-reactors over a wide range of temperatures. The selectivity to CO oxidation is fairly stable near 45% until about 210°C, beyond which it begins to decrease. Selectivity implies the competition between CO and H_2 oxidation in the PrOx reaction process. In the absence of CO, the oxidation of H_2 over Pt is instantaneous, even at room temperature. However, when CO is present in the mixture, CO predominantly covers the Pt catalyst surface and inhibits the oxidation of H_2. As the temperature is increased, the rate of CO oxidation increases and hence we see an increase in both CO and O_2 conversion. However, at the higher end of temperatures (beyond 200°C), CO begins to desorb from the catalyst surface resulting in partial coverage of the surface by CO, thus allowing the oxidation of H_2 to proceed at a faster rate. Hence, oxidation of H_2 now becomes dominant and we see a sharp fall in the CO conversion as well as the selectivity to CO oxidation[47]. No methane formation is observed in either case.

Examining equations 3.18 and 3.19 we do see that the temperature has an exponential effect on the reaction rate in these reactors and is the most dominant effect[35]. Since both reactors operate in the (fully mixed) regime and the other parameters(diffusion length, GHSV, etc.) and especially the temperature is kept the same we see similar conversion rates and efficiencies. Thus as long as the operating regime of the reactors is similar along with other parameters, a packed-bed and micro-channel reactor will yield similar conversion rates.

4.11 Scale up

Based on the results obtained from the single micro-reactor system, a prototype scale-up method for the micro-reactors can be developed. The method involves stacking the micro-reactors and bonding them using glass frit bonding. By this method the capacity of the system cab increased while at the same time reducing heat loss to the ambient due to the decreased surface area to reactor volume ratio. The reactors are also designed to be discrete so that separate reactors can be coated with separate catalysts and carry different reformate feeds.

Chapter 5

Silicon Micro-reactor with an Integrated Platinum Heater

5.1 Introduction

In the previous chapter, silicon micro-reactor was designed and fabricated for preferential oxidation of CO that forms through the reforming of hydrocarbon to hydrogen. It was shown that micro-reactors could be used for selective CO oxidation at a level comparable to that of packed bed reactors without the negative effects of pressure drop and mass transfer limitations. Compared to the macro-scale, packed-bed type reactors, micro-reactors have many advantages of better thermal management and mass transport, allowing more precise control of chemical reactions[36]. They can also be scaled up more easily and provides a flexibility in the design to achieve compact and efficient thermal integration[17, 25].

One of the main design challenges of micro-reactors is to maintain a desired temperature within each reactor component with minimal heat loss to the surroundings. To achieve this goal, a careful thermal integration among various reactor components is the first critical step. Even with the most effective thermal integration, however, it is sometimes necessary to provide additional energy into the reactor via an external heating device. In the previous chapter, this was achieved by use of cartridge heaters embedded in a bulky external aluminum housing. To further improve on this preliminary design and to fully utilize the benefit of the micro-reactors, it is necessary to integrate the heating system with the reactor into a more compact package. In this chapter, a platinum heater embedded on a glass wafer(Fig. 5.1) is utilized to make the whole assembly smaller. The new integrated heater/reactor design thus allows a more thermally efficient and compact reactor system.

This chapter presents a description of the modeling and experimental processes used in the design and fabrication of a thin-film platinum heater integrated with the silicon micro-reactor for preferential CO oxidation. The modeling effort includes an analysis of thermal characteristics of the system using FLUENT[62], as well as the reactor performance using POLYMATH[63]. Experimental measurements using the fabricated reactors are compared with the simulation results in order to assess the overall performance of the new micro-reactor design.

5.2 Platinum heater design and fabrication

In this study, a thin film of platinum was chosen as a resistive heater. To design the platinum thin-film heater (Fig. 5.1), an estimate of the deliverable power was needed. The silicon micro-reactor measures 6.5 cm × 6.5 cm and its thickness was $1100\ \mu\mathrm{m}$ (*i.e.* a $550\ \mu\mathrm{m}$ thick silicon wafer with a $550\ \mu\mathrm{m}$ thick pyrex wafer on top). The heater was integrated with the micro-reactor by employing a glass frit bonding method. The effective thickness of the micro-reactor system with the integrated heater was therefore $1650\ \mu\mathrm{m}$. To obtain the heater design parameters, the micro-reactor system was modeled as a 6.5 cm × 6.5 cm × $1650\ \mu\mathrm{m}$ heated plate held horizontally in ambient air.

To obtain the heater power rating, the plate was assumed to be heated uniformly. Heat losses from the thin vertical faces of the plate are assumed to be negligible compared to those from the larger horizontal faces. Since heat generation due to the PrOx reactions is small, at steady-state, the total heat loss from the device is assumed to be the power delivered by the heater. It was assumed that the plate was required to be heated to a maximum temperature of $400^{\circ}\mathrm{C}$. This therefore yields the maximum power generation by the plat-

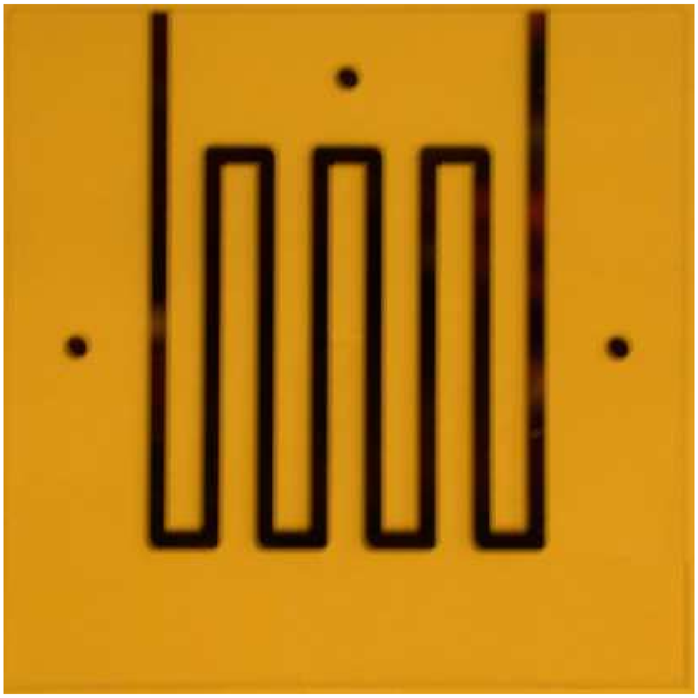

Figure 5.1: Platinum thin film heater deposited on a pyrex 7740 wafer

inum heater to be approximately 40 W. To account for radiative losses and an over-design safety factor, it was decided to operate on AC line voltage(110 V RMS AC) with a heating value of 60 W. This suggested that resistance of approximately 202 Ω would be required.

The cross-section of the deposited platinum is 2 mm wide and $0.1\ \mu\text{m}$ thick. Using the electrical resistivity of platinum, the required length of the heater is found to be 390 mm. To accommodate this length on a small chip, the heater is then designed as a single meandering platinum line in the center region of the bottom pyrex wafer.

An important consideration in designing the thin-film heater is that it needs to deliver the required power without electro-migration of the heater lines. Electro-migration is of particular significance in the case of thin films carrying electric current. If the current density in the film exceeds a certain threshold value called electro-migration limit, it can lead to a failure of the thin film. It is known that the electro-migration limit for platinum is approximately 10^{10} A/m^2[64, 65]. The maximum possible current through the thin-film heater is found to be 755 mA when the AC voltage reaches the peak value. The corresponding cur-

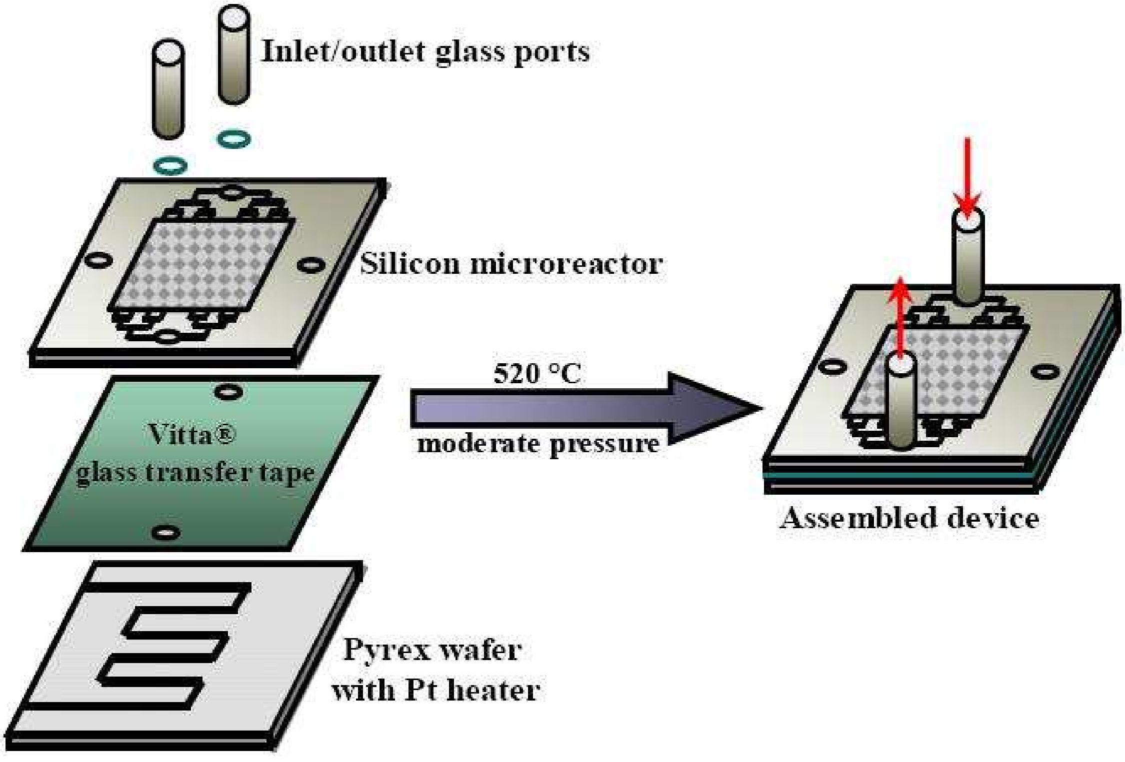

Figure 5.2: Glass frit bonding scheme

rent density is 3.77 $\times 10^9$ A/m^2. This value may seem to be close to the electro-migration limit. However the heater was designed for a temperature nearly 200°C higher than its operating temperature and the heater design wattage was subsequently increased as well. This ensures safe operation of the heater.

Another factor to be considered is dielectric breakdown. When a dielectric material or insulator is subjected to a potential difference that exceeds its breakdown voltage, the dielectric properties of the insulator are lost. For pyrex glass, the dielectric breakdown voltage is on the order of 10 kV/mm. Since the potential difference between the heater and all ground planes in the micro-reactor is significantly less than the dielectric breakdown voltage, dielectric breakdown is not expected to be a problem in the this design.

First, the heater pattern was created by electron-beam evaporation, and was transferred to a $550\ \mu\mathrm{m}$ thick Pyrex 7740 wafer by photo-lithography. A thin layer of titanium was first deposited in order to facilitate adhesion, and a $0.1\ \mu\mathrm{m}$ of platinum was subsequently deposited. Acetone lift-off was carried out to delaminate the undeveloped photoresist, which also removed the Ti-Pt film from unwanted areas. The glass wafer with the deposited Pt heater was then integrated with the silicon micro-reactor by employing glass frit bonding. Inlet and outlet ports (3 mm Pyrex tubes) are also bonded to the micro-reactor using glass frit bonding(Fig. 5.2). Glass frit tape was applied to the surfaces to be bonded, *i.e.* the lower surface of the silicon micro-reactor and the upper surface of the glass wafer. This was followed by multiple curing steps in a furnace. Under heat and pressure, the glass molecules melt to form an intermediate sealing layer which solidifies on cooling.

5.3 Thermal modeling

A 3-D CFD simulation with a full thermal model of the micro-reactor was performed using FLUENT[62]. Since the reactor itself was unmodified, the flow patterns in this system are the same as that shown in Chapter 4. Hence, in this chapter focus is on the thermal aspects of the system. We look at the prediction of the temperature profiles from the CFD simulations and verification through experimentation.

The 3D simulation included the micro-reactor itself along with the top and bottom pyrex glass covering layers. Since the thickness of the heater is $0.1\ \mu\mathrm{m}$, its thickness was neglected and was incorporated as surface heating at the interface of the bottom pyrex glass and silicon layers. Non-reactive PrOx reactant flow(1% CO, 1% O_2 and 60% H_2 in Ar) within the silicon layer was also considered. The intricate pattern etches in the silicon was not modeled similar to last time.

For calculation of the heat loss from the exterior surfaces, Rayleigh and Nusselt number correlations[66] are used to obtain overall ambient heat transfer convective coefficients for the upper and lower horizontal surfaces on the micro-reactor system. These are then developed into a local form so that they could be used in the simulations as user defined functions. Due to buoyancy, different local convection correlations for natural convection for upper and lower surfaces are calculated as:

$$h_{\text{upper}} = 4.2218\,(T_S - T_\infty)^{0.2773} \tag{5.1}$$

$$h_{\text{lower}} = 2.1109\,(T_S - T_\infty)^{0.2773} \tag{5.2}$$

The emissivity of pyrex glass is 0.82 and hence radiation effects are also taken into consideration for the simulation. The FLUENT simulations provided detailed 3-D temperature distributions for different heater power densities provided as an input.

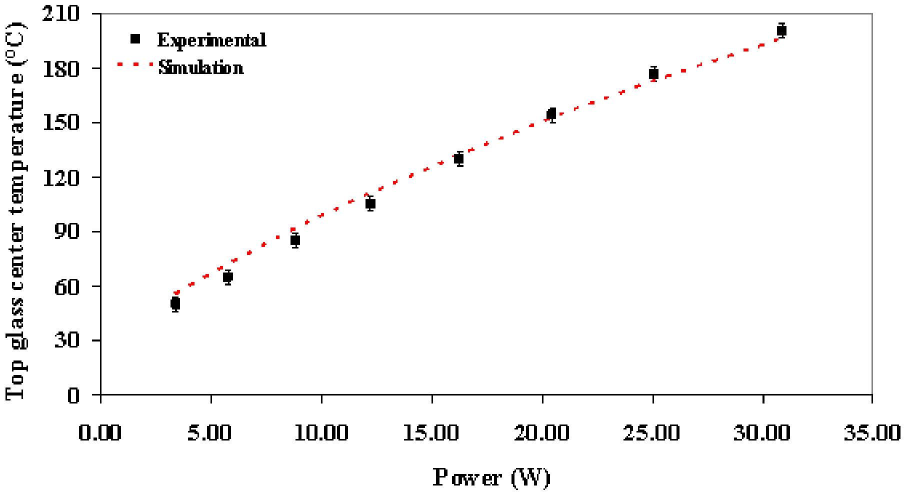

Figure 5.3: Comparison of predicted and experimentally measured temperatures at the center of the top glass plate of the micro-reactor

On the experimental side, the silicon micro-reactor system with the platinum heater was placed on three glass rods arranged in a triangle form in order to mimic suspension in ambient air. The thin-film leads are soldered to a copper wire and connected to an AC line through a variac. The variac is adjustable to provide between 0-100% of line voltage. The temperature at the center of the pyrex cover plate was measured using a K-type wire thermocouple. Care was taken to ensure that the thermocouple tip was in intimate contact with the pyrex cover plate. This was achieved by taping it down with high temperature Kapton adhesive tape. A milli-ammeter was placed in the thin-film heater/variac circuit to obtain the current flowing through the heater at different applied voltages. The product of applied voltage and current (both RMS values) through the heater is the power dissipated by the heater. For different applied voltages and powers, the temperature at the center of the cover plate was noted and compared with the values predicted for this location by the FLUENT thermal simulation.

A plot of experimental and predicted temperature values at the center of the top glass plate for different heating powers is shown in Fig. 5.3. It is shown that the FLUENT model predicts the experimental data within 5% over a wide range of heater power. The results confirm the model validation and predicts the overall temperature distribution in the micro-reactor system.

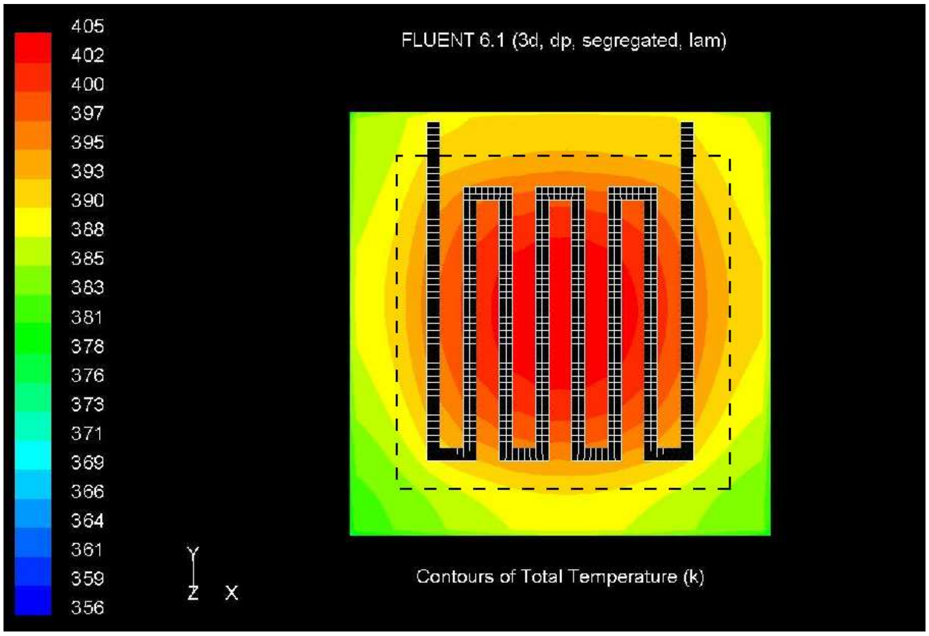

Figure 5.4: Temperature distribution: Glass silicon interface with Pt heater. The dotted line shows the location of the micro-channel over the heater

FLUENT simulations are then performed to examine the spatial temperature distribution on the reactor surface. A sample result for a heater power dissipation of 15 W is shown in Fig. 5.4 through 5.6. The temperature distribution in the reaction zone is seen to vary within 15°C, with a majority of the zone within 5–7°C(Fig. 5.5). Due to the narrow temperature distribution in the silicon micro-reactor, it concludes that the reactor operates under

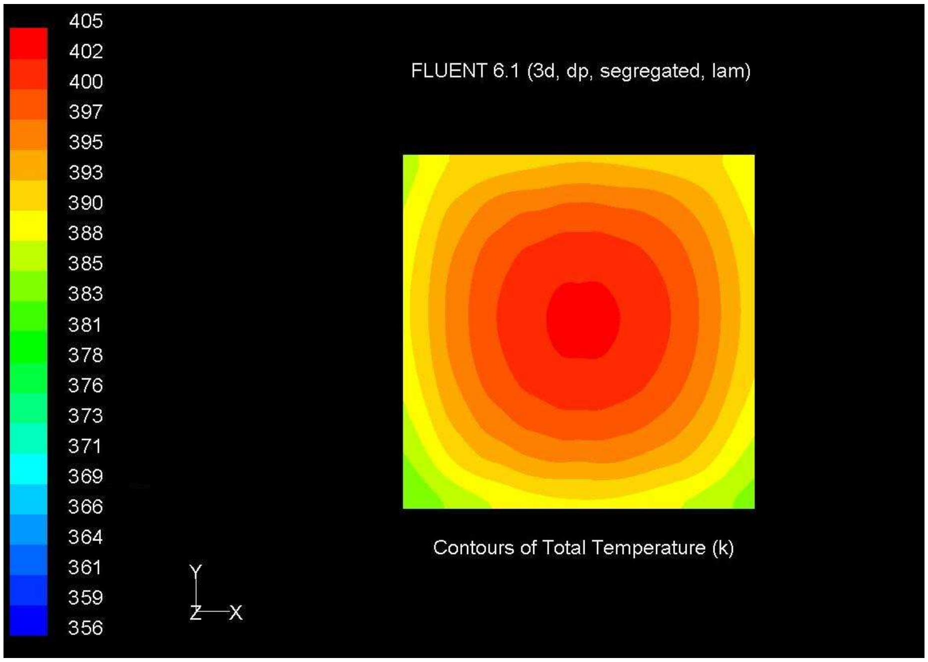

Figure 5.5: Temperature distribution: Center plan of reaction zone(micro-channel)

reasonably isothermal conditions, the reaction temperature being the average temperature in the micro-channel reaction zone.

5.4 Reaction modeling

In Chapter 4, the performance of the silicon micro-reactor was found to be similar to that of a packed-bed micro-reactor of comparable characteristic dimensions. A simplistic packed-bed micro-reactor model as a means to predict the performance of the silicon micro-reactor is thus developed. The aim of this model is to provide a reasonable design basis to determine the micro-reactor sizing and performance estimation. The following assumptions are made:

1. The system operates at steady state.
2. Convective transport is in one spatial dimension(axially along the gas flow).
3. The reactor is isothermal.

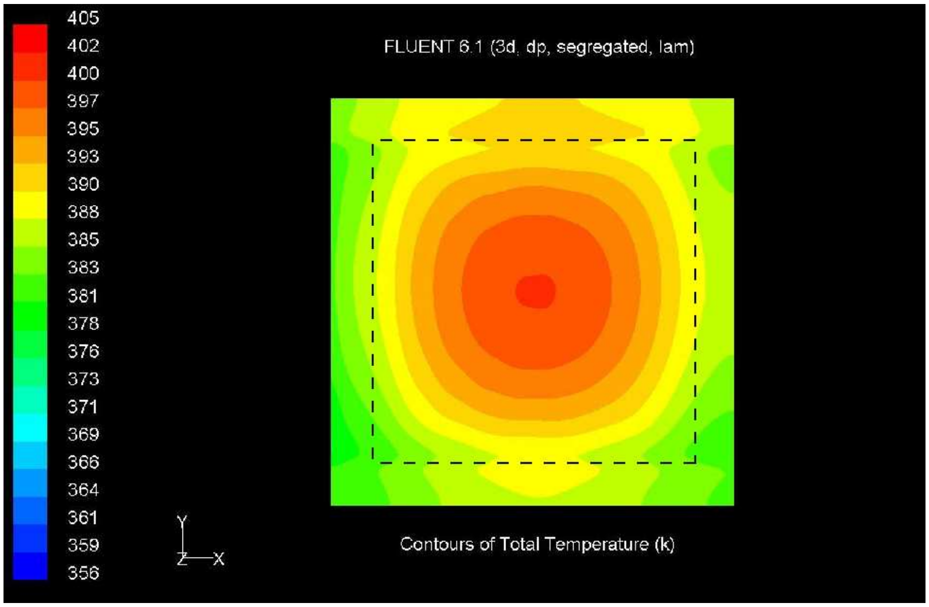

Figure 5.6: Temperature distribution: Glass cover plate. The dotted line shows the location of the micro-channel beneath the glass plate

4. Reactions are primarily the CO and H_2 oxidation on a Pt/γ-Al_2O_3 catalyst. Methanation and reverse water-gas-shift reactions are neglected. Kinetic rate constants for the CO oxidation are obtained from Kim *et al.*[47]
5. Selectivity of H_2 oxidation based on experimental evidence is assumed to be constant and equal to 50% (S=0.5).
6. Thermodynamic and transport properties are determined based on the mixture of excess H_2 and Ar, since CO and O_2 are in trace amounts.

The net PrOx reaction over Pt/γ-Al_2O_3 with both the CO and H_2 oxidation together is written as:

$$\mathrm{CO} + \frac{1-S}{S}\,\mathrm{H_2} + \frac{1}{2S}\,\mathrm{O_2} \rightarrow \mathrm{CO_2} + \frac{1-S}{S}\,\mathrm{H_2O}. \tag{5.3}$$

The species conservation equation[67] for CO is then given by:

$$-\rho_{bed}\frac{\mathrm{d}(V \cdot C_{\mathrm{CO}})}{\mathrm{d}W} = \kappa_{\mathrm{CO}} \cdot \psi \cdot (C_{\mathrm{CO}} - C^*_{\mathrm{CO}}), \tag{5.4}$$

where the right hand side represents the rate of CO transport from the bulk to the catalyst surface. A steady state is reached on the catalyst surface, such that

$$\kappa_{\mathrm{CO}} \cdot \psi \cdot (C_{\mathrm{CO}} - C^*_{\mathrm{CO}}) = \frac{(-r_{\mathrm{CO}})^* \cdot \theta_{\mathrm{Pt}} \cdot \chi_{\mathrm{Pt}} \cdot \rho_{bed}}{M_{\mathrm{Pt}}}. \tag{5.5}$$

The right hand side of equation 5.5 represents the CO consumption rate on the catalyst surface. A semi-empirical reaction rate was taken from literature(Kim *et al.*[47]) in units of turnover frequency (TOF, s^{-1}) per number of Pt sites.

$$(-r_{\mathrm{CO}}) = k_{\mathrm{CO}} \cdot e^{\left(\frac{-Ea}{R \cdot T}\right)} \cdot p^{\alpha}_{\mathrm{CO}} \cdot p^{\beta}_{\mathrm{O_2}}. \tag{5.6}$$

Following this the Pt loading in the catalyst and its dispersion was included in the expression. Since the micro-channels have a small characteristic dimension, the external mass transfer limitation was also neglected. Therefore, $C^*_{\mathrm{CO}} \approx C_{\mathrm{CO}}$, such that $(-r_{\mathrm{CO}})^* \approx (-r_{\mathrm{CO}})$.

Furthermore, since O_2 is present in trace amounts (1%), the volume change in the reaction can be neglected so that the total volumetric flow rate in the micro-reactor is approximately constant. The mass flow controllers are calibrated at room temperature. Combining Eqn. (5.4), (5.5) and (5.6) we obtain the conversion equation for CO as a function of the mass of the catalyst:

$$\frac{\mathrm{d}X_{\mathrm{CO}}}{\mathrm{d}W} = \frac{k_{\mathrm{CO}} \cdot \theta_{\mathrm{Pt}} \cdot \chi_{\mathrm{Pt}} \cdot T_0 \cdot (R \cdot T)^{\alpha+\beta}}{M_{\mathrm{Pt}} \cdot V_0 \cdot T \cdot C^i_{\mathrm{CO}}} e^{\left(\frac{-Ea}{R \cdot T}\right)} \cdot C^{\alpha}_{\mathrm{CO}} \cdot C^{\beta}_{\mathrm{O_2}}. \tag{5.7}$$

From the PrOx reaction stoichiometry, the conversion equation for O_2 is then derived as:

$$\frac{\mathrm{d}X_{\mathrm{O_2}}}{\mathrm{d}W} = \frac{1}{2S} \frac{k_{\mathrm{CO}} \cdot \theta_{\mathrm{Pt}} \cdot \chi_{\mathrm{Pt}} \cdot T_0 \cdot (R \cdot T)^{\alpha+\beta}}{M_{\mathrm{Pt}} \cdot V_0 \cdot T \cdot C^i_{\mathrm{CO}}} e^{\left(\frac{-Ea}{R \cdot T}\right)} \cdot C^{\alpha}_{\mathrm{CO}} \cdot C^{\beta}_{\mathrm{O_2}}, \tag{5.8}$$

and similarly for H_2 as:

$$\frac{\mathrm{d}X_{\mathrm{H_2}}}{\mathrm{d}W} = \frac{1-S}{S}\frac{k_{\mathrm{CO}} \cdot \theta_{\mathrm{Pt}} \cdot \chi_{\mathrm{Pt}} \cdot T_0 \cdot (R \cdot T)^{\alpha+\beta}}{M_{\mathrm{Pt}} \cdot V_0 \cdot T \cdot C^{i}_{\mathrm{CO}}} e^{\left(\frac{-Ea}{R \cdot T}\right)} \cdot C^{\alpha}_{\mathrm{CO}} \cdot C^{\beta}_{\mathrm{O_2}}. \tag{5.9}$$

This gives a set of three ordinary differential equations, which are subjected to the boundary condition:

$$X_{\mathrm{CO}} = X_{\mathrm{O_2}} = X_{\mathrm{H_2}} = 0, \text{ for } W = 0. \tag{5.10}$$

The set of the above differential equations are integrated using Matlab[49] to obtain the final conversion numbers.

Experiments were conducted, where a mixture of 1% CO, 1% O_2 and 60% H_2 in Ar was introduced in the silicon micro-reactor. Exit gas concentrations were measured using a Varian CP-4900 micro gas-chromatograph. The temperature of the micro-reactor was varied by adjusting the variac power. Due to the narrow temperature distribution in the silicon micro-reactor, as inferred from the FLUENT 3D thermal simulations, it is assumed that it operates effectively under an isothermal regime. The average temperature in the reaction zone of the micro-channel reactor is taken to be the reaction temperature for the reaction model.

The temperatures required for the reaction modeling are the average core reactor temperatures. However these could not be measured directly. Hence FLUENT simulations are used to determine the core reactor temperatures given the outer surface temperatures. From experimentation, the surface temperatures measured on the top of the glass plate are measured and simulations are performed in FLUENT so as to obtain the same temperatures at the same locations. Heat generated by the Platinum heater is also check for consistency. Using these simulations, the average temperatures for the core region of the reactor are calculated. These temperatures are then used in the reaction modeling.

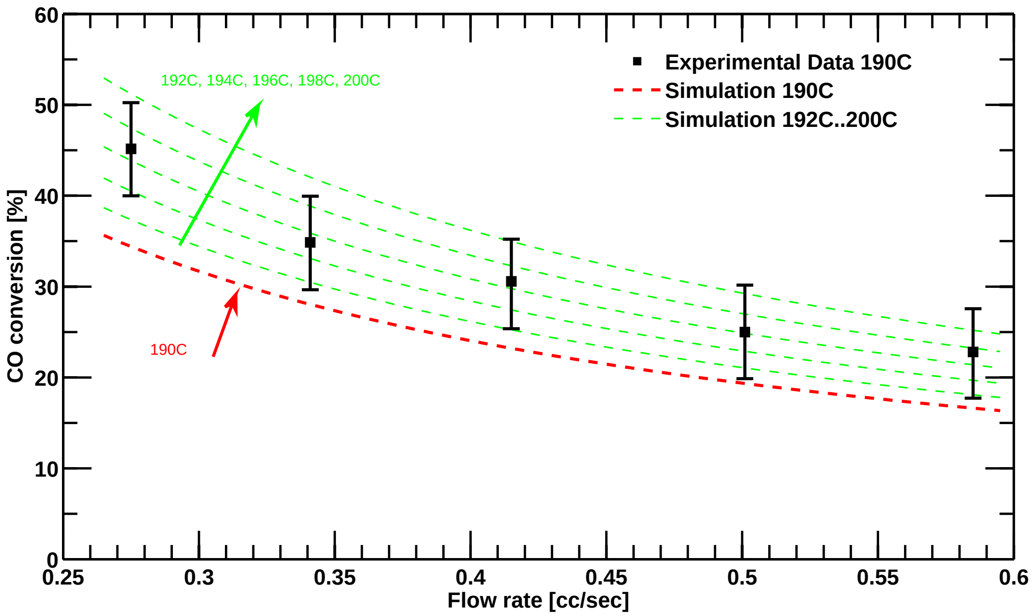

Figure 5.7: Comparison of predicted and experimentally measured CO conversions for different flow rates at constant heater power

The experimental CO conversion was determined by gas chromatograph measurements for a set of different heater powers (and hence for different average reaction temperatures). The isothermal packed-bed reactor model predicted a set of CO conversion values for these different reaction temperatures. The heater was found to be insufficient to sustain temperatures over 190°C. Thus comparisons at higher temperatures and conversion rates could not be made. Figures 5.7 and 5.8 show a comparison of the experimentally observed CO conversions with those obtained from the packed-bed micro-reactor model.

Figure 5.7 shows CO conversion as a function of flowrate of reformate in the micro-reactor at 190°C. The reaction model captures the experimental trend of CO conversion, however it consistently underestimates the conversion values. Arrhenius reaction rates are exponential in nature. Hence taking an average of a 2D temperature field would generally underestimate the reaction rates since higher than average temperatures have an exponentially higher effect as compared to lower than average temperatures.

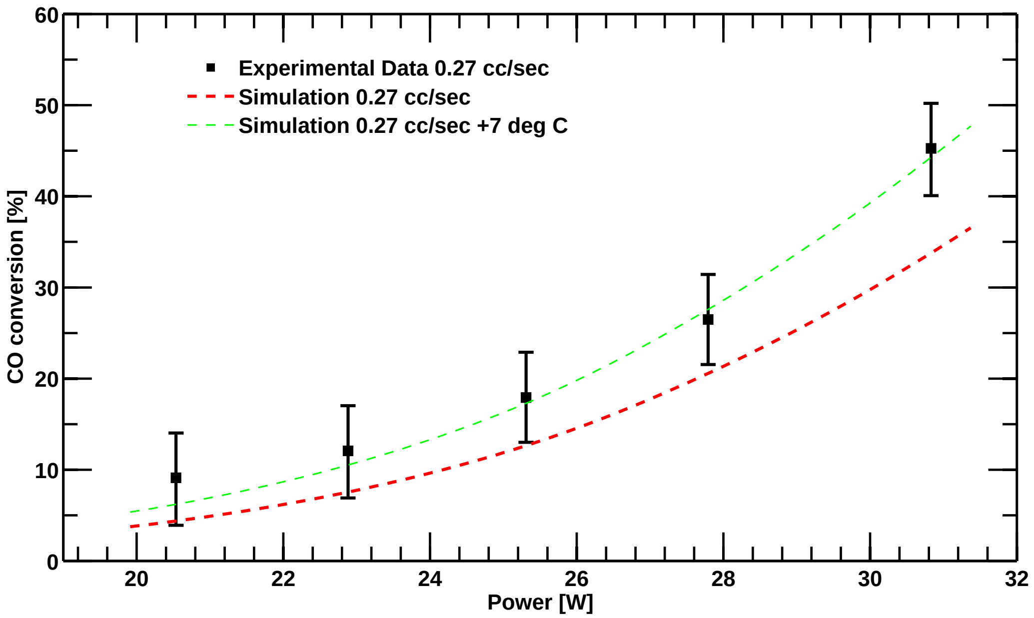

Figure 5.8: Comparison of predicted and experimentally measured CO conversions for different heater powers at constant flow rate

To understand the underestimation a sensitivity analysis is done using the reaction model. Results are generated at various temperatures above the average temp of 190°C. The temperatures used are 192, 194, 196, 198 and 200°C. Using this analysis we find that the temperature in the reaction model is underestimated by about 6–8°C. The higher temperatures are able to able to match the CO conversion numbers.

Figure 5.8 shows CO conversion as a function of heater power (or temperature from the reaction model). Similar to before, the model is able to capture the trend but underestimates the CO conversion values. To confirm the above hypothesis of the average temperature underestimating CO conversion, the reaction model was rerun at higher power levels so as to increase the average temperature by 7 degrees. It is found that by increasing the temperature by 7°C, the model results match the experimental data within 3%, thus confirming the hypothesis.

Collapsing a 2D or a 3D temperature field to an average temperature is found to underestimate the reaction rates since the Arrhenius kinetics are exponential with temperature.

A better methodology is to utilize a weighted temperature averaging that would be better suited to Arrhenius kinetics in order to increase the accuracy of the reaction model. However, it is clear that the packed-bed model describes the performance of the silicon micro-channel reactor in a satisfactory manner, thus establishing the validity of using such a model as a design tool for micro-channel systems.

Chapter 6

Design and Prototyping

This chapter describes the development and prototyping of the University of Michigan fuel processor design. Based on the collective knowledge and experience, the University of Michigan fuel processor team set an aim of designing a working prototype of an iso-octane/gasoline fuel processing system. A total of three prototypes were designed and built. This chapter will describe each generation of fuel processor built and the results of operating the fuel reformers. The author will describe in detail the modeling work performed to support the fuel processor development process.

6.1 Generation I

The Gen I design was the stepping stone which further led to the Gen II micro-reactor design. The Gen I design played a key role to gain further understanding of layered counterflow micro-reactors. The Gen I design utilized a counterflow scheme of alternate endothermic and exothermic reactions for recuperative operation.

6.1.1 Design

Figure 6.1 shows the prototypes for the Gen I micro-reactor. The Gen I micro-reactor is a layered micro-reactor. There are multiple thin plates sandwiched between two thick plates. The inner plates of the micro-reactor hold the metal foam in-between two plates. The metal foams are subsequently washcoated with the desired catalyst.

The layered structure in the Gen I prototype is used as a heat exchanger in the counterflow or coflow modes. Separate reformate feeds are channelled though alternate plates/layers in either the opposite direction (counterflow) or the same direction (coflow). This creates an arrangement where heat exchange takes place between two neighboring channels thus creating a reactive channel along with a heat exchanger similar to the model described in Chapter 3.

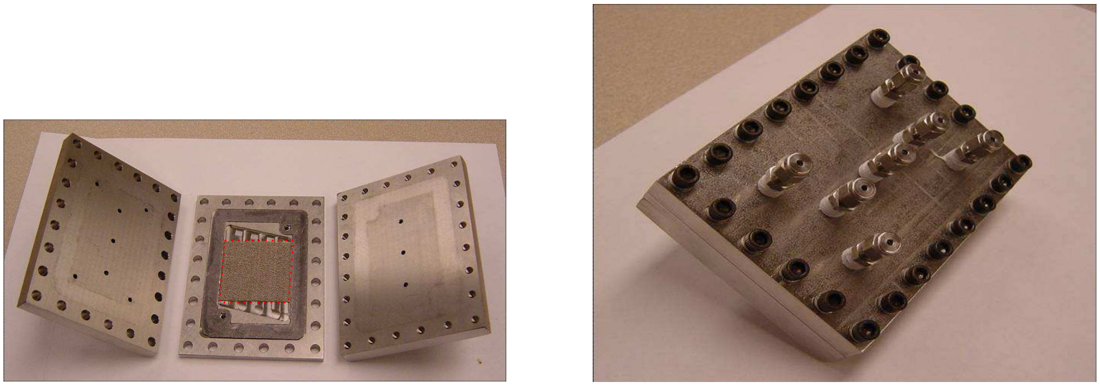

Figure 6.1: The first generation micro-reactor. The dashed red line outlines the metallic foam coated with the catalyst

6.1.2 CFD and thermal analysis

The central plates in the Gen I design contain a trapezoidal hollow section where a rectangular metal foam is seated. Each of these foams is washcoated with a suitable catalyst and located near the site of the catalytic reactions. To ensure that there were no dead spaces or flow channeling issues in these trapezoidal regions and the foams, a FLUENT flow simulation is performed to predict the flow pattern. The FLUENT simulations do not account for the effect of foam in the flow conditions due to the model limitations for porous media. It is anticipated that the foam would only mix with the fluid better and thus modeling without a foam would give us a worst case scenario. The flow analysis in figure 6.2 show the velocity profiles at every quarter length down the axial direction. The meshing for this simulations is shown in figure 6.3.

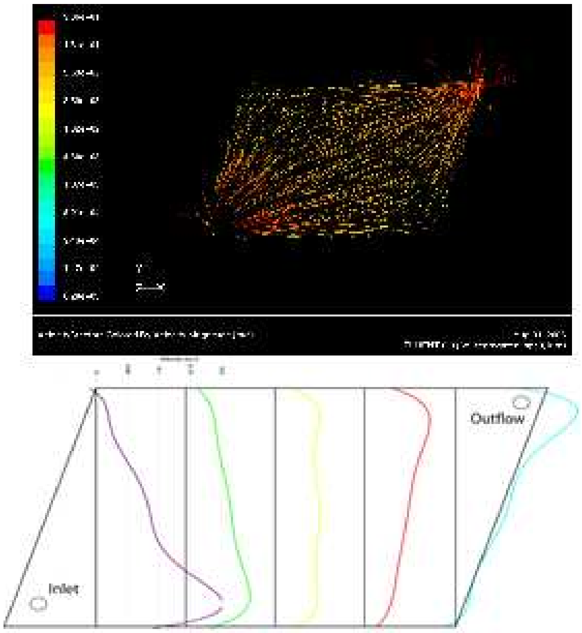

Figure 6.2: Flow field inside a single channel of the Gen I micro-reactor. High velocities are seen near the inlet and exit with small recirculation zones in the opposite corners.

The higher gas flow velocities through a channel of the Gen I micro-reactor design were observed near the inlet and exit regions. The small negative velocities in the top left and the bottom right corners, indicates the existence of recirculation zones, although they appear to be of minor significance. Furthermore, the presence of foam in the real prototype would mitigate these recirculation zones. Thus via a FLUENT analysis it was shown that the Gen I mircro-channel design would not have any maldistribuition of gas flow.

To assess the performance of the prototype as a heat exchanger, FLUENT thermal simulations are performed for the geometry shown in figure 6.4. The alternating four channels consist of two high temperature streams (red-923 K) and two low temperature streams (blue-400 K). The mass flow rate in both the reactor channel and the coolant channel was taken to be 0.4 gm/sec. Under these conditions, the heat transfer between the two sets of channels was found to be significant. Figure 6.5 shows the simulations results and plots the temperatures. The top plot shows the coolant entry side and the bottom plot shows the reactant entry side. Within a few millimeters of the inlet and the outlet the two flows

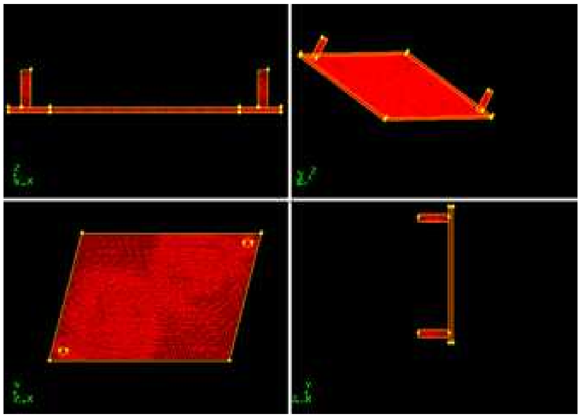

Figure 6.3: Model of a single channel with mesh of the Gen I micro-reactor

reached an equilibrium temperature. The results were confirmed by the experimental observations, thus the Gen I prototype was found to be inadequate for the present application. The ability of the design to adequately separate the temperature of the two feeds is the main requirement and the Gen I design could not achieve.

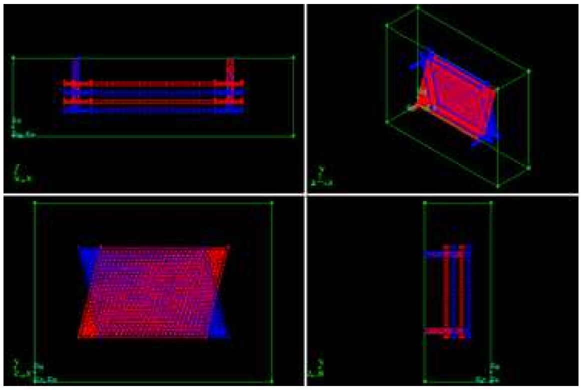

Figure 6.4: Mesh of multiple channels for thermal simulation of the Gen I micro-reactor. The red channels carry the hotter fluid, the blue channels carry the cooler fluid in the opposite direction

In summary, the Gen I design acted as a large heat sink and the device could not be heated up to operational temperatures. An alternative design, the Gen II is developed to overcome the limitations Gen Idesign.

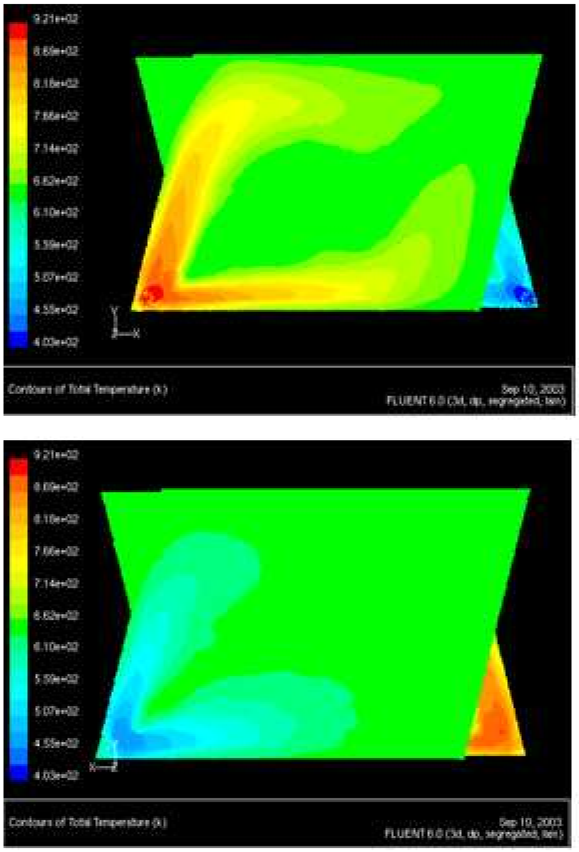

Figure 6.5: CFD prediction of the temperature profiles within the Gen I prototype reactor. Two figure show the reactant (top) and coolant (bottom) flow temperature fields of a counterflow-type reactor

6.2 The Gen II prototype

The Gen II prototype is designed considering the limitations of Gen I to lower the surface area to volume ratio and retain heat better in the system. This concept is designed considering the feasibility and manufacturability. The overall volume of the reactor was reduced by a factor of 25 while keeping the core reactor and catalyst volume the same. This gives a favorable surface area to volume ratio. In this particular design the individual reactors are linked together in a serial manner with a temperature controller for each reactor.

Recognizing that many problems with the Gen I prototype were caused by the large surface to volume ratio, the Gen II prototype is designed with a more compact package while maintaining the metal foam size for the catalyst as before. Figure 6.6 shows the modular components and the assembled reactor. Heaters are installed in the reactor for startup and temperature control.

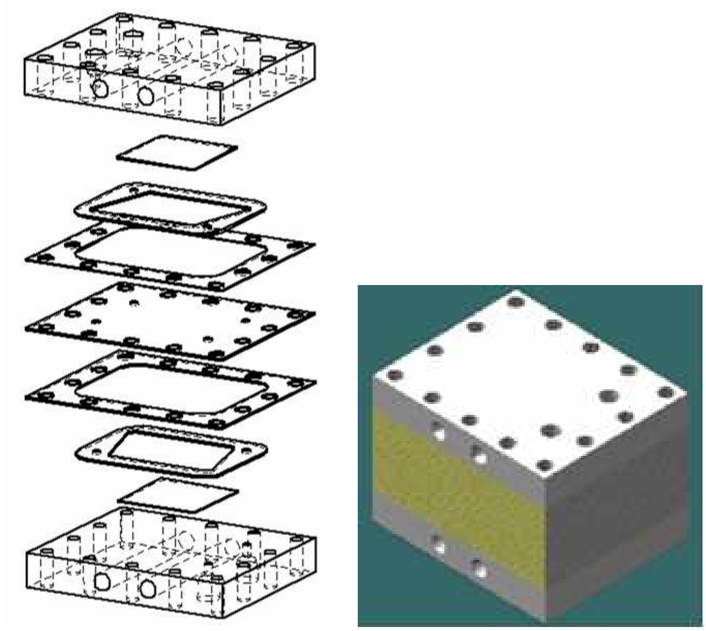

Figure 6.6: Exploded view of the second generation micro-reactor. The assembled version on the right show 25 layers

The design consists of metal plates placed in layers. In the Gen I design, the inner plates were milled to form the trapezoidal groove in the plates where the metal foam was placed. This process was time consuming and costly. In the Gen II design, each inner plate is replaced by two separate plates. One is a complete plate while the other plates a full depth hole cut in it. By placing these two plates together the trapezoidal grove similar to the Gen I design was obtained. Since these plates are laser cut, they cost much less to produce. Gaskets are introduced around the foam to prevent leaking and to hold the foam in place.

In the Gen I reactor, startup of the system was found to be a critical issue. Even after starting, the reactor could not sustain its operating temperature. Thus, in the Gen II design, heaters were incorporated into the reactor to initiate high temperature for startup. For startup, the Gen II prototype requires heating up to a temperature of about 300 °C. To check whether the system would start up and achieve a stable temperature within a few minutes, high wattage heaters were incorporated into the design. Based on calculations done with 500W of heating per reactor, the startup time was estimated to be around 1.2 minutes. These were used as startup heating devices and also to control the temperature of the reactor during the operation.

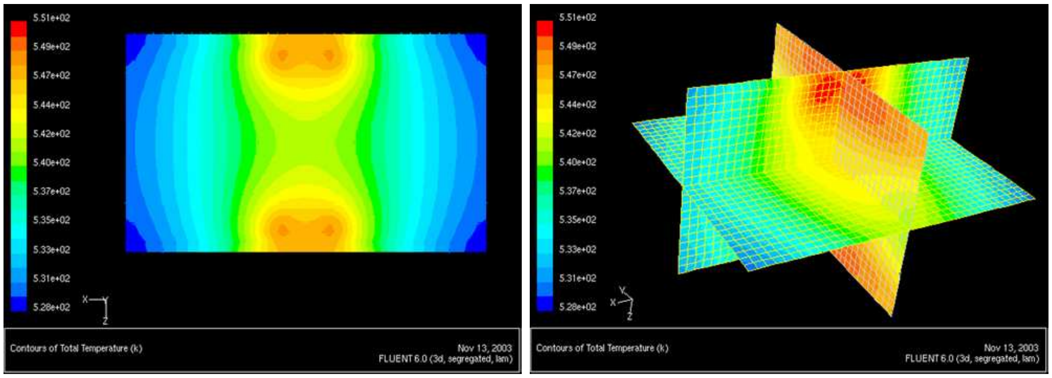

Figure 6.7: Gen II predicted temperature profiles in a cross-section(left) and the mid-planes(right)

One of the concerns with this design is that these heaters may generate hot spots in the reactor. The hot spots can not only cause a drop in reaction efficiency, but also cause excessive thermal stresses in the reactor leading to leakage and failure. With uneven heating present in the reactors, the temperature distribution in the reactors could be very uneven. This would lead to hot or cold spots in the reactors which would lead to thermal stresses, warpage, leakages and even failure of the reactors. Thus to understand the temperature distribution in the reactors, a FLUENT thermal simulation is undertaken. The ATR being the hottest reactor in the system is chosen for the simulation. From the heat loss calculations, it was estimated that about 80 W of heating would be required to keep the ATR at a steady state temperature of close to 700 °C. In the model, 4 heaters of 20 W each were used. This system is solved for steady state with convective and radiative heat loss to the atmosphere. Figure 6.7 shows the temperature distribution obtained from the simulations in the Gen II reactor. The four bright red spots are the heaters in the reactors The corners of the reactor were found to be the coldest. Nevertheless, the difference between the hottest and the coldest spots in the core region of the reactor is found to be less than 25 °C. This core region is where the catalyst washcoated metal forms sit and hence the reactor is found to be fairly isothermal under operating conditions.

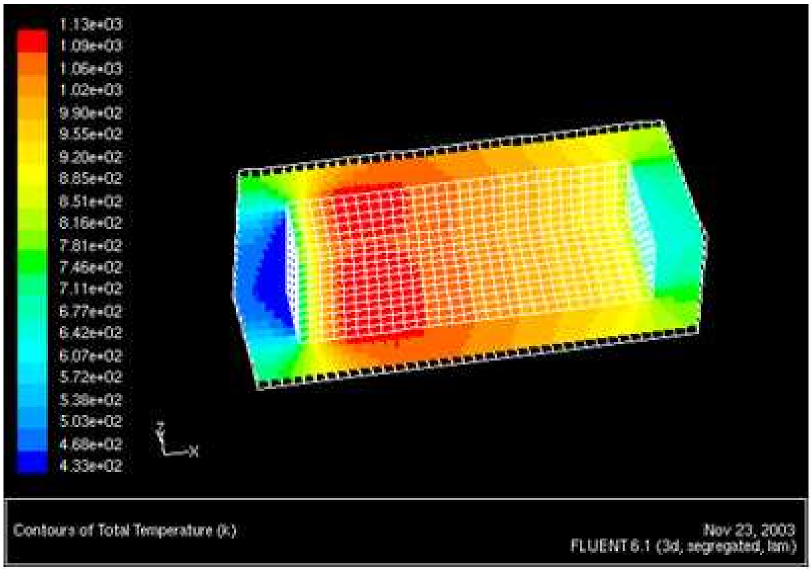

Figure 6.8: Gen II predicted temperatures in the quarter section

Thermal stresses are expected to be maximum in the ATR, which operates at a much higher core temperature(700 °C) than any other reactor in the system. A second FLUENT thermal simulation to predict a variation in temperature in the ATR was undertaken. For this simulation the mesh from the previous simulation was used. The expected temperature profile for the ATR was plugged into the reactor model as in input boundary condition. The temperature profile for an ATR rises steeply to its maximum temperature of 900 °C in the first 10% of the catalytic metal foam and then reduces linearly to 650 °C by the end of the metal foam. This is implemented into FLUENT as a user defined function with a predefined temperature as described above.

Due to symmetry of the model of the reactor design, only a quarter of the reactor is required to be modeled. The results of this simulation are shown in figure 6.8. On the inlet side the temperature decreases more than 600 °C from the metal foam tip to the outer surface on the reactor. On the outlet side, this temperature drop is less than 500 °C. Thus the simulation shows a steeper temperature gradient on the inlet side This implies that the reactor is more prone to warpage and leakage on the inlet side of the ATR. During experimental work we did observe leakage on the ATR and this due to warpage. As a remedy, the inlet and exit ports were welded to the reactor body for the ATR. Welding of the ports was not required for the other reactors (WGS and PrOx) since the reactors operate at much lower temperatures and no leakage was observed during testing.

6.2.1 Generation II: System integration

With the Gen II design in place, a complete datasheet is drawn up (Appendix A) based on a 100 W_e (electric) system. All the reactors in the system , *i.e.* ATR, WGS 1, WGS 2, PrOx 1 and PrOx 2, are based on the Gen II layered design as shown in figure 6.6.

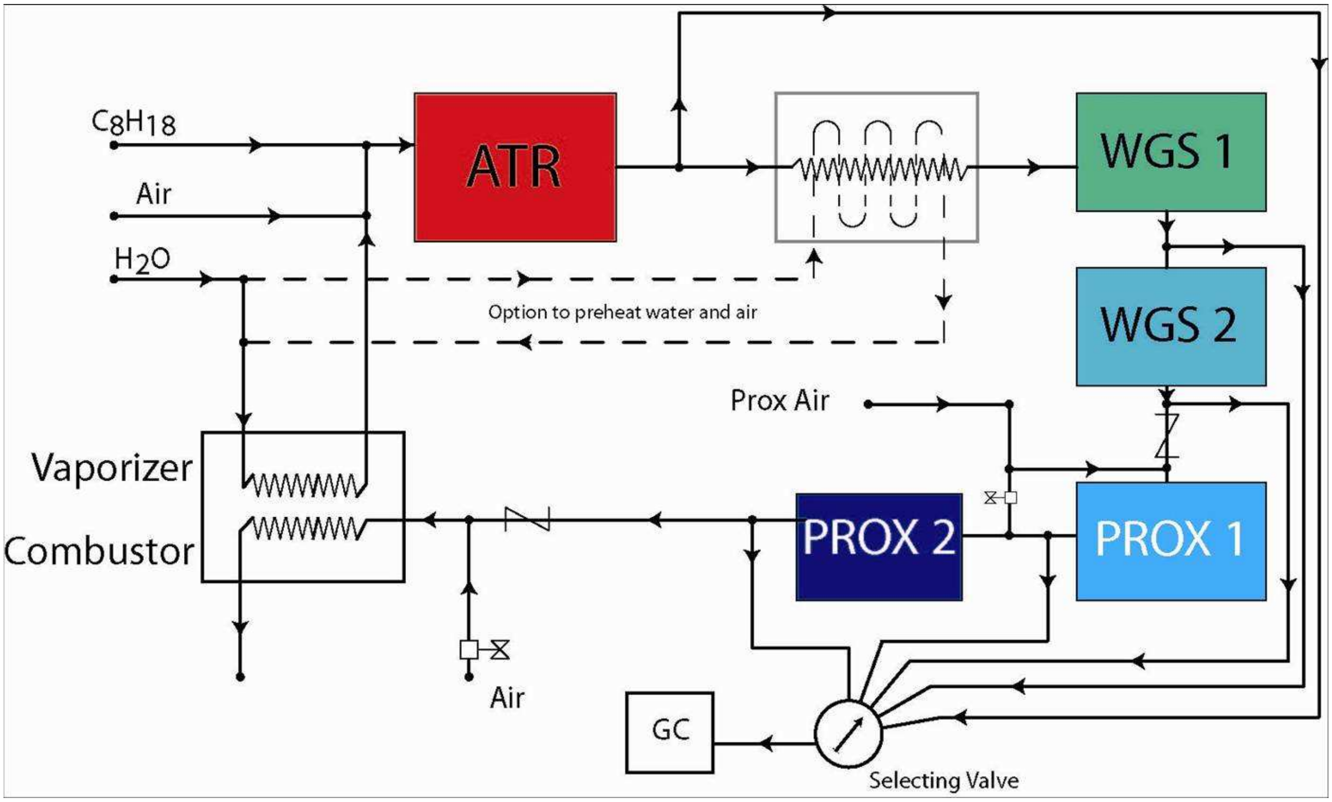

Figure 6.9: Gen II system flowchart

This system flowchart is shown in figure 6.9. Preheated water from the vaporizer/combustor is mixed with the air and the fuel and fed into the ATR. Two WGS reactors follow the ATR to clean up the bulk of the CO. This is followed by two PrOx reactors which further reduce to the CO concentration to below 10 ppm. This hydrogen-rich stream is fed into the fuel cell for power generation. Exhaust from the fuel cell containing residual hydrogen is then fed into the combustor for heat recuperation.

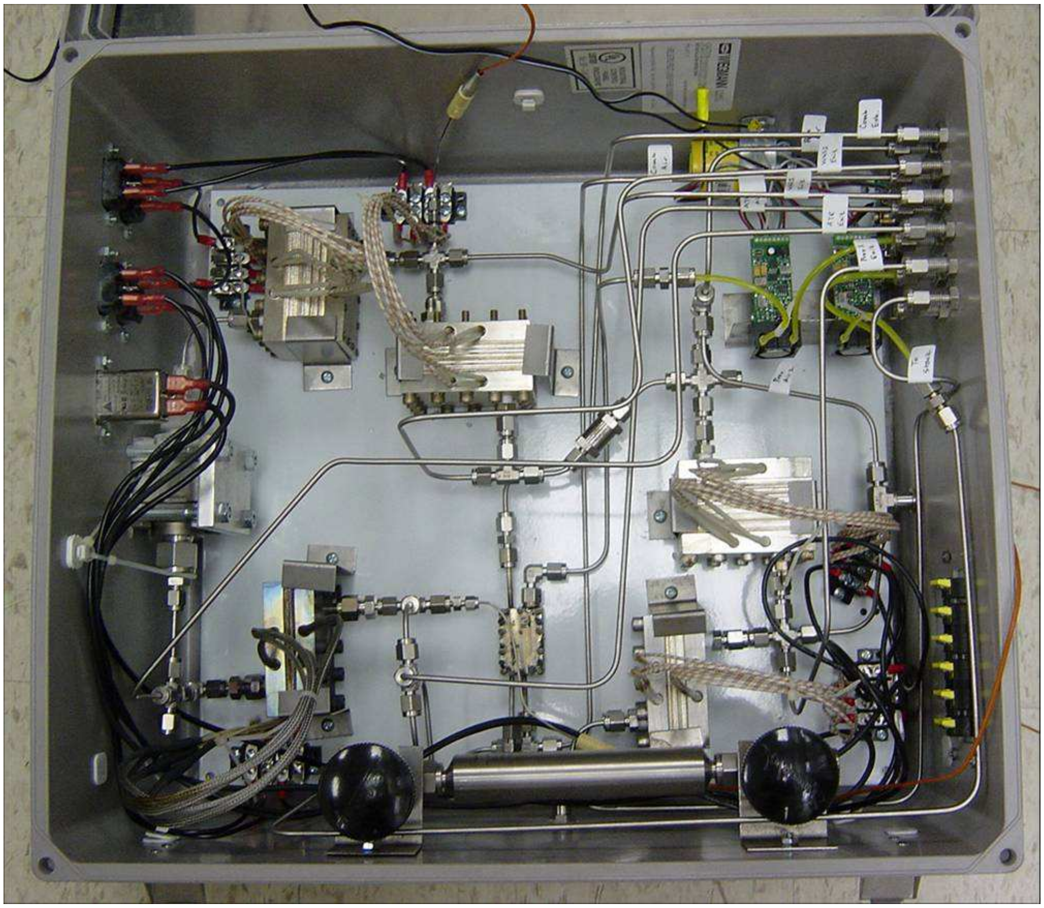

Figure 6.10: Gen II assembled system

During startup as the autothermal reformer comes up to temperature, it produces methane into the gas stream which might poison the downstream catalysts. To prevent that from happening a bypass valve is connected after the ATR which bypasses the rest of the system during startup. Once the ATR is up to temperature and functioning normally, the bypass valve is closed routing the gas stream to the WGS and PrOx reactors.

Each component is controlled individually to its operational temperature by the embedded heaters totalling 80 W of heating power per reactor. The number of catalytic metal foams in each reactor is based on the required space velocity of the reactor. Thus while

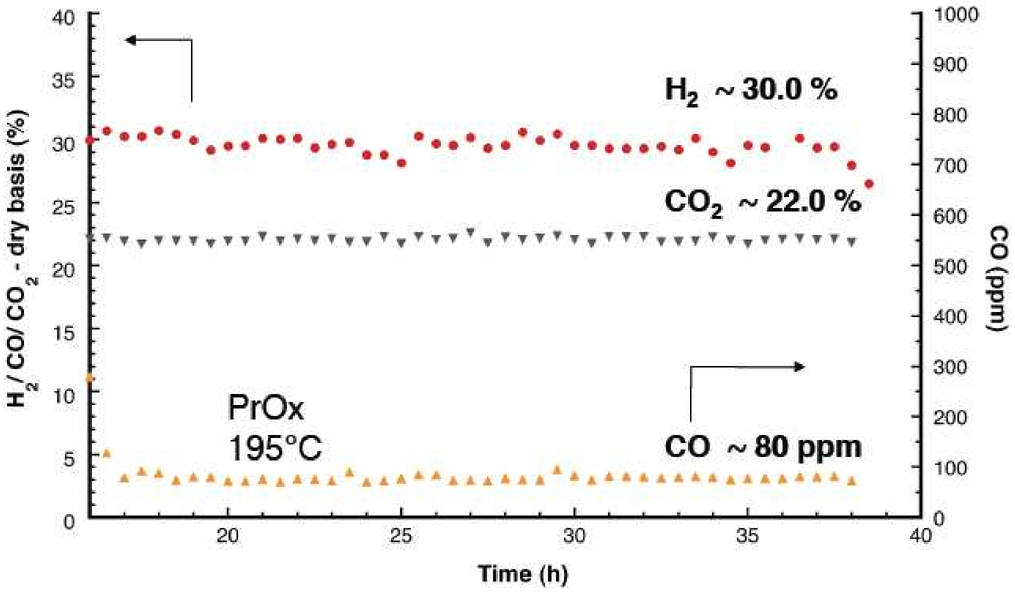

Figure 6.11: Gen II species plot

only 4 layers of the catalytic metal foams were required for the ATR reactor, the WGS and PrOx reactors required on the order of about 20 metal foams each. For measurement purposes each reactor has a tap to sample the output to the gas chromatograph (GC) for composition analysis. Figure 6.10 shows the picture of the assembled Gen II system.

Results from the operation of the Gen II system over 40 hours is shown in figure 6.11. The system successfully generated over 30% hydrogen concentration with CO levels below 80 ppm. While the operation of the Gen II system is as per design, the system is not thermally self sufficient. External heat in the form of electrical heaters is provided in each reactor for startup as well as for continuous operation. Each set of heaters in each reactor is controlled by a PID controller to maintain the temperature of the reactor as specified. A rough calculation showed that the heat input into the system was much more than the electric power expected from operating a fuel cell by the hydrogen generation by the system.

Even though the system is thermally inefficient, the Gen II system demonstrates that a fuel reformer portable system is feasible to the constructed and operated. In the next generation of the design, the individual reactors will be incorporated in a single design for thermal efficiency and self sufficiency.

6.3 Generation III

Moving from the Gen II system design of discrete reactors, the Gen III design is an attempt to integrate the reactors into one physical package. The aim as mentioned before is to further reduce heat losses from the reactors to the ambient surroundings. In the Gen III design, emphasis is on combining all the reactive regions in a single physical package. Hence instead of separate discreet physical reactors, the complete system is implemented in a single metal brick form. This is the first attempt where actual recuperation of heat from the exothermic reactors to the endothermic reactors is attempted via conduction.

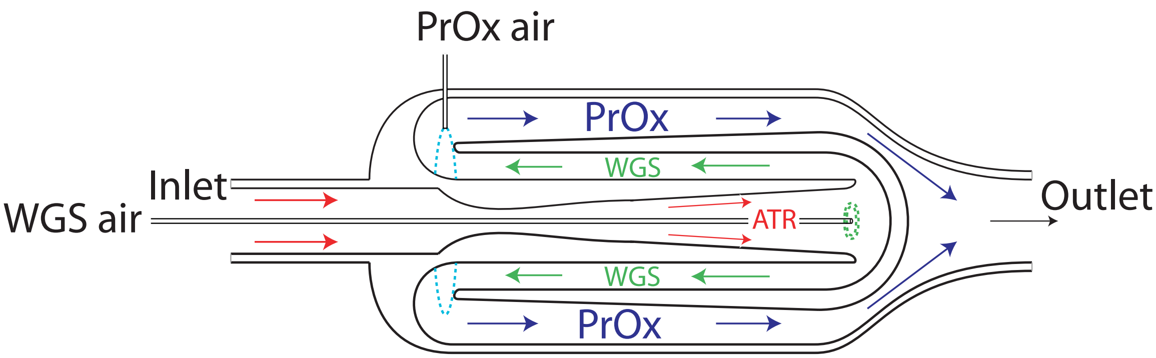

Figure 6.12: An idealized concept of an integrated fuel reformer system

6.3.1 Changes in the Generation III design

For each of the individual reactors, the earlier approach was washcoating the catalyst onto metal foams. Multiple foams are then stacked onto each other to form a single reactor. This makes the reactor packaging very bulky which leads to a higher heat loss to the ambient air due to a larger surface area of the individual reactors. To reduce the package size of the reactor, especially for the very hot ATR, the micro-channel approach was abandoned and replaced with a packed-bed reactor. The packed-bed reactor is sized as per the flow and conversion requirements of the reactor. In the Gen III design the system is designed for 1 kW_e electric output(Appendix A), so the packed-bed ATR was sized accordingly with the required amount of catalyst. Instead of washcoating the catalyst on metal foams, the ATR catalyst powder is trapped in a cylindrical ceramic channel blocked by wire meshes on both sides. This gives a very small reactor size with a good reformate conversion[35].

Heat always flows naturally from a higher temperature to a cooler temperature with the rate of flow of heat proportional to the temperature gradient. Thus, to minimize the heat loss, one has to minimize the temperature gradients. Placing a hot reactor directly exposed to the ambient air will create a high temperature gradient and hence the heat loss will be large. By placing the hottest reactor in the middle of the system and layering the other slightly cooler reactors around the hot reactor, the temperature gradients and heat losses are reduced.

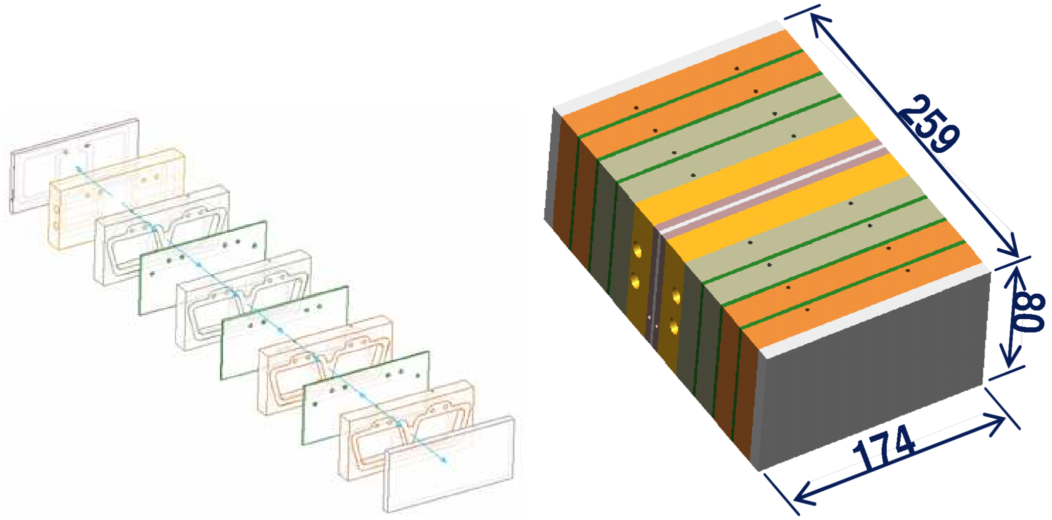

Figure 6.13: Exploded and assembled view of the Gen III concept

6.3.2 Ideal concept

The ideal concept is to place the hottest reactor in the most central location of the system and place successive reactors in a layered fashion outside of the hottest reactor. This would lead to a spherical or cylindrical design. One such cylindrical design concept is shown in figure 6.12. The ATR being the hottest reactor is placed in the core of the system. The

WGS reactor operates at a slightly lower temperature than the ATR is layered around the ATR. The initial part of the ATR can also be used as a heat exchanger along with the latter half of the WGS to preheat the feed. Finally, the PrOx reactor is further layered on top of the WGS reactor. Further insulation and heat sources might be added to the system for proper operation.

Controllability and manufacturability of such an idealized system is very difficult to achieve. To maintain the required temperature profiles in each of the reactors while providing the correct amount of heat transfer from one reactor to another is a very difficult balance to achieve. The author attempts to provide a first step into the ideal concept by use of counterflow configurations as shown in Chapter 3. The ideal concept is further complicated by startup concerns.

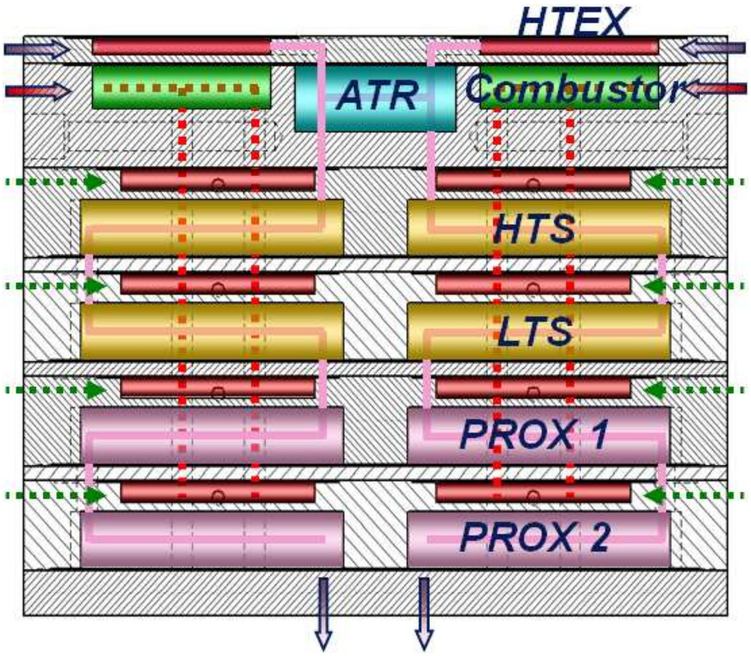

Figure 6.14: Gen III cross-sectional view

6.3.3 Description of the Generation III design

The construction of an idealized concept (figure 6.12) is also a very difficult task. To facilitate the production of a concept where heat recuperation from one reactor to another takes place, the simpler and more familiar box design with layers of metal is selected.

Figure 6.13(left) shows an exploded view of the Gen III concept. The design is made up of rectangular blocks of steel with cavities designed in some layers for the ATR, WGS and PrOx reactors. The reactors are separated by thinner sheets of steel with holes drilled in various locations and layers for providing flow passages for the flow from one reactor to the next. The picture on the right shows the complete assembled system.

Figure 6.14 shows the cross-section of shows one half of the Gen III concept. The other half is mirrored on the top such that the ATR and combustors are right in the middle of the layout. By utilizing this scheme, the hottest reactors, the ATR and the combustors do not loose heat to the ambient, but to the surrounding reactors which is the WGS reactor and the feed preheat chambers(HTEX). The other reactors are similarly layered in the system. The low temperature reactors now see the hotter reactors on one side and actually gain heat instead of loosing heat from that side. This leads to a much more thermally integrated and efficient design.

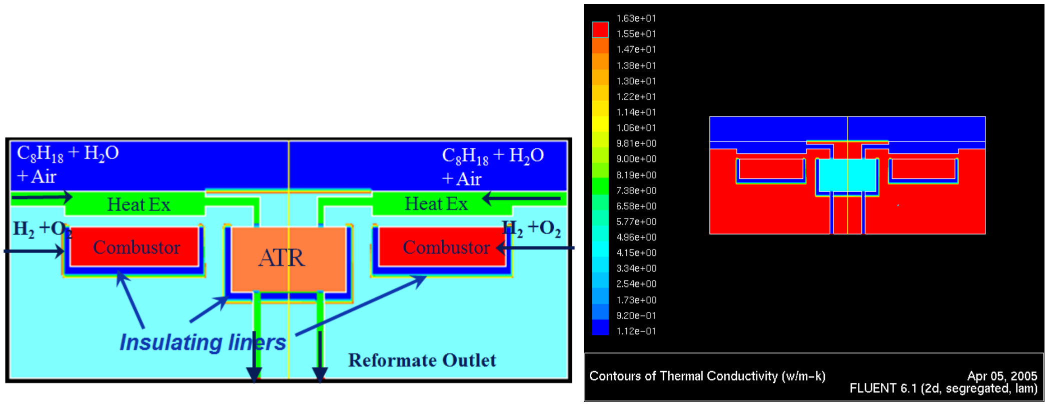

Figure 6.15: Schematic and thermal conductivity of the initial build-up on the Gen III system

6.3.4 Prototype of Generation III

During the construction of the Gen III reactor system the overall system design from the ATR to the PrOx is laid out as shown above. However it would be very difficult to make the complete system operational in a single attempt. Hence, initially, only the combustors, ATR and heat exchangers are build. The first step is to get these three components operational. The following devices will then be added one by one.

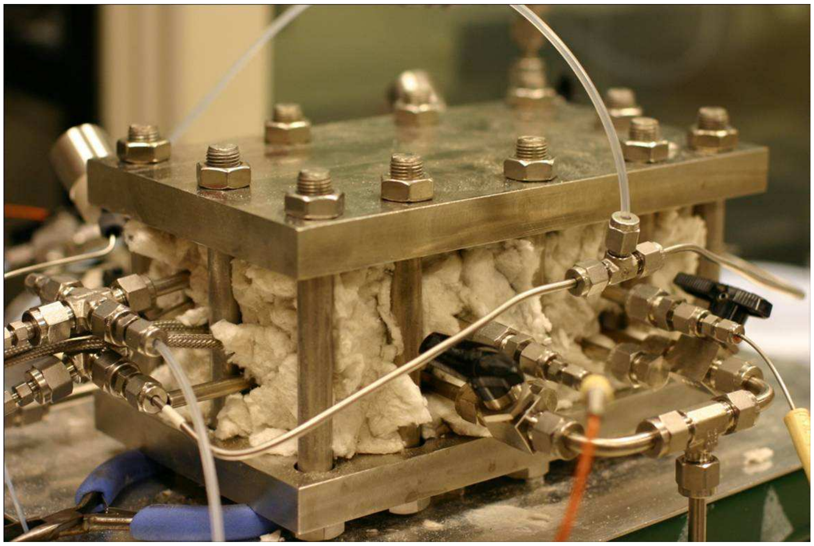

Figure 6.16: Picture of the assembled Gen III system

Figure 6.15 shows the schematic of the initial buildup of the Gen III system. The combustors in the Gen III are used to provide the heat to preheat the feed of iso-octane, water and oxygen entering into the system. The heat exchangers themselves are made bigger to provide a larger surface area for better heat transfer. Furthermore the larger size allows the feed to flow at a much slower rate in the chamber which gives a larger residence time and better preheating. The feed then flows into the ATR.

Figure 6.16 shows the assembled system with the plumbing, insulation and the complete package between two ceramic plates and then two thick steel plates. The ceramic plates are used to provide a thermal insulator on the top and bottom sides of the system while the steel plates are necessary to provide rigidity and compression to the system. The complete system is them bolted down by twelve long bolts. The sealing of the operate layers is done by graphite gaskets and compression from the bolts. Glass wool is used as external insulation on the outside of the system. By this method, the system is essentially inside insulation from all side, the ceramic plates on the top and bottom and the glass-wool on the sides. Then this complete package is caged inside the steel plates.

The system was designed not only to maintain good external insulation but also selective internal insulation. Selective insulation within the system is achieved by use of insulating foam within the reactors by lining the reactors on certain sides only. For the hydrogen combustor, the insulating foam is placed on the bottom and the sides as shown in figure 6.15. This directs the heat above to the heat exchangers and minimized heat flowing below. For the ATR, the insulating foam lining is done on the bottom and sides to prevent heat flow to the lower part. The top part is left open so that heat can flow from the heat exchangers to the ATR and vice versa.

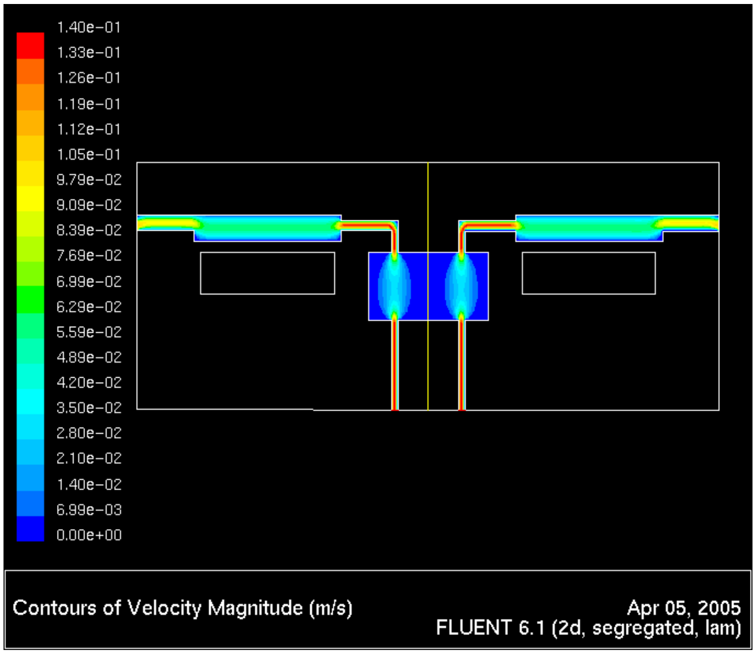

Figure 6.17: Flow characteristics in the preheat chambers and the ATR in the Gen III system

Similar to Gen II cartridge heaters were installed in the Gen III design for startup and to control the operating temperature. Even though the heaters are necessary for startup, during testing the Gen III design could self-sustain without any external heat.

6.3.5 Thermal simulations of generation III

Since the Gen III design is thermally integrated, it was important to understand the thermal characteristics and flow of heat in the design. Hence CFD based flow and thermal analysis are conducted for the Gen III system.

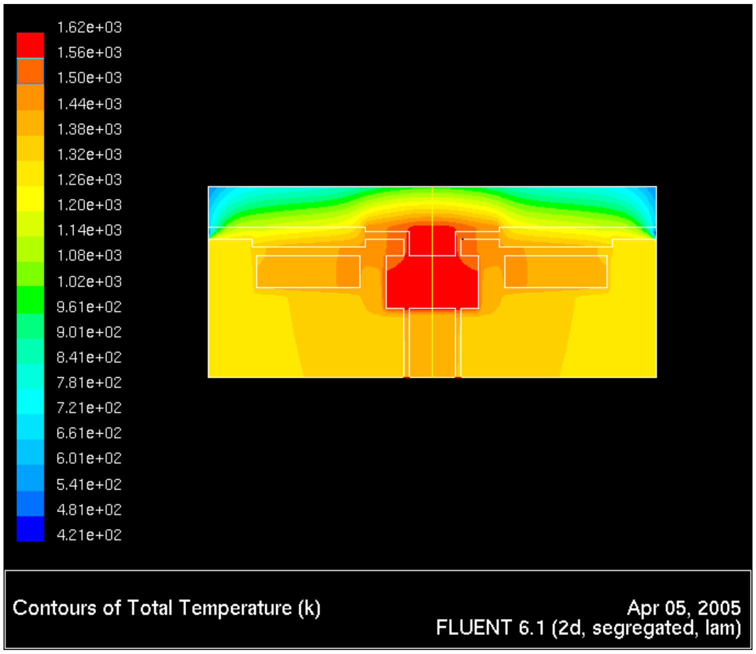

Figure 6.18: Temperature profiles in the Gen III system due to ATR heating. The ATR is used a source of heat and the heats up the rest of the system

The CFD domain is setup as shown in figure 6.15 with conductivity of the material including the insulating lining within the reactors. Since the model is symmetric, only half of the model is simulated. For simplicity, a 2D simulation in undertaken instead of a full 3D. The flow boundary conditions are given in Appendix A for a 1 kW_e system.

Figure 6.17 show the results for the flow simulation. The flow appears to be channelized within the ATR and may cause some mixing issues. However, in the actual setup, within the ATR a ceramic block is placed with a single channel. Hence channelization would not be a problem. Note that this flow simulations did not contain the ceramic block used in the ATR during testing.

Figure 6.18 shows the results from the simulation of the Gen III initial setup. In this simulation, the ATR is defined as a heat source to see how heat would spread in the system. For the results, we can say that the insulating liners within the ATR reactor are able to direct heat to the heat exchanger above rather than let it flow below and away from the heat exchangers.

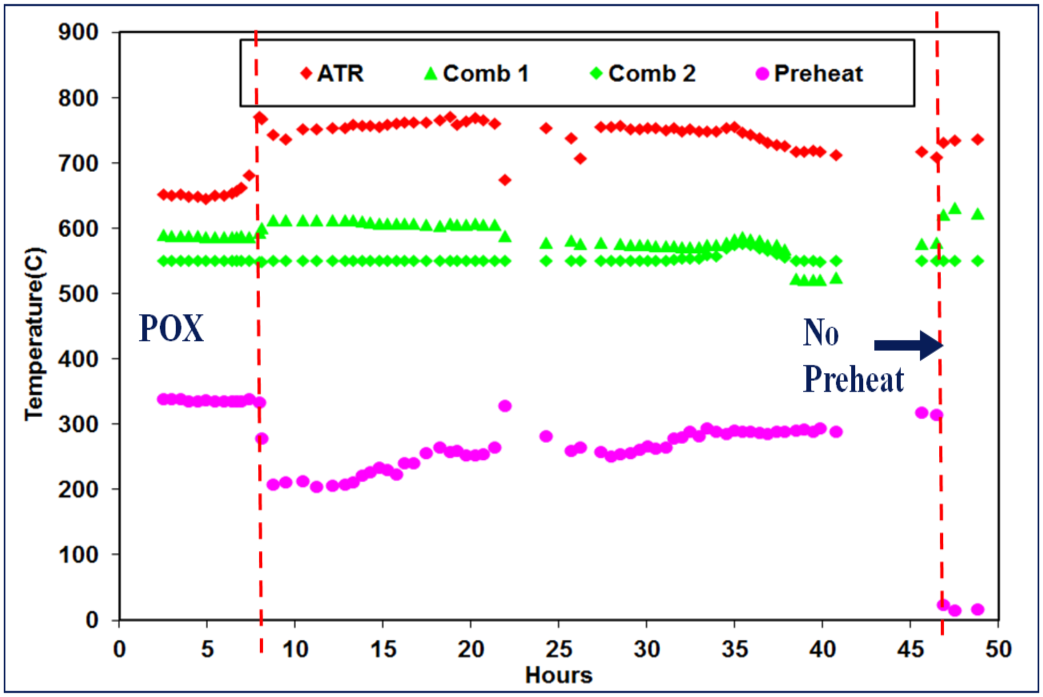

Figure 6.19: Gen III temperature plot

6.3.6 System operation and experimental results

The system was run continuously for 50 hours with the feed rates as shown in appendix A which corresponds to a system power generations of 1 kW_e. Figure 6.19 shows the temperatures, pressure drop and heat input(preheat) in the system over the 50 hours of operation. For the first 10 hours or so the water was mistakenly not turned on. Hence the ATR operated as a partial oxidation reactor instead of auto-thermal reforming. For the last few hours of operation, the preheat was turned off to see if the system would operate without any external heat input. As seen in figure 6.19, the system continued to operate with no drop in temperature. The temperatures within the ATR and combustors remain stable.

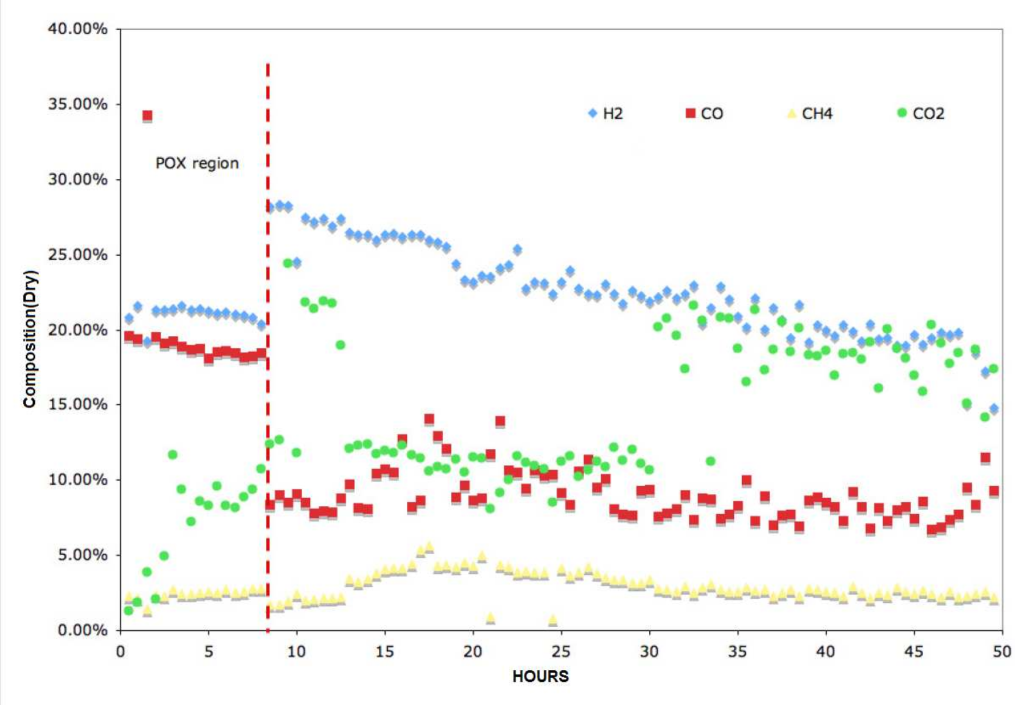

Figure 6.20: Gen III species plot

Figure 6.20 show the results for the species from the system. The plot shows the mole fractions for the various species without the mole fraction for water. Hence the totals do not add up to a hundred. Again for the initial 10 hours, the water input to the system is turned off resulting in lower percentage of hydrogen as the system is operating in partial oxidation mode. As soon as the water is turned on, the hydrogen percentage jumps to about 30 %. The system performance does degrade a little over time with hydrogen production lowering to about 20 % at 50 hours. However even when the preheat was turned off the system continued to operate and generate hydrogen.

The University of Michigan fuel processor team continued the above work to add further stages in the Generation III design and built an updated system[68]. It includes the WGS and PrOx reactors and is able to sustain itself thermally and chemically over long periods of time with gasoline as a fuel. The hydrogen flow output from the design is 4.1 L/min which corresponds to 732W$_{th}$. The hydrogen efficiency for the conversion is 0.7 for the system and the thermal efficiency is calculated to be 0.51. The system was tested for over 100 hours and found to be tolerant to sulphur in the fuel.

Chapter 7

Summary and Recommendation for Future Work

With PEM fuel cells showing great promise as a future portable power sources, the emphasis on hydrogen production by fuel processing has increased. The need for miniaturization of current reactors to portable levels is also evident by the nature of the applications served by the fuel cell/fuel processor systems.

In this dissertation, an attempt was made in the development of thermally efficient and compact fuel processor systems. Work including the development of a basic heat recovery models to the development of working prototypes was undertaken. The following paragraphs give the overall summary for the work done.

Counterflow reactor A counterflow heat exchanger model for heat recovery with a catalytic PrOx reaction channel was developed. Parametric studies were undertaken to investigate the effect of various parameters on the system. It was demonstrated that the counterflow control stream could be used to control the operating conditions of the reactor system. Since heat is recovered from the exothermic reactor to preheat the cold reactant feed, the heat recuperation may sacrifice the conversion efficiency in the reactor. The proposed model provides a convenient tool to efficiently identify the optimal conditions for initial system design.

Silicon micro-reactor CFD flow modeling of a silicon substrate based micro-reactor was performed. A custom mesh to capture the boundary layer effects was constructed. Flow characteristics of the micro-reactor were modelled using FLUENT. Effect of the micro-reactor features on the flow mixing was studied by closing off alternate inlets and this effect was found to be negligible. The flow was found to redistribute itself in less than two cell lengths.

Thermal simulations of the micro-reactor was done to predict the temperatures in the silicon micro-reactor when the complete setup is packaged in a bulky contraption. Comparison to experimental and validation of the thermal model packaging was done in Chapter 5.

Comparison of the micro-reactor was done with a packed-bed system. The micro-channel system is found to be comparable to the packed-bed system since mass transfer is not a limitation in both systems. The micro-reactors also have a much smaller pressure drop and have distinct advantages such as flexibility of reactor design and integration of structural and functional features. Scale up of the design by increasing the number of micro-reactors by stacking was discussed. The scale-up method can also be used for fabricating a crossflow heat-exchanger configuration using the same design. The use of such a wall-coated micro-channel reactor system provides advantages such as customizable reactor designs, integration of structural and functional features, low pressure drop and, possibly, efficient heat management which are very difficult in conventional packed-bed reactors.

Silicon micro-reactor with and integrate platinum heater The micro-channel reactor was integrated with a platinum heater which was deposited on the underside of the silicon substrate. Thermal CFD simulations of the setup were done to predict the hot spots in the design and the temperature distribution. The thermal model was validated by use of thermocouple data over different thermal dissipation rates from the platinum heater. The model is able to predict the temperature distribution in the micro-reactor and its surroundings.

A 1-D reactive model for the PrOx reaction was implemented in POLYMATH. The reactive model was able to predict the conversion of the micro-reactor to a very good degree. The measured data was consistent with the simulations results. Integrating a heater with the micro-reactor makes a much smaller package with better thermal characteristics.

Design and prototyping Three generations of fuel processing systems were designed and prototyped. After a first prototype(Gen I) that did not work very well, a complete micro-channel based working fuel processor system (Gen II) was constructed and run over extended times. The conversion or the reformate into hydrogen was satisfactory at about 70%. Using a micro-channel design has to be done with much care, since the micro-channel necessitates a much bigger physical design which which is prone to high heat losses to the environment. This generation of the system used discreet packaged reactors with each having their own external heat supply.

As a next step a thermally integrated(Gen III) system was designed. The foam based reactor approach was replaced with packed-bed ATR design. The initial part of the system with only the integrated combustors/heat exchangers and the ATR was constructed. The system gave good conversion performance and was able to continue operation even when external heat supply was removed. Using packed bed reactors sized to the design flow requirements instead of using small foam based reactors decreases the package size of the reactors. This makes the reactors much more thermally compact and efficient.

7.1 Directions for Future Work

In this dissertation we have build and used simplistic models as well as full 3D CFD models to study and built reactors for fuel processing as well full fuel processing systems. Much is yet to be learned and accomplished and the following are some recommendations.

The counterflow model as a simplistic model works very well to predict the effect of varying different parameters. Effect of only a limited number of parameters were studied. This can be expanded to include numerous other parameters such as construction material, wall thickness, variable catalyst loading, etc. Expansion to multiple reactors chained together as shown in figure 3.14 can also be done. However this model cannot predict the heat transfer and temperatures in thermal integrated design such as the Gen III design. For the latter, 2D or 3D CFD simulations are still required to get accurate numbers. Extension of the counterflow model to the other reactors other than PrOx such as the ATR and WGS can also be undertaken.

Until now, all micro-reactor development have been done in highly controlled environments. The temperature of these micro-reactors has been controlled by the use of external heaters. While this system works, in practice any external heat input implies a loss of the overall system efficiency. Therefore, it is necessary to design micro-reactors with minimal use of external heat inputs. This requires extensive parametric studies with various system dimensions and configurations, which can be substantially facilitated by developing simulation tools with the required fidelity.

In Chapter 4 and Chapter 5, while a silicon based micro-channel reactors has be modelled and demonstrated, the heat losses from such a high aspect ratio physical package are excessive. Effects of scaling-up via multiple parallel reactors the system to reduce the thermal losses can be studied via modeling. Comparison to a packed-bed reactor as the system is scaled-up should be kept in mind since in the Gen III design there is merit in replacing the micro-channel based ATR with a packed-bed reactor.

Chapter 6 demonstrated a working fuel processor system and the initial makings of a thermally integrated fuel processor with only the ATR and the combustors. This should obviously be carried forward to included the WGS and PrOx reactors to complete the system.

Fuel reforming remains one of the desirable techniques to generate hydrogen for portable devices. However, the Department of Energy's strategy has shifted towards developing portable fuel reformers based on abundant and renewable fuel sources[69] such as natural gas and biomass. With the lighter hydrocarbons, not only do we skip the big components of WGS and PrOx since CO cleanup is not required, but also the operating temperatures are much lower at below 200°C. An iso-octane fuel reformer would need to operate at over 700°C making the design big and heavy.

Appendix A

System datasheet for a 400W fuel processor

System Power (Hydrogen based) - 400 W

Hydrogen feed required for fuel cell 10.66 gm-mol H_2/hour

(Calculated from DOE Fuel Cell handbook - Page 8-2)

(www.seca.doe.gov/pubs/4-fuelcell.pdf)

(Data from Perry's chemical engineers' handbook[57])

Fuel Modeled Gasoline - (Iso-octane + 300 ppm Sulphur)

Component wise data sheet

Desulpherizer

Number of Devices - 1

Operating Temperature - Room Temperature

Inlet Flow Rates

Modeled gasoline — 0.6406 gm-mol C_8H_{18}/Hr

Inlet Sulphur Concentration 300 ppm

Outlet Sulphur Concentration 20 ppb = 0.02 ppm (Worst Case 0.3 ppm)

Auto-thermal reformer(ATR)

Number of Devices - 1

Inlet Temperature 350–400 $^\circ\mathrm{C}$

Inlet Flow Rates and composition

C_8H_{18} — 0.0209 x 12.8665 = 0.6406 gm-mol C_8H_{18}/Hr (using Carbon balance)
H_2O — 0.3344 x 12.8665 = 10.2496 gm-mol H_2O/Hr (using H_2O/C = 2.0)
Air — 0.0836 (O_2+3.76 N_2) x 12.8665 = 2.5624 gm-mol (O_2+3.76 N_2) /Hr (O_2/C = 0.5)

Exit Temperature 550±50 $^\circ\mathrm{C}$

Exit Composition (Wet Volume Basis) Equilibrium Based at 700 $^\circ\mathrm{C}$

H_2 — 0.2788
N_2 — 0.3139
CO — 0.0690
CH_4 — 0.002
CO_2 — 0.0962
H_2O — 0.2400

Total mole flow = 30.65 gm-mol/Hr (Remains unchanged, WGS does not change number of moles, in PrOx $O_2$is consumed.)

Water gas shift reactor

(The reaction $CO+H_2O \rightarrow CO_2+H_2$ is assumed to go to completion, leaving $\sim$500 ppm CO)

Number of Devices 2 in serial configuration

Inlet Temperature 400 $^\circ\mathrm{C}$

Inlet Composition (Wet Volume Basis)

H_2 — 0.2788
N_2 — 0.3139
CO — 0.0690
CH_4 — 0.002
CO_2 — 0.0962
H_2O — 0.2400

Exit Temperature 250 °C

Exit Composition (Wet Volume Basis)
H_2 — 0.3478
N_2 — 0.3139
CO — $\sim$500 ppm
CH_4 — 0.002
CO_2 — 0.1652
H_2O — 0.1700

Preferential oxidation reactor

(Here the changes in concentrations other than CO are neglected. The only change made is that the CO concentration goes down from $\sim$500 ppm to $\sim$10 ppm)

Number of Devices 2 in serial configuration

Inlet Temperature 220 °C

Inlet Composition (Wet Volume Basis)
H_2 — 0.3478
N_2 — 0.3139
CO — 500 ppm
CH_4 — 0.002
CO_2 — 0.1652
H_2O — 0.1700

Additional air is also introduced into the PrOX reactor. Using selectivity = 0.5 Moles of O_2needed = 2 x 500 ppm x 30.65 /Hr /2(atoms/molecule of O_2) = 0.015 gm-mol O_2/Hr

Exit Temperature 180 °C

Exit Composition (Wet Volume Basis)

H_2 — 0.3478

N_2 — 0.3139

CO — 10 ppm

CH_4 — 0.002

CO_2 — 0.1652

H_2O — 0.1700

Appendix B

PrOx implementation for Counter-Flow Reactor model

Nomenclature

Reactor channel bulk temperature	$T_R(x)$	[K]
Length of channel	L	[cm]
Flow rate of CO species	F_{CO}	[moles/sec]
Weight of catalyst	W_{TOT}	[gm]
CO generation per gm cat.	r_{CO}	[moles/sec-gm of cat.]
Kinetic rate TOF	$r_{CO\|TOF}$	[sec^{-1}]
Active catalyst percentage	θ_{Pt}	[gm-Pt/gm-cat]
Catalyst dispersion	χ_{Pt}	[ ]
Molecular weight of active catalyst	MW_{Pt}	[gm/mole]
Inlet flow rate	V_0	[cm^3/sec]
Temperature for V_0	T_0	[K]
Pre-exponential factor	k_{CO}	[1/sec-kPa$^{(\alpha+\beta)}$ for $r_{CO\|TOF}$]
Activation Energy	Ea	[ergs/mol]
Gas constant	R	[=8.314e7 ergs/mol-K]
CO Partial pressure	P_{CO}	[dynes/cm^2], [kPa for $r_{CO\|TOF}$]
O_2 Partial pressure	P_{O_2}	[dynes/cm^2], [kPa for $r_{CO\|TOF}$]

Concentration of species i	C_i	[moles/cm^3]
Selectivity	s	[ ]

Superscripts

Initial value, at $x = 0$ i

Assumptions

The total number of moles that flow in the channel do not change. This is reasonable for the PrOx reaction since it operates in a very dilute range and any effects change in total number of moles due to the reaction is very small. This would not be applicable in the WGS reaction and the equations would have to be changed accordingly.

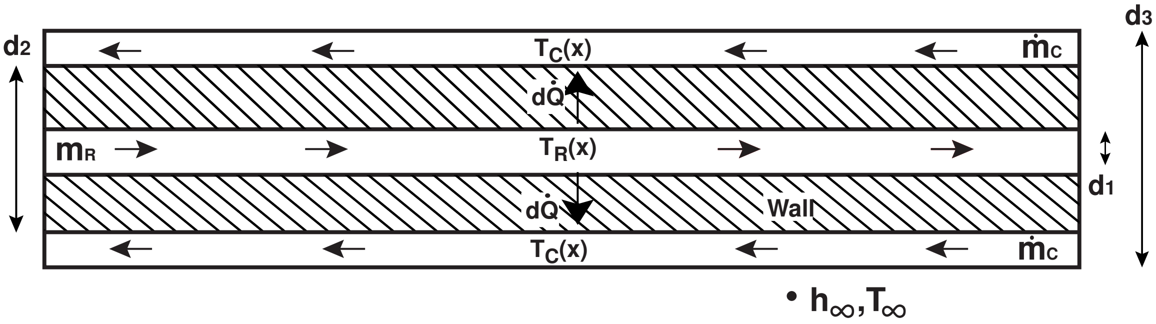

Figure B.1: Model configuration: Concentric counterflow reactor

Equations

$$\frac{dF_{CO}(x)}{dW} = r_{CO} \quad \text{[moles/sec-gm of cat.]} \tag{B.1}$$

$$r_{CO} = \frac{r_{CO|TOF} \cdot \theta_{Pt} \cdot \chi_{Pt}}{MW_{Pt}} \quad \text{[moles/sec-gm of cat.]} \tag{B.2}$$

$$-r_{CO|TOF} = k_{CO} \cdot e^{\frac{-Ea}{RT}} \cdot P_{CO}^{\alpha} \cdot P_{O_2}^{\beta} \quad [\text{sec}^{-1}] \tag{B.3}$$

Also flow rate $F_{CO}(x)$ can be written as a product of the concentration $C_{CO}(x)$ and the flow rate $V(x)$. The flow rate $V(x)$ is related to the inlet flow rate and temperature by …

$$\begin{aligned} V(x) &= \frac{V_0}{T_0} \cdot T_R(x) && \text{(B.4)} \\ \Rightarrow F_{CO}(x) &= C_{CO}(x) \cdot V(x) = C_{CO} \cdot \frac{V_0}{T_0} \cdot T_R(x) && \text{(B.5)} \end{aligned}$$

Also

$$\begin{aligned} W(x) &= W_{TOT} \cdot \frac{x}{L} && \text{(B.6)} \\ \Rightarrow \quad dW &= \frac{W_{TOT}}{L} \cdot dx && \text{(B.7)} \\ \frac{dF_{CO}(x)}{dW} &= \left[\frac{V_0}{T_0} \frac{L}{W_{TOT}} \right] \cdot \frac{d(C_{CO}(x) T_R(x))}{dx} && \text{(B.8)} \end{aligned}$$

Putting it all together.

$$\frac{d[C_{CO}(x) T_R(x)]}{dx} = - \left[\frac{T_0}{V_0} \frac{W_{TOT}}{L} \right] \cdot \frac{k_{CO} \cdot \theta_{Pt} \cdot \chi_{Pt} \cdot [R \cdot T_R(x)]^{\alpha+\beta}}{MW_{Pt}} e^{\left(\frac{-Ea}{R \cdot T_R(x)} \right)} \cdot C_{CO}^{\alpha} \cdot C_{O_2}^{\beta} \tag{B.9}$$

which can also be written as …

$$\frac{d[C_{CO}(x) T_R(x)]}{dx} = - \left[\frac{T_0}{V_0} \frac{W_{TOT}}{L} \right] \cdot \frac{k_{CO} \cdot \theta_{Pt} \cdot \chi_{Pt} \cdot}{MW_{Pt}} e^{\left(\frac{-Ea}{R \cdot T_R(x)} \right)} \cdot P_{CO}^{\alpha} \cdot P_{O_2}^{\beta} \tag{B.10}$$

where the partial pressures P_{CO} and P_{O_2} are given in kPa.[ref Kim Lim]

Concentration Relations

$$\begin{aligned} P_{CO} V &= n_{CO} R T_R && \text{(B.11)} \\ C_{CO} = \frac{n_{CO}}{V} &= \frac{P_{CO}}{R T_R} = \frac{X_{CO} P}{R T_R} && \text{(B.12)} \\ C_{CO}^{i} &= \frac{X_{CO}^{i} P}{R T_R^{i}} && \text{(B.13)} \end{aligned}$$

PrOx Reaction

Defining selectivity . . .

$$s = \frac{\text{Oxygen consumed by CO oxidation}}{\text{total oxygen used}} \tag{B.14}$$

The Preferential oxidation of CO in a hydrogen environment is characterized by the following two reactions. . .

$$CO + \frac{1}{2}\,O_2 \quad \longrightarrow \quad CO_2 \tag{B.15}$$

$$\left(\frac{1}{s} - 1\right)(H_2 + \frac{1}{2}\,O_2 \quad \longrightarrow \quad H_2O) \tag{B.16}$$

For every mole of CO that reacts $\frac{1}{2s}$ mole of $\mathrm{O_2}$ reacts. Total number of moles that flow are given by . . .

$$[F^i_{CO} - F_{CO}(x)] = \frac{1}{2s}[F^i_{O_2} - F_{O_2}(x)] \tag{B.17}$$

Hence the following holds true.

$$[C^i_{CO}T^i_R - C_{CO}T_R(x)] = \frac{1}{2s}[C^i_{O_2}T^i_R - C_{O_2}T_R(x)] \tag{B.18}$$

or

$$C_{O_2} = \frac{T^i_R}{T_R}(C^i_{O_2} - 2s\,C^i_{CO}) + 2s\,C_{CO} \tag{B.19}$$

Conventional derivation

From Kuo[48] . . .

$$\frac{\partial C_A}{\partial t} + \nabla \cdot C_A v = \nabla C D_{AB} \, \nabla X_A + \dot{\Omega}_A \tag{B.20}$$

Under steady state conditions with no diffusion, the equation reduces to . . .

$$\frac{\partial}{\partial x}(C_A v) = \dot{\Omega}_A \tag{B.21}$$

where

$$\dot{\Omega}_A = r_{A|TOF} \times \left(\frac{W_{TOT}}{LA_C} \right) \times \frac{\theta \cdot \chi}{MW} \tag{B.22}$$

$$v = \frac{V}{A_C} = \frac{V_0}{A_C} \frac{T_R}{T_0} \tag{B.23}$$

Thus

$$\frac{\partial}{\partial x} \left(C_A \frac{V_0}{A_C} \frac{T_R}{T_0} \right) = r_{A|TOF} \frac{W_{TOT}}{LA_C} \frac{\theta \cdot \chi}{MW} \tag{B.24}$$

Linking heat generation with Heat of Reaction

$$-\dot{m}_R C_{PR} \frac{dT_R}{dx} - h_1 \pi d_1 (T_R - T_W) + \frac{\dot{q}}{\Delta x} = 0 \left[\frac{\text{ergs}}{\text{cm} - \text{s}} \right] \tag{B.25}$$

$$\Delta F_{CO} = \frac{\partial [C_{CO} V]}{\partial x} \Delta x \tag{B.26}$$

$$\dot{q} = HOR \times \Delta F_{CO} \tag{B.27}$$

$$\frac{dT_R}{dx} = -\frac{\pi h_1 d_1}{\dot{m}_R C_{PR}} (T_R - T_W) + \frac{HOR}{\dot{m}_R C_{PR}} \cdot \frac{V_0}{T_0} \cdot \frac{d[C_{CO} T_R]}{dx} \tag{B.28}$$

Appendix C

Matlab code for the counter flow model

```matlab
%% Module for counter flow model with PrOx implementation
% Amit Dhingra
% Incorporating the Kim Lim kinetics
% In dimensional form (CGI system)

%% INIT
clear all;
close all;
format short g;
disp('Beginning')
run_number = 0; % used to modify ergs——> Joules only once

%% DATA ENTRY

%%     Inlet mass fractions for reactor stream and catalyst properties
% Define input volume percentages
% index [CO O2 H2 Ar]
XXi=[0.01 0.01 0.60 0.38]; % Initial mole fractions
Wt=[28 32 2 40]; % Molar weights
T0 = 300; % Temperature at which V0 was measure, e.g. SLPM [K]
Wtot = 0.8059; % [gm] of catalyst
```

```
thetaPt = 0.02; % [fraction] mass fraction of Pt in catalyst
chiPt = 0.3; % [] Dispersion of Pt
MWPt = 195; % [gm/mol] Molecular weight of Pt
s = 0.5; % selectivity

%%     Single step reaction data – PROX kinectics – Kim Lim
kCO=1.4e8;
HORCO=–280000e7; % [ergs/mol]
HORH2=–240000e7; % [ergs/mol]
Ea=78000e7; % [ergs/mol]
Rgasconst=8.314e7; % [ergs/mol–K]
a=–0.51; %CO2 coeffcient
b=+0.76; %O2 coefficient

%%     Geometry and constrction material
d1=0.56; %Reactor channel diameter [cm]
d2=1.29; %Inner coolent channel diameter [cm]
d3=2.89; %Outer coolent channel diameter [cm]
L=4; %Length of the reactor [cm]
kW=12e5; %Thermal conductivity of the wall [ergs/s–cm–K]

AR=pi/4*d1*d1; % Cross–section area of reactor channel [cmˆ2]


%%     Reactor channel
mR=0.00018651e2;  % mass flow rate in reactor channel [gm/s]
CPR=1535e4; % specific hear in the reactor channel [ergs/gm–K]
NuR=4.0; % Nussleft number of the reactor channel, diameter based []
TRIN = 198+273; % Inlet temperature of the reactor channel [K]
kR = 0.10783e5; % [ergs/sec–cm–K]
% hR is calculated below

%%     Coolant channel
```

```
mC=7.32e-3; %[gm/sec]
CPC=4200e4; %[ergs/gm-K]
TCIN=300; % [K]
kC=0.6e5; %[ergs/sec-cm-K]
NuC=7.54; %

%%     Ambient Conditions
TINF=300;  %[K]
hINF=10e3; %[ergs/sec-cm2-K] % Recalculate
pINF=1.0135e5 * 1e1; % [dynes/cm2] Make sure you convert Pressure to ...
    kPa in rCO|TOF

%% END DATA entry, BEGIN data processing

%% Beginning big loop for parameteric study
%%     Setting varied variable limits and steps
var_desc = 'Reactor channel mass flow rate [gm/sec]';
var_name = 'mR';
var_base_value = eval(var_name);
var_LB = 0.00009e2;
var_UB = 0.00036e2;
no_steps = 400;
var_space = linspace(var_LB, var_UB, no_steps);
disp('Parameteric Study');
fprintf('For %s\n', var_name)
disp('    LB     UB  No of Steps')
disp([var_LB, var_UB, no_steps])
for k = 1:no_steps
%%     Setting  varied variable
    assignin('base',var_name,var_space(k))
    fprintf('%i of %i : %s is %f\n',k,no_steps,var_name,eval(var_name));

```

```
%%     Normalizing the mole fractions and calulating initial ...
   concentrations
        if abs(sum(XXi))>1.02; warning('Mole fractions do not add up ...
           to 1, Normalizing...'); end;
        XXi=XXi/sum(XXi);
        %Calculating the mass fractions and initial concentrations
        YYi = (XXi.*Wt)/(XXi*Wt');
        CCi = XXi.*pINF/Rgasconst/TRIN; %[moles/cm^3]

%%     Calculated Values. Do not modify directly
        rhoR0 = pINF*XXi*Wt'/Rgasconst/T0; % [gm/cc]
        rhoRIN = pINF*XXi*Wt'/Rgasconst/TRIN; % [gm/cc]
        V0 = mR/rhoR0; % [cc/sec]
    VRIN = mR/rhoRIN; % [cc/sec]
    v_RIN = mR/rhoRIN/AR; % velocity at reactor entrace [cm/sec]
        WHSV = V0/Wtot*3600; % [cc/hour /gm of cat]
        C1 = T0/V0*Wtot/L;
        C2 = kCO*thetaPt*chiPt/MWPt;
        HOR = HORCO + (1/s-1) * HORH2; %[ergs/mol]

        hR=kR*NuR/d1; %[ergs/(sec-cm^2-K)]
%       hC=kC*NuC/d2; %[ergs/(sec-cm^2-K)]
%       Rthermal=(1/pi/NuR/kR +log(d2/d1)/2/pi/kW + 1/NuC/kC/pi); ...
   %[sec-cm-K/ergs]
    h1=hR;

        % End data manipulation, Begin solving.

%%     DAE definitions and Solution

    % Variables defination
    % y(1) - T_W
    % y(2) - T_Wdot
```

```
        % y(3) - T_R
        % y(4) - T_C
        % y(5) - T_R * C_CO
        % y(6) - T_R * C_O2

        %Solver Initialization and Options, then solution
    options = bvpset('Stats','off','RelTol',1e-5, 'AbsTol',[1e-5 ...
       1e-5 1e-5 1e-5 1e-5 1e-5]);
        if exist('sol') == 1;
            solinit = sol;
        else
            solinit = ...
                bvpinit(linspace(0,L,201),[(d1*TRIN+d2*TCIN)/(d1+d2) ...
                0 0.8*TRIN TCIN TRIN*CCi(1) TRIN*CCi(2)]);
        end;
    sol = bvp4c(@eqn_s,@eqn_bc,solinit,options,C1,C2,Ea,Rgasconst, ...
       a,b,s,HOR,V0,T0,d1,d2,d3,TRIN,TCIN,CCi,h1,kW,mR,CPR,mC,CPC,hINF,TINF);

        solk(k) = sol; % Copy sol to a solk variable for post_sens.m

%%      Calculating efficiency terms
        lastnode = length(sol.x);
        Isotherm(k) = sqrt(sum((sol.y(3,:)-TRIN).^2));
        % End Isothermality Block

        Qgen(k)  = (sol.y(5,1) - sol.y(5,lastnode))*V0/T0*(-HOR);
        Qtran(k) = mR*CPR*(sol.y(3,1) - sol.y(3,lastnode)) + Qgen(k);
        Qgain(k) = mC*CPC*(sol.y(4,1) - sol.y(4,lastnode));
        Qloss(k) = Qtran(k) - Qgain(k);
        Qloss2(k) = trapz(sol.x,(sol.y(4,:)-TINF))*pi*hINF*d3;
        effic(k) = Qgain(k)/Qtran(k);
        conv(k) = 1-(sol.y(5,lastnode)/TRIN/CCi(1)); % Conversion ...
           and Converting y(2) = C_CO*T_R back into XX
```

```
        [Qgen(k) Qtran(k) Qgain(k) Qloss(k) Qloss2(k) effic(k) ...
           conv(k)]; % There is a semicolon here

        % Calculating the reaction rate length
        cut_off = 1e-8;
        PCO = sol.y(5,:)*Rgasconst; % [dynes/cm2]
        PO2 = sol.y(6,:)*Rgasconst; % [dynes/cm2]
        PCO = PCO/10/1e3; % [kPa]
        PO2 = PO2/10/1e3; % [kPa]
        dCCOTRdx = C1*C2*exp(-Ea/Rgasconst./sol.y(3,:)) ...
           .*PCO.^a.*PO2.^b/TRIN; %This is now positive
        reac_index=1; max_index = length(dCCOTRdx);
        while ((dCCOTRdx(reac_index)>=cut_off) && ...
           (reac_index<max_index) )
            reac_index=reac_index+1;
        end;
        reac_length(k)=sol.x(reac_index);

end; %for k, the big loop for parameteric study ENDS HERE

%% Post processing.
close all
reac_length2=supsmu(var_space, reac_length); %Fitting the data
if min(reac_length2)<0; warning('Minimum of reac__length2 < 0'); end;
reac_length2 = reac_length2 + eps; % Make sure any term in ...
   reac_length2 is not zero for log later on.
dlmwrite('ecl.dat', [var_space' effic' conv' ...
   reac_length2'],'precision','%20.10f')

%% Sensitivity Analysis - Uses center differencing
for k = 1:no_steps-1
    xvar(k) = (var_space(k)+var_space(k+1))/2;
```

```
    Isotherm_sens(k)  = (log(Isotherm(k+1))-log(Isotherm(k))) / ...
       (log(var_space(k+1))-log(var_space(k)));
    Qtran_sens(k)  = (log(Qtran(k+1))-log(Qtran(k))) / ...
       (log(var_space(k+1))-log(var_space(k)));
    Qgain_sens(k)  = (log(Qgain(k+1))-log(Qgain(k))) / ...
       (log(var_space(k+1))-log(var_space(k)));
    Qloss_sens(k)  = (log(Qloss(k+1))-log(Qloss(k))) / ...
       (log(var_space(k+1))-log(var_space(k)));
    effic_sens(k)  = (log(effic(k+1))-log(effic(k))) / ...
       (log(var_space(k+1))-log(var_space(k)));
    conv_sens(k)  = (log(conv(k+1))-log(conv(k))) / ...
       (log(var_space(k+1))-log(var_space(k)));
    reac_length2_sens(k)  = ...
       (log(reac_length2(k+1))-log(reac_length2(k))) / ...
       (log(var_space(k+1))-log(var_space(k)));
end;

dlmwrite('ecl_sens.dat', [xvar' effic_sens' conv_sens' ...
   reac_length2_sens'], 'precision','%20.10f')

%% Plot the main plot
close all
[ax, hlines] = plotyyy(var_space', effic', var_space', reac_length2, ...
   var_space', conv', {'Efficiency' 'Reactive Length' ...
   'Conversion'}) ;
legend(hlines, 'Efficiency', 'Reactive Length', 'Conversion')
%set(hlines(1), 'Color', [1 0 0], 'LineWidth', 2.0)
%set(hlines(2), 'Color', [0 0 1], 'LineWidth', 2.0, 'LineStyle', '-.')
%set(hlines(3), 'Color', [0 1 0], 'LineWidth', 2.0, 'LineStyle', '--')

axes(ax(1));
xlim_t = get(ax(1), 'xlim');
axis([xlim_t 0 1]);
```

```

axes(ax(2));
xlim_t = get(ax(2), 'xlim');
axis([xlim_t 0 5]);

axes(ax(3));
xlim_t = get(ax(3), 'xlim');
axis([xlim_t 0 1]);

%% Plot the sensitivity plot
[ax, hlines] = plotyyy(xvar', effic_sens', xvar', reac_length2_sens, ...
   xvar', conv_sens, {'Sens Efficient' 'Sens Reac Len' 'Sens Conv'});
legend(hlines, 'Sens Efficiency', 'Sens Reactive Length', 'Sens ...
   Conversion')
%set(hlines(1), 'Color', [1 0 0], 'LineWidth', 2.0)
%set(hlines(2), 'Color', [0 0 1], 'LineWidth', 2.0, 'LineStyle', '−.')
%set(hlines(3), 'Color', [0 1 0], 'LineWidth', 2.0, 'LineStyle', '−−')

axes(ax(1));
xlim_t = get(ax(1), 'xlim');
axis([xlim_t −2 2]);
%set(ax(1), 'XTickMode', 'Auto')

axes(ax(2));
xlim_t = get(ax(2), 'xlim');
axis([xlim_t −1 1]);


axes(ax(3));
xlim_t = get(ax(3), 'xlim');
axis([xlim_t −2 2]);

%% Defining factor and Modifying var_space
```

```
mod_fact = 1; %Changes the display value in the x–axis
if run_number == 0
    run_number = 1;
    var_space = var_space /mod_fact;
    xvar = xvar /mod_fact;
    var_LB = var_LB/mod_fact;
    var_UB = var_UB/mod_fact;

    Qtran = Qtran/1e7;
    Qgain = Qgain/1e7;
    Qloss = Qloss/1e7;
end;

%% Plotting sensitivity of effic, conv and reac_length

disp('The End')
```

```
function dydx = eqn_s(x,y,C1,C2,Ea,Rgasconst,a,b,s,HOR,V0,T0, ...
   d1,d2,d3,TRIN,TCIN,CCi,h1,kW,mR,CPR,mC,CPC,hINF,TINF)

% Variables defination
        % Variables defination
    % y(1) – T_W
    % y(2) – T_Wdot
        % y(3) – T_R
        % y(4) – T_C
        % y(5) – T_R * C_CO
        % y(6) – T_R * C_O2

PCO = y(5)*Rgasconst; % [dynes/cm2]
PO2 = y(6)*Rgasconst; % [dynes/cm2]
PCO = PCO/10/1e3; % [kPa]
```

```
PO2 = PO2/10/1e3; % [kPa]
dCCOTRdx = -C1*C2*exp(-Ea/Rgasconst/y(3))*PCO^a*PO2^b; % Is negative

dydx = [y(2)
        -(d1*(y(3)-y(1))-d2*(y(1)-y(4)))*4*h1/kW/(d2*d2-d1*d1)
        (y(1)-y(3))*pi*h1*d1/mR/CPR + dCCOTRdx*HOR/mR/CPR*V0/T0
        (-y(1)+y(4)+hINF*d3/h1/d2*(y(4)-TINF))*pi*h1*d2/mC/CPC
        dCCOTRdx
        1/2/s*dCCOTRdx] ;
```

```
function res = eqn_bc(ya,yb,C1,C2,Ea,Rgasconst,a,b,s,HOR,V0,T0, ...
    d1,d2,d3,TRIN,TCIN,CCi,h1,kW,mR,CPR,mC,CPC,hINF,TINF)
% Variables defination
        % Variables defination
    % y(1) - T_W
    % y(2) - T_Wdot
        % y(3) - T_R
        % y(4) - T_C
        % y(5) - T_R * C_CO
        % y(6) - T_R * C_O2
res = [ya(1)-(d1*ya(3)+d2*ya(4))/(d1+d2)
       yb(1)-(d1*yb(3)+d2*yb(4))/(d1+d2)
       ya(3)-TRIN
       yb(4)-TCIN
       ya(5)-TRIN*CCi(1)
       ya(6)-TRIN*CCi(2)];
```

```
function v = eqn_init(d1,d2,d3,kW,mR,CPR,mC,CPC, ...
    hINF,TINF,h1,TRIN,TCIN,qdot)
v = [(d1*TRIN+d2*TCIN)/(d1+d2)
     0
```

```
     TRIN
     TCIN];
```

```
%% Sensitivity Post Processor for the Basic CFHE model
% Amit Dhingra
% 01–31–2005
%
% Run this files only after running the mail program.
% It uses the data in the memory.
% Change to write data to a file in main program and read it here

%% Init
% close all;
figure
hold('all')

%% Plot main plot
plh1 = subplot(2,2,1);
hold on;
for k = 1:12:no_steps
    plot(solk(k).x',solk(k).y(3:4,:)')
end;
grid on
xlabel('Length[cm]');
ylabel('Temperature[K]');
title('Counterflow HE with axial wall conduction')
legend('Tr','Tc');

%% Plot Qtran and Qrecup
plh2 = subplot(2,2,2);
plot(var_space,Qtran,var_space,Qgain);
%axes(ah2(1));
```

```
hold all;
xlabel(var_desc);
ylabel('Heat rate [W]');
title('Qtran and Qrecup');
legend('Qtran','QRecup');
grid on

%% Plot Isothermality and efficiency
plh3 = subplot(2,2,3);
[ah3,p1,p2] = plotyy(var_space,Isotherm,var_space,effic)
xlabel(var_desc);
ylabel('Isothermality');
title('Isothermality and efficiency')
%legend([p1 p2],'Isotherm','effic');
axes(ah3(2));
ylabel('Efficiency')
grid on

%% Plot others sensitivity of Isothermality and effciency
plh4 = subplot(2,2,4);
[ah4,p1,p2] = plotyy(xvar,Isotherm_sens,xvar,effic_sens);
%axes(ah4(1));
xlabel(var_desc);
ylabel('Isothermality');
title('Sensitivity of Isothermality and Efficiency')
%legend([p1 p2],'Isotherm','effic');
axes(ah4(2));
ylabel('Efficiency')
hold on;
grid on;
```

Appendix D

UDF Code listing for local heat transfer coefficient

In Fluent, one is able to plug in a constant value for the heat transfer coefficient or a user defined function(UDF) can be used. By use of published literature[66], the local heat transfer coefficient is calculated for every mesh point on the top and bottom surface of the silicon micro-reactor assembly in Chapter 5. This gives accurate values for the convection heat transfer from the silicon micro-reactor. The C code used to implement equations 5.1 and 5.2 in a UDF is shown below.

```
#include "udf.h"
#define PI 3.141592654

DEFINE_PROFILE(top_heattrancf, thread, position)
{
  real r[ND_ND];        /* this will hold the position vector */
  real x;
  face_t f;
  real our_temp;

  begin_f_loop(f, thread)
    {
```

```
      our_temp = F_T(f,thread);
    F_PROFILE(f, thread, position) = 4.2218* pow((our_temp-296),0.2273);
    }
  end_f_loop(f, thread)
}

DEFINE_PROFILE(bot_heattrancf, thread, position)
{
  real r[ND_ND];        /* this will hold the position vector */
  real x;
  face_t f;
  real our_temp;

  begin_f_loop(f, thread)
    {
      our_temp = F_T(f,thread);
    F_PROFILE(f, thread, position) = 2.1109* pow((our_temp-296),0.2273);
    }
  end_f_loop(f, thread)
}
```

Bibliography

[1] *Annual Energy Review, 2009*. United States Department of Energy. 1

[2] *Key World Energy Statistics 2011*. OECD Publishing. 1, 2

[3] Aleklett, K., Höök, M., Jakobsson, K., Lardelli, M., Snowden, S. and Söderbergh, B. (2010). The Peak of the Oil Age: Analyzing the world oil production Reference Scenario in World Energy Outlook 2008. *Energy Policy*, 38(3), pp. 1398–1414. 1

[4] Radovic, L. R. (1997). *Energy and Fuels in Society: Analysis of Bills and Media Reports*. McGraw-Hill. 2

[5] Taylor, A. M. (2008). Science review of internal combustion engines. *Energy Policy*, 36(12), pp. 4657–4667. 2

[6] Huo, H., Wu, Y. and Wang, M. (2009). Total versus urban: Well-to-wheels assessment of criteria pollutant emissions from various vehicle/fuel systems. *Atmospheric Environment*, 43(10), pp. 1796–1804. 2

[7] Ogden, J. M. (1999). Prospects for building a hydrogen energy infrastructure. *Annual Review of Energy and Environment.*, 24, pp. 227–279. 2, 3

[8] Acres, G., Frost, J., Hards, G., Potter, R., Ralph, T., Thompsett, D., Burstein, G. and Hutchings, G. (1997). Electrocatalysts for fuel cells. *Catalysis Today*, 38(4), pp. 393–400. 2

[9] Lemons, R. A. (1990). Fuel cells for transportation. *Journal of Power Sources*, 29, pp. 251–264. 2

[10] Qi, A., Peppley, B. and Karan, K. (2007). Integrated fuel processors for fuel cell application: A review. *Fuel Processing Technology*, 88(1), pp. 3–22. 3

[11] David, E. (2005). An overview of advanced materials for hydrogen storage. *Journal of Materials Processing Technology*, 162-163, pp. 169–177. 3

[12] Duret, B. and Saudin, A. (1994). Microspheres for on-board hydrogen storage. *International Journal of Hydrogen Energy*, 19, pp. 757–764. 3

[13] Amphlett, J., Creber, K., Davis, J., Mann, R., Peppley, B. and Stokes, D. (1994). Hydrogen production by steam reforming of methanol for polymer electrolyte fuel cells. *Intl. J. Hydrogen Energy*, 19, pp. 131–137. 3

[14] Farrell, C., Gardner, C. and Ternan, M. (2007). Experimental and modelling studies of CO poisoning in PEM fuel cells. *Journal of Power Sources*, 171(2), pp. 282–293. 4

[15] Chu, H., Wang, C., Liao, W. and Yan, W. (2006). Transient behavior of CO poisoning of the anode catalyst layer of a PEM fuel cell. *Journal of Power Sources*, 159(2), pp. 1071–1077. 4

[16] O'Connell, M., Kolb, G., Schelhaas, K.-P., Schuerer, J., Tiemann, D., Ziogas, A. and Hessel, V. (2010). The development and evaluation of microstructured reactors for the water gas shift and preferential oxidation reactions in the 5 kW range. *International Journal of Hydrogen Energy*, 35(6), pp. 2317–2327. 4

[17] Jensen, K. F. (2001). Microreaction engineering – is small better? *Chemical Engineering Science*, 56, pp. 293–303. 4, 5, 14, 44, 45, 61

[18] Kolb, G. and Hessel, V. (2004). Micro-structured reactors for gas phase reactions. *Chemical Engineering Journal*, 98, pp. 1 – 38. 4

[19] Hessel, V., Hardt, S., Löwe, H. and Schönfeld, F. (2003). Laminar mixing in interdigital micromixers with different mixing chambers. Part 1: Experimental characterization. *AIChE J.*, pp. 566–577. 4, 46

[20] Janicke, M. T., Kestenbaum, H., Hagendorf, U., Schüth, F., Fichtner, M. and Schubert, K. (2000). The controlled oxidation of hydrogen from an explosive mixture of Gases using a microstructured reactor/heat exchanger and Pt/Al_2O_3 catalyst. *J. of Catalysis*, pp. 282–293. 4, 46

[21] Srinivasan, R., Hsing, I., Berger, P., Jensen, K., Firebaugh, S., Schmidt, M., Harold, M., Lerou, J. and Ryley, J. (1997). Micromachined reactors for catalytic partial oxidation reactions. *AIChE J.*, 43(11), pp. 3059–3069. 4, 46

[22] Ajmera, S., Delattre, C., Schmidt, M. and Jensen, K. (2002). Microfabricated Differential Reactor for Heterogeneous Gas Phase Catalyst Testing. *J. Catalyses*, 209, pp. 401–412. 4, 46

[23] Handique, K., Burke, D., Mastrangelo, C. and Burns, M. (2000). Nanoliter liquid metering in microchannels using hydrophobic patterns. *Analytical Chemistry*, 72, pp. 4100–4109. 4, 46

[24] Holladay, J., Jones, E., Phelps, M. and Hu, J. (2002). Microfuel processor for use in a miniature power supply. *Journal of Power Sources*, 108, pp. 21–27. 4, 46

[25] Besser, R. S., Ouyang, X. and Surangalikar, H. (2003). Hydrocarbon hydrogenation and dehydrogenation reactions in microfabricated catalytic reactors. *Chemical Engineering Science*, 58, pp. 19–26. 5, 44, 61

[26] Korotkikh, O. and Farrauto, R. (2000). Selective catalytic oxidation of CO in H_2: fuel cell applications. *Catalysis Today*, 62(2-3), pp. 249–254. 6

[27] Manasilp, A. and Gulari, E. (2002). Selective CO oxidation over Pt/alumina catalysts for fuel cell applications. *Applied Catalysis B: Environmental*, 37(1), pp. 17–25. 48

[28] Avgouropoulos, G., Ioannides, T., Papadopoulou, C., Batista, J., Hocevar, S. and Matralis, H. (2002). A comparative study of Pt/γ-Al_2O_3, Au/α-Fe_2O_3 and CuO-CeO_2 catalysts for the selective oxidation of carbon monoxide in excess hydrogen. *Catalysis Today*, 75(1-4), pp. 157–167. 6

[29] Barnes, R. (1988). *Hydrogen storage materials*. Trans Tech Publications, Limited, New York. 9

[30] Dillon, A. C., Jones, K. M., Bekkedahl, T. A., Kiang, C. H., Bethune, D. S. and Heben, M. J. (1997). Storage of hydrogen in single-walled carbon nanotubes. *Nature*, 386, pp. 377–379. 9

[31] Srinivas, S., Dhingra, A., Im, H. G. and Gulari, E. (2004). A scalable silicon microreactor for preferential CO oxidation: Performance comparison with a tubular packed-bed microreactor. *Applied Catalysis A: General*, 274 Issues 1–2, pp. 285–293. 9, 14, 46, 48

[32] Micyus, N. J., McCurry, J. D. and Seeley, J. V. (2005). Analysis of aromatic compounds in gasoline with flow-switching comprehensive two-dimensional gas chromatography. *Journal of Chromatography A*, 1086, pp. 115–121. 11

[33] Hernandez-Maldonado, A. J., Qi, G. and Yang, R. T. (2005). Desulfurization of commercial fuels by [pi]-complexation: Monolayer CuCl/[gamma]-Al2O3. *Applied Catalysis B: Environmental*, 61, pp. 212–218. 11

[34] Hernandez-Maldonado, A. J., Yang, F. H., Qi, G. and Yang, R. T. (2005). Desulfurization of transportation fuels by [pi]-complexation sorbents: Cu(I)-, Ni(II)-, and Zn(II)-zeolites. *Applied Catalysis B: Environmental*, 56, pp. 111–126. 11

[35] Tadd, A. R., Gould, B. D. and Schwank, J. W. (2005). Packed bed versus microreactor performance in autothermal reforming of isooctane. *Catalysis Today*, 110, pp. 68–75. 12, 60, 87

[36] Haswell, S. J. and Skelton, V. (2000). Chemical and biochemical microreactors. *TrAC Trends in Analytical Chemistry*, 19, pp. 389–395. 14, 61

[37] Kolb, G., Schrer, J., Tiemann, D., Wichert, M., Zapf, R., Hessel, V. and Lwe, H. (2007). Fuel processing in integrated micro-structured heat-exchanger reactors. *Journal of Power Sources*, 171(1), pp. 198–204. 14

[38] Besser, R. (2011). Thermal integration of a cylindrically symmetric methanol fuel processor for portable fuel cell power. *International Journal of Hydrogen Energy*, 36(1), pp. 276 – 283. 15

[39] Northrop, W. F., Choi, S. O. and Thompson, L. T. (2012). Thermally integrated fuel processor design for fuel cell applications. *International Journal of Hydrogen Energy*, 37(4), pp. 3447 – 3458. 15

[40] Kolb, G., Baier, T., Schrer, J., Tiemann, D., Ziogas, A., Specchia, S., Galletti, C., Germani, G. and Schuurman, Y. (2008). A micro-structured 50 kW complete fuel processor for iso-octane as hydrogen supply system for mobile auxiliary power units: Part II Development of water gas shift and preferential oxidation catalysts reactors and assembly of the fuel processor. *Chemical Engineering Journal*, 138, pp. 474–489. 16

[41] Ahmed, S., Ahluwalia, R., Lee, S. and Lottes, S. (2006). A gasoline fuel processor designed to study quick-start performance. *Journal of Power Sources*, 154(1), pp. 214 – 222.

[42] Löffler, D. G., Taylor, K. and Mason, D. (2003). A light hydrocarbon fuel processor producing high-purity hydrogen. *Journal of Power Sources*, 117, pp. 84 – 91. 16

[43] Kim, G.-Y., Mayor, J. R. and Ni, J. (2005). Parametric study of microreactor design for water gas shift reactor using an integrated reaction and heat exchange model. *Chemical Engineering Journal*, 110, pp. 1–10. 19

[44] Kockmann, N. (2008). *Transport Phenomena in Micro Process Engineering*. Heat and Mass Transfer. Springer. 21

[45] Ronney, P. D. (2003). Analysis of non-adiabatic heat-recirculating combustors. *Combustion and Flame*, 135, pp. 421–439. 22, 23

[46] Dhingra, A., Srinivas, S., Im, H. G. and Gulari, E. (2005). A scalable silicon microreactor for preferential CO oxidation with and integrated platinum heater. *ASME International Mechanical Congress and Exposition 2005-81497*. 24, 26

[47] Kim, D. H. and Lim, M. S. (2002). Kinetics of selective CO oxidation in hydrogen-rich mixtures on Pt/alumina catalysts. *Applied Catalysis A: General*, 224, pp. 27–38. 25, 60, 69, 70

[48] Kuo, K. K. (2005). *Principles of combustion*. John Wiley, Hoboken, New Jersey. 26, 109

[49] MathWorks, I. (1999). *MATLAB : The language of technical computing : User’s guide*. MathWorks, Inc. 26, 71

[50] van Dijk, H., Boon, J., Nyqvist, R. and van den Brink, R. (2010). Development of a single stage heat integrated water gas shift reactor for fuel processing. *Chemical Engineering Journal*, 159, pp. 182 – 189. 29

[51] Geankoplis, C. (1993). *Transport Processes and Unit Operations*. Prentice Hall. 44

[52] Bird, R. B., Stewart, W. E. and Lightfoot, E. N. (2001). *Transport Phenomena*. Wiley. 44

[53] Chau, J., Wan, Y., Gavriilidis, A. and Yeung, K. (2002). Incorporating zeolites in microchemical systems. *Chem. Engg. J.*, 1-3, pp. 187–200. 46

[54] Franz, A., Jensen, A. and Schmidt, M. (2000). Palladium membrane microreactors. *Proc. 3rd Intl. Conf. on Microreaction Technology*, pp. 267–276. 46

[55] Dhingra, A. and Im, H. G. (2005). Counterflow Heat Exchanger Model For Thermal Management Of A Compact Catalytic Fuel Processor System. *ASME International Mechanical Congress and Exposition 2005-81481*. 47

[56] Deen, W. M. (1998). *Analysis of Transport Phenomena*. Oxford University Press, USA. 47

[57] Perry, R. H., Maloney, J. O., Green, D. W. and Knovel (1997). Perry's chemical engineers' handbook. 48, 101

[58] Lide, D. (1995). *CRC Handbook of Chemistry and Physics, 76th Edition*. CRC Handbook of Chemistry and Physics, 76th Edition. CRC Press. 48

[59] Agrafiotis, C. and Tsetsekou, A. (2002). Deposition of meso-porous γ-alumina coatings on ceramic honeycombs by sol-gel methods. *Journal of the European Ceramic Society*, 22(4), pp. 423–434. 48

[60] Agrafiotis, C., Tsetsekou, A., Stournaras, C., Julbe, A., Dalmazio, L. and Guizard, C. (2002). Evaluation of sol-gel methods for the synthesis of doped-ceria environmental catalysis systems. *Journal of the European Ceramic Society*, 22(1), pp. 15–25. 48

[61] Valentini, M., Groppi, G., Cristiani, C., Levi, M., Tronconi, E. and Forzatti, P. (2001). The deposition of γ-Al_2O_3 layers on ceramic and metallic supports for the preparation of structured catalysts. *Catalysis Today*, 69(1-4), pp. 307–314. 48

[62] Fluent (2002). *Fluent 6.0*. Fluent Inc., Lebanon, N.H. 50, 56, 62, 65

[63] Cutlip, M. B. and Shacham, M. (1999). *Problem solving in chemical engineering with numerical methods*. Prentice Hall PTR, Upper Saddle River, NJ. 62

[64] Christou, A. (1994). *Electromigration and electronic device degradation*. Wiley, New York, NY, USA. 63

[65] Ohring, M. (1998). *Reliability and failure of electronic materials and devices*. Academic Press, San Diego. 63

[66] Incropera, F. P. and DeWitt, D. P. (1996). *Fundamentals of heat and mass transfer*. Wiley, New York. 65, 122

[67] Fogler, H. S. (1999). *Elements of chemical reaction engineering*. Prentice Hall PTR, Upper Saddle River, N.J. 69

[68] Kim, C., Tadd, A., Kim, G.-Y., Dhingra, A., Im, H., Ni, J., Schwank, J. and Thompson, L. (2006). Thermally integrated micro-channel fuel processor. *AIChE Annual Meeting, Conference Proceedings*. 94

[69] Department of Energy: Hydrogen Production . http://www1.eere.energy.gov/hydrogenandfuelcells. 100